Distribution Agreement

In presenting this dissertation as a partial fulfillment of the requirements for an advanced degree from Emory University, I agree that the Library of the University shall make it available for inspection and circulation in accordance with its regulations governing materials of this type. I agree that permission to copy from, or to publish, this dissertation may be granted by the professor under whose direction it was written, or in his absence, by the Dean of the Graduate School when such copying or publication is solely for scholarly purposes and does not involve financial gain. It is understood, that any copying from, or publication of, this dissertation which involves potential financial gain will not be allowed without written permission.

Signature

_____   _____
Neslihan Ucuncuoglu   Date

Influence of Protein and Solvent Dynamics on Reactions in Ethanolamine Ammonia-Lyase addressed by using Time-Resolved Electron Paramagnetic Resonance and UV-visible Spectroscopy

By

Neslihan Ucuncuoglu
Doctor of Philosophy
Physics

Advisor: Dr. Kurt Warncke

Approved for the Department by:

_____
Advisor

_____
Dr. Fereydoon Family
Committee Member

_____
Dr. Laura Finzi
Committee Member

_____
Dr. Connie Roth
Committee Member

_____
Dr. Emily Weinert
Committee Member

Accepted:

_____
Lisa A. Tedesco, Ph.D. Dean of the Graduate School

_____
Date

Influence of Protein and Solvent Dynamics on Reactions in Ethanolamine Ammonia-Lyase addressed by using Time-Resolved Electron Paramagnetic Resonance and UV-visible Spectroscopy

by

Neslihan Ucuncuoglu
B.S., Bogazici University, Turkey 2007

Advisor
Kurt Warncke, Ph.D.

An abstract of
A Dissertation Submitted to the Faculty of the
James T. Laney School of Graduate Studies of Emory University
in partial fulfillment of the requirements for the degree of
Doctor of Philosophy
in Physics
2016

Abstract

Influence of Protein and Solvent Dynamics on Reactions in Ethanolamine Ammonia-Lyase addressed by using Time-Resolved Electron Paramagnetic Resonance and UV-visible Spectroscopy

By

Neslihan Ucuncuoglu

The radical-rearrangement step in the reaction of the (*S*)-2-aminopropanol-generated Co(II)-substrate radical pair in coenzyme B12 (adenosylcobalamin)-dependent ethanolamine ammonia-lyase (EAL) from *Salmonella typhimurium* has been studied by using time-resolved, full-spectrum, continuous-wave electron paramagnetic resonance (EPR) spectroscopy over the temperature range of 210 – 250 K. This approach addresses the kinetics of the radical rearrangement reaction step in EAL with a single step resolution. We identified that the substrate assumes two sequential inter-converting configurations, one of which is proposed to be reconfigured by the protein to form the native Co(II)-substrate radical pair, and the other, relatively high entropy/enthalpy state, which reacts by a non-native pathway to form an magnetically-uncoupled Co(II) and radical species. The emergence of the unprecedented, non-native pathway of deleterious radical reaction enabled us to assess whether the protein dynamic effect is generic, or specific to the native reaction. The free energy curve profiled a different *T*-dependency for the native and non-native reaction pathways at $T > 240$ K which could indicate the presence of protein configurational fluctuations that guide the native reaction pathway. In the second part of the dissertation, we presented the temperature dependence of the spin probe (TEMPOL) mobility in aqueous solution of EAL and (*S*)-2-aminopropanol to investigate the solvent-dynamical contributions to the enzyme kinetics. In the final chapter of the this study, a new reaction step; the conversion of adenosylcob(III)alamin to cob(II)alamin through the Co-C bond homolysis is investigated by using optical absorption spectroscopy, using ethylene glycol as the substrate. The EAL single step kinetics under these conditions were unraveling at temperature and solvent conditions that are close to the physiological conditions. The decay of the adenosylcob(III)alamin absorption signal is used as a measure to quantify the conversion, and it is proposed that the cob(II)alamin formation reaction is at least partially rate-determined by the hydrogen transfer-1 step. Overall, the results provide insight into the mechanisms and protein and solvent dynamical contributions to the substrate radical formation and rearrangement reactions in EAL.

Influence of Protein and Solvent Dynamics on Reactions in Ethanolamine Ammonia-Lyase addressed by using Time-Resolved Electron Paramagnetic Resonance and UV-visible Spectroscopy

by

Neslihan Ucuncuoglu
B.S., Bogazici University, Turkey 2007

Advisor
Kurt Warncke, Ph.D.

A Dissertation Submitted to the Faculty of the
James T. Laney School of Graduate Studies of Emory University
in partial fulfillment of the requirements for the degree of
Doctor of Philosophy
in Physics
2016

I dedicate this work to my parents,
my husband and my son.
I could not have done this without you.

Acknowledgements

First and foremost, I would like to express my sincere gratitude to my advisor Prof. Dr. Kurt Warncke for being a tremendous mentor for me. Your immense knowledge, enduring encouragement, and joy while doing experiments have been an invaluable source of support and inspiration for me. Without your guidance and constant feedback, this Ph.D would not have been achievable.

I would also like to thank my committee members, Prof. Dr. Fereydoon Family, Prof. Dr. Laura Finzi, Prof. Dr. Connie Roth and Prof. Dr. Emily Weinert for serving as my committee members and their insightful comments and guidance.

I want to thank present and past members of the Warncke lab: Dr. William Gunderson Dr. Wesley Robertson, for giving me an introduction into our lab, and Dr. Hanlin Chen, Dr. Adonis Bovell, Meghan Kohne and Benjamen Nforneh for their intellectual contributions during our group meetings.

I am also grateful for the friendship of my fellow graduate students and staff in the Physics Department for making my years at Emory memorable and fun. A special thanks to Emrah&Arzu Simsek (Avzu aplasi), your timely help and friendship shall always be remembered.

A huge, warm thanks to Dr. Emine Yaylali (Ems) for always looking out for me and being a remarkable friend. Thank you, my lifelong friends, Ems, Dr. Aysun Hiziroglu (Aysi) and Fatma Yigit, I consider myself extremely fortunate to have friends like you.

I am deeply grateful to my mother, Meryem Parlar, my father, Selim Parlar, for your unselfish love, unconditional support and for all the sacrifices that you have made on my behalf. I would not be here if not for you. I am also forever grateful for the constant support and love coming from my in-laws, Ruveyda and Cevat Ucuncuoglu. My sisters and my best friends all my life, Leyla Ates, and Rabia Betul Parlar, thank you for your love, care and humor that provided me unlimited moral support. Words cannot express the feelings I have for my entire family, your love and prayers for me were what sustained me thus far. Canim ailem, hepinizi cok seviyorum.

I would like to acknowledge my loving, supportive, encouraging, patient husband, Dr. Suleyman Ucuncuoglu (yol arkadasim, siginagim) who faithfully encouraged me during the challenges of graduate school and life. Last, but definitely not least, I would like to thank to my lovely, sweet son, Mehmet Duha Ucuncuoglu (gun isigim, yumurcagim, annesinin arkadasi) for giving me the reason to continue. You are the pride and joy of my life. Thank you for everything that you are, and everything you will become. I love you so much.

Table of Contents

List of Figures

Chapter 1

List of Tables

Chapter 1

Chapter 1

Introduction

1.1 Literature Review

1.1.1 Vitamin B$_{12}$: Structure and derivatives

Vitamin B$_{12}$ (cyanocobalamin) is a biomolecule that is widely abundant in nature and vital for human health. This naturally occurring organometallic compound has been intriguing for researchers for almost 70 years owing to its peculiar structure and unusual reactivity since its first isolation in 1948 [1-3]. Much emphasis had been placed on the structure and the synthesis studies for the first 10 years [4-6], until the discovery of the coenzyme form, adenosylcobalamin (AdoCbl), and the other members of the coenzyme B$_{12}$ family at 1958 [7] which led to the rise of the still-continuing interest in the role of the coenzyme in enzymatic reaction mechanisms. The research on B$_{12}$ has become phenomenal and yielded 3 Nobel prizes in chemistry (1964, 1965, 1981) and one in physiology and medicine so far (1934).

Structurally, vitamin B$_{12}$ is a cobalt corrinoid, which is very similar to the porphyrins (heme) having the four pyrrole rings joined with methine bridges, with some small yet chemically important differences (Figure 1-1). One difference is that the $C - CH_3$ methylene link between the A and D rings is not present in vitamin B$_{12}$, thus vitamin B$_{12}$ has one C atom less than the porphyrins (Figure 1-1). In addition, the corrin ring is not fully conjugated like the porphyrins, which makes it flexible comparably, and more open to conformational changes [8]. Also, the corrin ring does not look as flat from the side, and has the pendant axial base (lower ligand) linked back with a nucleotide loop onto the corrin ring itself (Figure 1-1). These differences add up to make the corrinoids unique complexes that exhibit large amount of distortion and flexibility. Also, the possibility of a steric repulsion between the lower ligand and equatorial ligand increases the flexibility of the molecule [9].

In the center cavity of the cobalt corrin, there is the cobalt atom in the $+3$ oxidation state in octahedral coordination with the nitrogens of the pyrrole rings and axial ligands (Figure 1-1). The cobalt corrinoid containing the nucleotide group is referred to cobinamide (Cbi), and when the Cbi has the DMB (α-5,6-$dimethybenzimidazole\ nucleotide$) as the lower ligand, it is called as cobalamin (Cbl) (Figure 1-1). The type of the upper ligand (X in Figure 1-1) defines the derivatives of B$_{12}$, some of which are: aquocobalamin (X $= H_2O$), vitamin B$_{12}$ (X$= CN$), methylcobalamin (X$= CH_3$) or adenosylcobalamin (X $= 5'$-$deoxyadenosine$) [10]. Among these derivatives, only methylcobalamin (MeCbl) and AdoCbl are enzymatically competent [11].
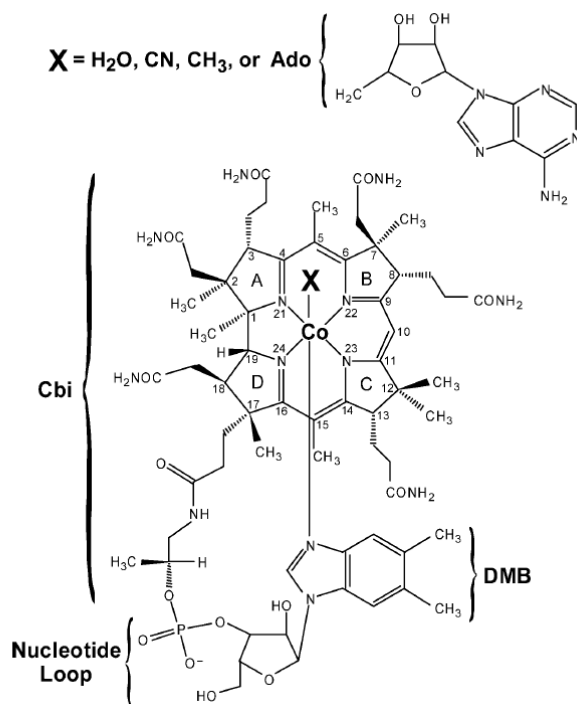
Figure 1-1 Chemical structure and numbering of the Co (III)-cobalamin (Cbl) form of the vitamin B$_{12}$ [11]. The X is representing the functional upper ligand.

The B$_{12}$ derivatives catalyze very important and unusual reactions effectively, either as an electro-chemical or a covalent catalyst [10]. The key feature of the B$_{12}$-dependent reactions is the cleavage of the bond between the Co and $5'$-C in the coenzyme, and hence forming the three oxidation states. The difference between the reactions of the two active B$_{12}$ derivatives depends on how this Co-C bond cleavage occurs: (i) Heterolytic cleavage which forms either $Co(I)$ or $Co(III)$ with a positively or negatively charged C respectively, and (ii) Homolytic cleavage of the Co-C bond which generates a radical and a $Co(II)$. The heterolytic cleavage of the Co-C bond occur in the methyl-transfer reactions that is catalyzed by MeCbl-dependent enzymes [11]. The homolytic cleavage, on the other hand, is associated with the AdoCbl-dependent enzyme family, which is of specific interest for this dissertation study.

1.1.2   Ethanolamine Ammonia-Lyase: an AdoCbl-dependent enzyme

AdoCbl-dependent enzyme superfamily

The AdoCbl-dependent enzyme superfamily utilizes the Ado group that is occupying the upper axial position of the cobalt corrin ring of AdoCbl for generation of reactive radicals for atom migration or elimination reactions [10, 12-14] (Figure 1-1). The members of the enzyme superfamily are mostly found in eubacteria, with only one exception that is found in mammals (methylmalonyl-CoA mutase) [15]. The AdoCbl-dependent enzymes can be categorized into three classes based on the nature of the functional group that is migrated and the substituent group that takes place of the migrated group [10]. Class I are mutases that catalyze the carbon skeleton rearrangements so that the C-C bond is cleaved, and includes glutamate mutase [16], 2-methylene-glutarate mutase [10, 17], isobutyryl-CoA mutase [18] and methylmalonyl-CoA mutase [13, 19].

Class III are aminomutases that catalyzes the migration of the amino group to the adjacent C atom by using pyridoxal cofactor (PLP) to form a Schiff base, hence catalyzes the cleavage of the C-N bond. This group includes 2,3-aminomutase [20] and ornithine 4,5-aminomutase [21]. Class II AdoCbl-dependent enzymes catalyzes are the eliminases that catalyze the migration and elimination of the amino or the hydroxyl group [10] which include glycerol dehydratase [22, 23], propane-1,2-diol dehydratase [24, 25], and ribonucleotide triphosphate reductase [26] and ethanolamine ammonia lyase (EAL, EC 4.3.1.7) [27]. Among these AdoCbl-dependent enzymes, the mechanism of the EAL is the focus of this dissertation.

Understanding the catalytic cycle of AdoCbl-dependent enzymes

The common mechanistic characteristics that applies to all the AdoCbl-dependent enzymatic reactions (except ribonucleotide reduction) is the migration of the X group from one carbon atom to the adjacent carbon atom, in exchange for a hydrogen atom that migrates in the opposite direction (Figure 1-2). The homolysis of the Co-C bond, generates a low-spin, $S = 1/2$ Co(II) and unmasks the $5'$-deoxyadenosyl radical (Ado•) [14]. This is a highly reactive radical that could react spontaneously in solution, however, in the holoenzyme, it solely reacts with the substrate to abstract the hydrogen atom, and activate it for the 1, 2-rearrangement (Figure 1-2) [28-31]. The rearranged substrate transfers hydrogen atom back to Ado• exclusively, not to the bulk solvent or the surrounding molecules, to reform Ado-H complex [32]. The mechanism by which the Ado• and the substrate radicals are utilized for this specific reaction cycle has been studied extensively, and has not been fully resolved yet.
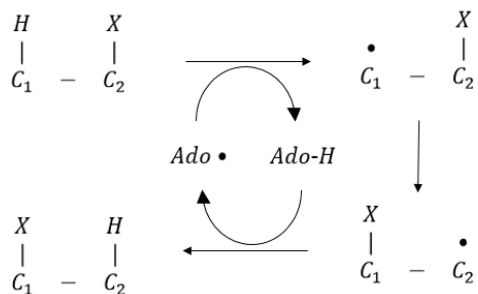
Figure 1-2 Basic mechanism for AdoCbl-dependent rearrangement reactions. The X in the substrate can be-OH,-NH_2 or a C containing fragment.

The mechanism behind the homolysis of the Co-C bond by the holoenzyme is a common interest in the kinetics mechanistic investigation of AdoCbl-dependent enzymes [15]. The bond dissociation energy of Co-C bond of AdoCbl is estimated to be 30 $kcal/mol$ [33]. This energy is reduced to below 15 $kcal/mol$ by the AdoCbl-dependent enzymes which is equivalent to an about 10^{12}- fold acceleration in the homolysis rate [33-36]. Another aspect of the reaction that has not been elucidated yet is the role of the protein during the transfer of the H from substrate to the Ado•. The geometry of the Co(II) and the C centers of the coenzyme and the substrate is studied for the EAL and based on the active site geometry; it is suggested that Ado• actively mediates this transfer by undergoing a displacement of 5 - 7 Å [30, 37]. Another challenge to understand is the involvement of the coenzyme in the substrate radical rearrangement step. Computational studies, using the close proximity of the Ado• group to the substrate methyl group and the orbital overlap between the two as a starting point, speculates about participation of the coenzyme to the rearrangement reaction in both Class I [38, 39] and Class II enzymes [40].

Ethanolamine Ammonia Lyase (EAL)

EAL is a Class II AdoCbl dependent enzyme expressed in enteric bacteria that catalyzes the 1,2-amino shift of vicinal amino alcohols, such as 2-aminoethanol and (R)- and (S)-2-aminopropanols to oxo-compounds and ammonia. EAL from *Salmonella typhimurium* is composed of two subunits (Figure 1-3): a 453-residue, 49.4 kDa EutB (α) and a 286-residue, 32.1 kDa EutC (β) subunit which are coded by *eutb*, and *eutc* genes respectively [41]. The two subunits form a hexamer of $\sim 500\ kDa$ presented in a $\alpha_6\beta_6$ stoichiometry in the active enzyme. The substrate binding site is in the EutB subunit [42]. The crystal structures of the EutB and EutC subunits of the EAL from *E. coli* were solved in 2010 [43]. The progress in the obtaining the crystal structure information of EAL, makes it a feasible target for further detailed kinetics and mechanistic studies. Also, the $\alpha_8\beta_8$ barrel, or triose phosphate isomerase (TIM), barrel secondary structure in the EutB subunit makes EAL a very robust enzyme, preserving its activity at a very wide range of pH (6.6 to 8.2) (Figure 1-4). This feature is another factor that makes EAL suitable for our experiments to be held at cryogenic temperatures.
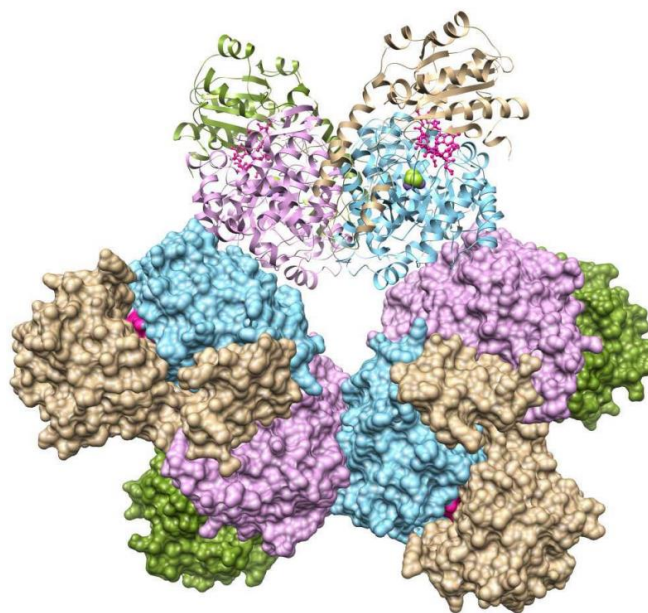
Figure 1-3 Overall $\alpha_6\beta_6$ structure of EAL is shown [44]. α and β subunits are shown in violet/sky blue and green/khaki, respectively. The subunits are shown in surface model except one (αβ)2 dimer that is shown in ribbon model. The CN-Cbl is attached to the interface of α and β subunits and is shown in ball and stick model. The substrate, 2-amino-1-propanol is attached to the active site and is shown as CPK model.
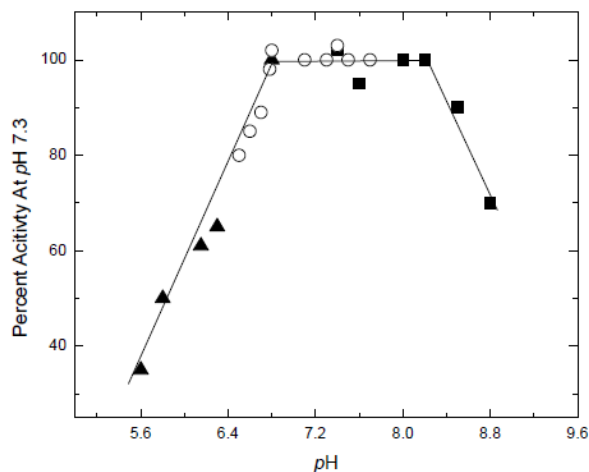
Figure 1-4 EAL activity vs. pH plot; open circle, solid square and solid triangles represent the different buffer conditions: Phosphate buffer, Tris buffer and Citrate buffer respectively [45].

EAL is one of the few enzymes that lack stereospecificity [28, 44] therefore it acts on enantiomers of the aminoethanol, such as (R)- and (S)-2- aminopropanol [28, 46]. Ethylene glycol and *2*-ethoxyethylamine are found to be the active substrates for the EAL [47-50] . The kinetic constants for EAL from *S. typhimurium* with different substrates are given in Table 1.1.

Table 1.1 Kinetic parameters for substrate analogues of EAL from *S. typhimurium*

Substrate	$K_m(\mu M)$	$k_{cat}\ (s^{-1})$	
Ethanolamine	13.6 ± 2.9	52.2 ± 3.7	[51]
(S)-2-aminopropanol	0.80 ± 0.06	0.12 ± 0.01	[52]
(R)-2-aminopropanol	9 ± 2	0.067 ± 0.001	[52]
Ethylene glycol	20×10^3	0.2	[49]

The minimal catalytic mechanism of EAL is shown in Figure 1-5 [13, 14]. The homolytic cleavage of the Co-C bond of the coenzyme AdoCbl that generates a low-spin, $S=1/2$ Co(II) and Ado• (**1** in Figure 1-5). The C5' radical center of the Ado• activates the substrate by abstracting the pro-S hydrogen atom from C1 (**2** in Figure 1-5) [28-30]. The substrate which has unpaired electron localized on C1, forms the Co(II)-substrate radical pair state. Then, the vicinal NH_2 group of the substrate radical migrates from the C2 to C1 which induces the transfer of the electron spin density on C2 (**3** in Figure 1-5). The product-like radical captures a hydrogen atom from the 5' carbon of 5'-deoxyadenosine, and forms bound product species (**4** in Figure 1-5) [31, 53]. The elimination of NH_3 from the product states, and leaving the acetaldehyde as the final product completes the full catalytic cycle (**5-6** in Figure 1-5) [31].
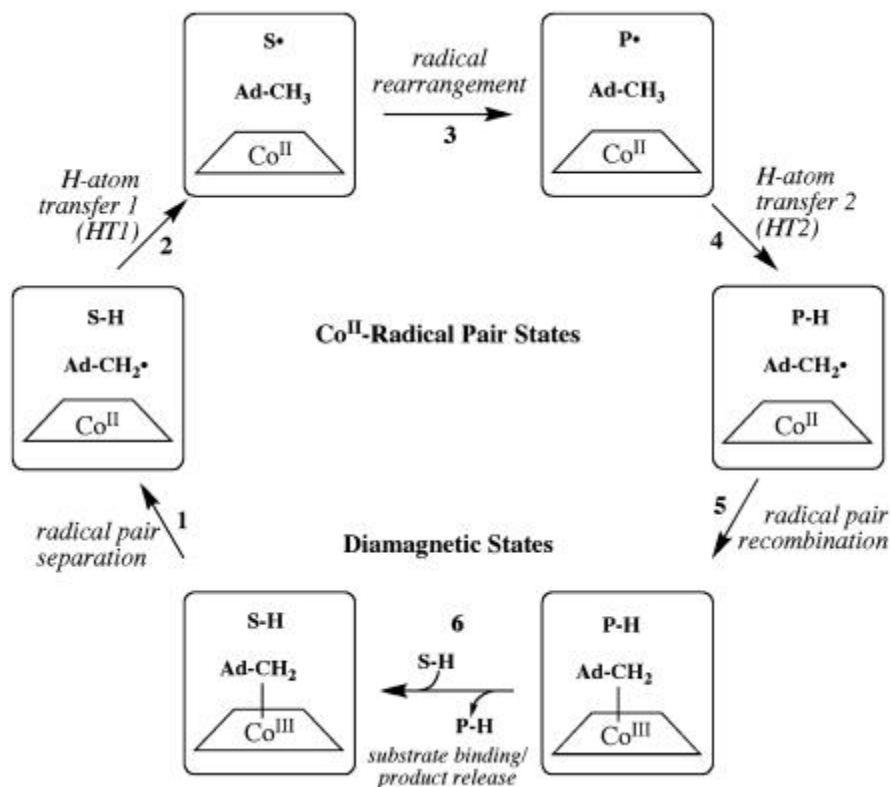
Figure 1-5 Minimal reaction mechanism for the EAL holoenzyme. The first step is the homolysis of the Co-C bond (**1**: *radical pair separation*), which generates the Ado• ($Ad\text{-}CH_2$) and Co(II). In the second step (**2**: *HT1*), Ado• abstracts an H-atom from the C1 of the substrate to form the Co(II)-substrate radical pair (Co(II) S•). In the third step (**3**: *radical rearrangement*) the amino group in the C2 of the substrate is migrated to the C1, and hence the radical spin moiety rearranges to on C2. The rearranged molecule is called as product radical (P•) which transfers a H-atom back from the Ado-H (**4**: *HT2*). The newly formed Ado• binds back to the Cbl (**5**: *radical pair recombination*), the products are released and substrate binds for the new cycle (**6**: *substrate binding/product release*).

1.2   EPR Theory

Electron paramagnetic resonance (EPR) spectroscopy is a powerful tool for detection and identification of the free radicals and their surroundings [54, 55]. The enzymatically catalyzed

processes that involve paramagnetic species either in the possession of the catalyst or as a reaction intermediate has been a suitable target for EPR studies [56, 57]. Such processes are relatively uncommon in biological molecules, and EAL is one of the handful of the proteins that utilizes an unpaired electron. In the following sections the basics of the EPR theory will be summarized.

1.2.1 Continuous wave (CW) EPR spectroscopy

EPR spectroscopy, with a broadest definition, is the interaction of the unpaired electrons with the magnetic component of the radiation in the microwave range frequency. The radiation energy is absorbed by the unpaired electrons which induces the transition of the electron's spin state to an excited energy level, or from an excited level to a lower level. The energy gap between the ground and the excited spin states is given by $\Delta E = h\nu$, where h is Planck's constant, and ν is the frequency of the applied radiation. This also applies to any absorption spectra.

Electron Zeeman Interaction

Angular momentum of an electron has two components; orbital angular momentum (**L**), and spin angular momentum (**S**). Orbital angular momentum of an electron is similar to the classical definition of the orbiting motion and can be expressed mathematically using spherical harmonics. However, spin angular momentum of an electron has no classical analogue, and cannot be directly measured or expressed in mathematical wave functions; only the components of it in a given coordinate frame can be measured. Therefore, it is considered as an intrinsic property of the electrons. As a characteristic of the quantum angular momentum phenomenon, both orbital momentum and the axial components of the spin angular momentum are quantized. For example,

the spin angular momentum in z-direction is given by $S_z = m_s \hbar$, where m_s is the spin magnetic quantum number $\pm \frac{1}{2}$ and $\hbar$ is the reduced Planck's constant.

Electron angular momentum constitutes a magnetic dipole moment, $\mu = \mu_\iota + \mu_s$, where μ_ι and μ_s are the orbital and spin components respectively. The magnetic dipole moment associated with the orbital angular momentum is equal to $\boldsymbol{\mu_\iota} = -\frac{g\beta}{2\hbar} \mathbf{I}$, and the magnetic dipole moment associated with spin angular momentum is equal to $\boldsymbol{\mu_s} = -\frac{g\beta}{\hbar} \mathbf{S}$, where β is the Bohr magneton, g is the g-factor for electron which is equal to 2.0023, and $\mathbf{I}$ and $\mathbf{S}$ are the nuclear and electron spin operators respectively. The constant β is found by $e\hbar/2m_e c$, where e, and m_e is the electron charge and mass, respectively. These relations show that the spin and the spin dipole moment is in opposite directions.
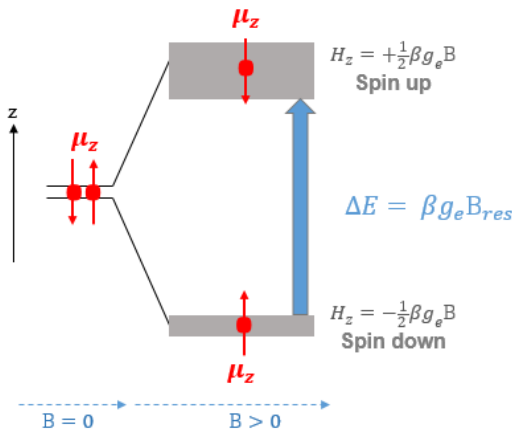
Figure 1-6 Figure illustrates the net transition of the spin states at the resonance condition for a free electron. Zeeman energy levels emerge when the field (B) is on, and the transition occurs at the resonance condition, which is stated in blue font. The energy terms for the two split spin states (Spin up, and Spin down: shown with the gray bars) are shown in gray font. The size of the gray bars visualize the relative populations of the two states that are distributed according to the Boltzmann distribution (see Equation 1-10). The red arrows represent the electron dipole moments measured along the z-direction.

When placed in an external magnetic field, the electron magnetic moment interacts with the magnetic field (**B**) and produces a torque ($\boldsymbol{\tau} = \boldsymbol{\mu} \times \mathbf{B}$) that tends to align itself in the direction of the applied field. The interaction of the electron with the applied external field is also known as *Zeeman Effect*. The absorbed energy in this process is given by the electron Zeeman operator H_{EZ} :

$$H_{EZ} = -\,(\boldsymbol{\mu}_\iota + \boldsymbol{\mu}_s) \cdot \mathbf{B}$$

Equation 1-1

When the magnetic dipole moment expressions are inserted in Equation 1-1, the electron Zeeman operator reads as:

$$H_{EZ} = g\beta\,(\mathbf{I} + 2\mathbf{S}) \cdot \mathbf{B}$$

Equation 1-2

If the orbital angular momentum is averaged for a free electron, spin angular momentum represents the total angular momentum in the Hamiltonian. For a free electron in z-direction, the Hamiltonian becomes:

$$H_{EZ,z} = \; g\beta B \hat{S}_{\mathbf{z}}$$

Equation 1-3

where $\hat{S}_{\mathbf{z}}$ represents the angular momentum when the orbital angular momentum is averaged. If the above $S_z = m_s \hbar$ expression is inserted in

Equation 1-3, the Hamiltonian gives two possible values; indicating the two possible orientations of the spin with respect to the applied field with the $H_{EZ,z} = -\frac{1}{2}g\beta B$ being the low-energy, spin-down orientation and the $H_{EZ,z} = +\frac{1}{2}g\beta B$ being the high-energy, spin-up orientation. When an oscillating field perpendicular to B that has an equal energy with the gap between the two spin states ($\beta_e g_e B$) is applied, the transition between the two states occurs. This phenomenon is referred as the resonance condition:

$$h\nu_{res} = g\beta B_{res}$$

<div align="right">Equation 1-4</div>

where ν_{res} and B_{res} are the frequency of the radiation and the magnitude of the applied field when the EPR occurs.

Higher order energy terms

Until now, the electron Zeeman term of the spin Hamiltonian is covered. The complete spin Hamiltonian has the higher order energy terms originating basically from x` (Equation 1-5).

The nuclear Zeeman interaction (H_{NZ}) describes the energy of the interaction between the nuclei having a net nuclear spin and the external magnetic field and is given by (for a constant field applied in z-direction): $H_{NZ,z} = g_n \beta_n B \hat{I}_z$, where g_n is the nuclear g-factor which is equal to approximately 5.59 for hydrogen, β_n is the nuclear magneton which is found by $e\hbar/2m_p$, and $\hat{I}_z$ is the spin angular momentum in z-direction for the nucleus. The energetic contribution of nuclear Zeeman term is small due to having the m_p, mass of the proton, in the denominator in β_n.

$$H = H_{EZ} + H_{NZ} + H_{HFI}$$

The term H_{HFI} refers to the interaction of the electron and nuclear dipole moments that gives rise a hyperfine structure in the spectra. The energy contribution of this interaction is given by $H_{HFI} = h(\mathbf{I} \cdot \hat{A} \cdot \mathbf{S})$, which is equal to $H_{HFI,z} = hA_{iso}\hat{I}_z\hat{S}_z$ in z-direction, where h is the Planck's constant and $\hat{A}$ is the second rank tensor for the hyperfine coupling constant, and A_{iso} is the isotropic hyperfine coupling constant. The magnetic nuclei is coupled to the unpaired electron spin through $\hat{A}$, which is defined with the two terms:

$$A_{iso} = \frac{8\pi}{3} g\beta g_n\beta_n|\Psi_0|^2$$

$$A_{dipolar} = g\beta g_n\beta_n \left[\frac{\mathbf{S}\cdot\mathbf{I}}{\mathbf{r}^3} - \frac{3(\mathbf{S}\cdot\mathbf{r})(\mathbf{I}\cdot\mathbf{r})}{\mathbf{r}^5}\right]$$

where first term, A_{iso} makes the Fermi contact component (H_{FC}) of the H_{HFI} that describes the unpaired electron-nuclei coupling, and is originating from spin density at the magnetic nucleus, $|\Psi_0|^2$. The isotropic coupling occurs for the magnetic nuclei and the *s*-orbital electrons through the chemical bonds. This give information about the covalent chemical bonds in a molecule and does not depend on the orientation of the molecule with respect to the external field. The dipolar coupling, on the other hand, is the interaction of the magnetic nuclei and the unpaired electrons through the space, and depends on the orientation. The dipolar coupling component of the H_{HFI} will be revisited in the next section, where the Zeeman Hamiltonian Anisotropies is discussed.

Zeeman Hamiltonian Anisotropies

So far, the Hamiltonian has been expressed for the simple, hydrogen-like atoms. For more complicated atoms, the orbital angular momentum term interacts with the field too, and cannot be averaged because of the lack of spherical symmetry. In this case, instead of using the orbital angular momentum term explicitly, its effect can be reflected in the Hamiltonian by introducing anisotropy to the g-factor that is expressing it with a matrix formalism. The magnetic field is a column vector of (1×3), and hence the g-factor becomes a (3×3) tensor $(\hat{g})$. In general, the principal axes of $\hat{g}$ are aligned with the molecular symmetry axes, therefore, the g-tensor becomes a diagonal matrix. The g-tensor reflects two orbital angular momentum related interactions. First one is the orbital angular momentum term in the Zeeman interaction. The second one is the spin-orbit interaction, which can be expressed as $H_{SO} = \lambda \mathbf{L} \cdot \mathbf{S}$, where λ is an experimentally found spin-orbit coupling constant.

The dipolar energy term in the hyperfine interaction also represents a dependence on the orientation of the unpaired electron with respect to the applied field, and hence introduces an orientation-dependent anisotropy to the system. The coupling of the magnetic dipole moment of the nucleus with the magnetic dipole moment of the electron is expressed with the $A_{dipolar}$ in

Equation 1-6 which is derived from the classical definition of the dipolar interaction energy $E = \frac{\mu_l \cdot \mu_s}{r^3} - \frac{3(\mu_l \cdot r)(\mu_s \cdot r)}{r^5}$. With spins aligned in the direction of the z-direction with the applied field, the dipolar interaction component of the hyperfine interaction Hamiltonian becomes; $H_{dipolar} = g\beta g_n \beta_n (\frac{1-3\cos^2\theta}{r^3})\hat{S}_z\hat{I}_z$ where θ is the angle between the electron dipole moment and the z-

direction. Together with the A_{iso}, the term $A_{dipolar}$ forms the hyperfine interaction tensor, $\hat{A}$ which is also found to be symmetric, i.e. has only the diagonal terms usually.

Additionally, when two unpaired electrons present, they produce a magnetic dipole-dipole energy interaction with each other that creates one singlet and one triplet splitting, also known as zero-field splitting. This interaction is expressed as $H_{EE} = \mathbf{S} \cdot \widehat{\mathbf{D}} \cdot \mathbf{S}$, where $\widehat{\mathbf{D}}$ is the zero field parameter and is represented with a second rank tensor. As with the $\hat{g}$, and $\hat{A}$, D-tensor can also be diagonalized.

For practical purposes, the g-factor can be expressed as:

$$\hat{g} = g\mathbb{1} + 2\lambda\widehat{\Lambda} \qquad \text{Equation 1-7}$$

where $\widehat{\Lambda}$ is the tensor that represents the spin-orbit coupling contributions to the energy. The zero field parameter is also expressed in terms of $\widehat{\Lambda}$ as below:

$$\widehat{\mathbf{D}} = \lambda^2\widehat{\Lambda} \qquad \text{Equation 1-8}$$

This formalism yields a new effective Hamiltonian for the anisotropic systems:

$$H_{eff} = \beta\mathbf{B} \cdot \hat{\mathbf{g}} \cdot \mathbf{S} + \mathbf{S} \cdot \widehat{\mathbf{D}} \cdot \mathbf{S} \qquad \text{Equation 1-9}$$

where the first expression is for the Zeeman and the spin-orbit coupling term, and the second expression is for the zero-field splitting term.

Statistical approach

The discussion until this point was about a single isolated spin. However, in real EPR samples there are many spins in many different orientations. In order to formulate such systems, statistical approach is more appropriate. As the magnetic moment vector that has an angle θ with the applied field aligns itself in the direction of the applied field (Figure 1-7), it experiences a precession with the frequency $\omega_L = \gamma B_z$, which is known as *Larmor frequency*. If an oscillating field (B_1) is applied, the spins continuously undergo the transition (flip) between the up and down orientations, with two orientations are occupied with the same probability. In this case, in order to detect a net transition, there must be a difference from the start between the populations of the two states, which is satisfied in the case of EPR, as stated in Boltzmann distribution:

$$\frac{N_{upper}}{N_{lower}} = exp\left(\frac{h\nu}{k_B T}\right)$$

Equation 1-10

where N_{upper} and N_{lower} are the number of spins in the upper (parallel alignment) and lower energy (antiparallel alignment) levels respectively, k_B is the Boltzmann constant, T is the temperature in Kelvin, and $h\nu$ is the energy separating the two levels. According to this equation, for an experiment at the X-band frequency (9.75 GHz), and at the temperature of 298 K, the ratio becomes 0.998 that makes the detection of the absorption possible.

When an oscillating field is applied, the rate of change of the population at upper (or similarly at lower) level can be expressed as:$\frac{dN_{upper}}{dt} = -Pn$ where n is the difference between the population of the upper and lower states and P is the general probability for a spin flip. From

here, we can calculate the rate of change of the two population as $\frac{dn}{dt} = -2Pn$, which yields to $n = n_0 \exp(-2Pt)$, where n_0 is the initial difference between the populations. This expression, by showing that the populations of the two states becomes equal in time (saturation condition), contradicts with the prediction that the Boltzmann distribution makes. In order to resolve this contradiction, the spin-lattice relaxation is defined, which is the mechanism that reverses the saturation state back to thermal equilibrium. In this case, the rate of change of the populations becomes $\frac{dn}{dt} = -\frac{n-n_0}{T_1}$, where T_1 is called as the spin-lattice relaxation time.

Bulk magnetization and Bloch equations

The information that is presented in above sections for a single electron can be extended to describe an ensemble of the non-interacting spins in a sample. In order to do that, the vector sum of the individual spin magnetic moments of the bulk sample is defined as a new vector, **M**, the bulk magnetization vector (Figure 1-7). When there is no field applied, the spin vectors are randomly oriented within the allowed spin states which is limited by the two cones that the motion with the *Larmor frequency* creates in Figure 1-7 (A). When a static uniform field is applied, at equilibrium according to the Boltzmann prediction, more of the spins would be aligned in the field direction and **M** would be in the direction of the external magnetic field as shown in Figure 1-7 (B). In order to distort this equilibrium state, a new field, **B$_1$** is applied which is oscillating with the Larmor frequency of the observed spins and perpendicular to the static field. After the microwave radiation is applied the resonance condition is satisfied and the amplitude of **M** is changed and goes back to the equilibrium state with a rate of T_1, the spin-lattice relaxation time (Figure 1-7 (C)).
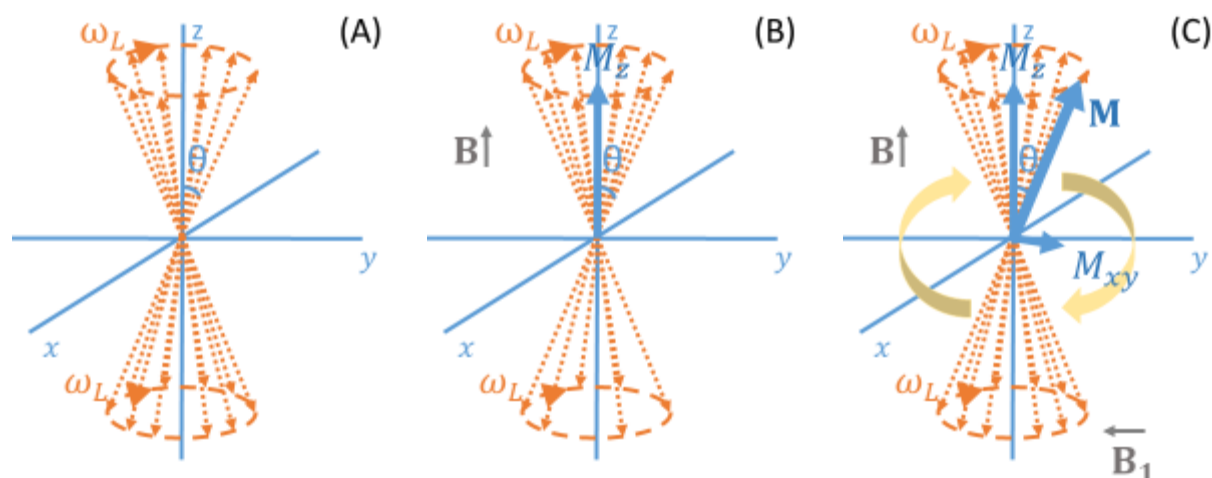
Figure 1-7 Figure depicting the net magnetization vector (**M**) in a bulk sample under three conditions: (A) **M** is equal to zero when there is no uniform magnetic field is applied. The individual spin magnetic moment vectors (dashed orange arrows) are randomly oriented among the allowed spin states (two orange cones) that is formed by the precession of the magnetic moment vectors about z-axis with a frequency ω_L. (B) In the presence of a uniform magnetic field in z-direction (**B**) the population of the spin magnetic vectors that is oriented with the field would outnumber the ones that are oriented against the field, and **M** would be in the z-direction (M_z). (C) In the presence of a uniform magnetic field and an oscillating field (B_1). After the resonance condition is met, the oscillating field would induce the "flipping" of the spin orientations (yellow arrows) by changing (i) the amplitude of **M**, and (ii) the orientation of **M**, with the components oriented along the Cartesian coordinates (M_z, M_{xy}). The state of **M** then be reserved back to equilibrium state in time $^1/_{T_1}$.

The **M** vector is directly proportional to the previously defined variable n, hence the rate of change equation for n applies to **M** also. Therefore, the rate of change of the 3 components of **M** is given by,

$$\frac{dM_x}{dt} = -\frac{M_x}{T_2}$$
<div align="right">Equation 1-11</div>

$$\frac{dM_y}{dt} = -\frac{M_y}{T_2}$$

$$\frac{dM_z}{dt} = -\frac{M_z - M_0}{T_1}$$

where T_2 is defined as the spin-spin relaxation time specific to the transverse magnetization in the xy plane. If Equation 1-11 is solved using the torque equation:

$$\frac{dM_x}{dt} = \omega_L M_y - \frac{M_x}{T_2}$$
<div align="right">Equation 1-12</div>

$$\frac{dM_y}{dt} = \omega_L M_x - \frac{M_y}{T_2}$$

$$\frac{dM_z}{dt} = -\frac{M_z - M_0}{T_1}$$

This set of equations given in the Equation 1-12 are the Bloch equations that are expressing the net magnetization of a bulk sample placed in an oscillating magnetic field (Figure 1-7).

EPR lineshape

All the concepts that are introduced so far have a combined effect that defines the EPR lineshape. The EPR lineshape itself is the solution of the Bloch equations along the axis chosen. The longitudinal component of the magnetization is not detected with the conventional EPR setups, however the transverse components of the magnetization; M_x and M_y can be detected simultaneously. The detection occurs with a microwave reference signal shift of 90^0 between the two components which produces a complex signal of the form: $(-M_y + iM_x)$. For the detection either y-axis (in phase component) or the x-axis (out-of-phase component) can be used which produces an absorption or a dispersion curve, respectively (**A** and **B** in Figure 1-8). In most of the cases, only the absorption spectroscopy is recorded because of its relatively higher amplitude and hence better signal-to-noise (SNR).
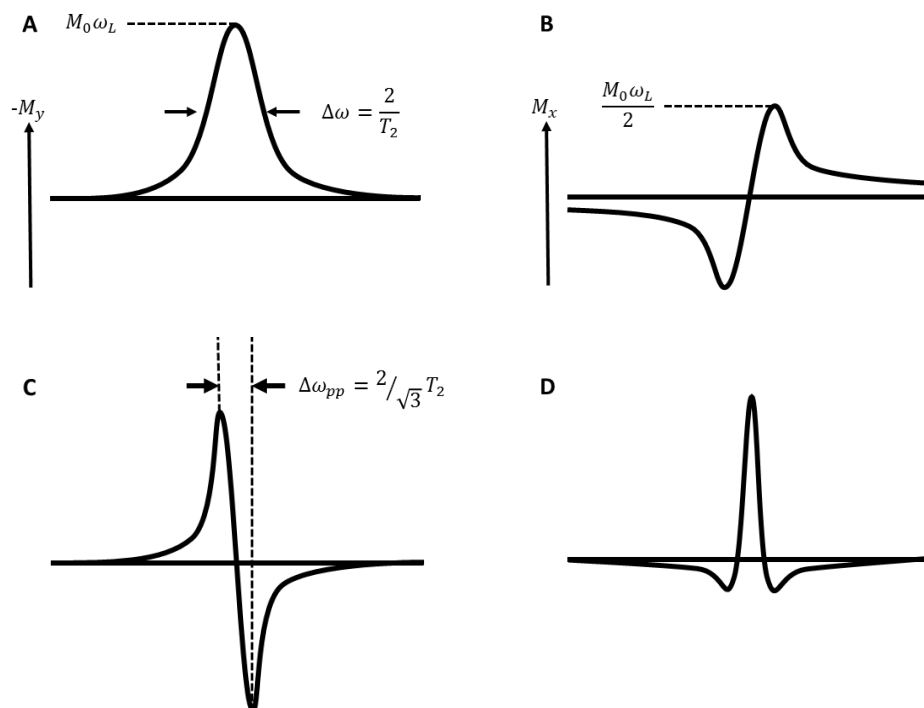
Figure 1-8 Line shapes that illustrate the solutions of Bloch equations among *y*-axis (**A**) and *x*-axis (**B**), that are called as absorption and dispersion spectra, respectively. The absorption spectrum which is in the Lorentzian form has a maximum amplitude of $M_0\omega_L$ where M_0 is the equilibrium magnetization and a half-of-maximum width of $\frac{2}{T_2}$. The dispersion spectrum has half of the maximum amplitude of the absorption curve. The first-derivative line shapes of the **A** and **B** are illustrated in **C** and **D**. Because of the instrumentation that is explained in the next section instead of the absorption curves, their first derivatives is produced by the EPR. The peak-to-peak width of the derivative of the absorption signal (ω_{pp}) is given by $\frac{2T_2}{\sqrt{3}}$. The dispersion curve, and hence its derivative signal is often not chosen for the detection because of the less signal amplitude.

The shape of absorbance curves and their positions are defined by the anisotropy in g and A. The g-anisotropy sets a range of magnetic field where the absorption can occur, by causing the peaks occur at the principal g-tensor component values through the field. The anisotropy of the hyperfine interaction causes the split features to have shapes that are different from each other.

The broadening of the spectral lines are a result of the spin-lattice relaxation phenomenon. The spectral lines, which would be infinite lines otherwise, becomes broader curves, because of the finite lifetime of the spin states before going to the saturation state. The width of the curve is proportional with $1/T_1$ and $1/T_2$, and only with $1/T_2$ in the nonsaturating limit (see the width of the absorption curve at the half of its maximum in Figure 1-8, **A**). There is also another variable defined as the rotational correlation time (τ_c) that affects the width of the broadening. It is a term that depends on T_1, T_2 and the elements of the g, and A tensors. It is introduced to take the effect of rotational diffusion on the relaxation time into consideration [58]. The signal is presented in the first-derivative form (**C** and **D** in Figure 1-8) because of the technical reasons which will be explained in the next section.

Phase-sensitive detection and field-modulation

In order to enhance the signal sensitivity, the CW-EPR spectra are produced through the phase sensitive detection and field modulation. Phase sensitive detection allows to differentiate the dispersion and absorption signals. The frequency of the detected noise is controlled by the field modulation: A small sinusoidal field that has a linear time dependence is produced, and scans through absorption curve to detect whether it is increasing or decreasing. The resulting curve corresponds to the derivative of the absorption curve directly, and is shown instead of the absorption curve itself (**C** and **D** in Figure 1-8). The modulation frequency should be big enough to maintain a good signal to noise ratio, however should be smaller than the width of the EPR derivative line (ω_{pp} in Figure 1-8, **C**).

1.2.2 Nitroxide Spin Labels

The molecules that have no intrinsic unpaired electrons cannot be studied using EPR spectroscopy. In such cases, these molecules can be modified to become paramagnetic and EPR detectable artificially. This is achieved by using the stable radicals which are referred as the spin probes when they are not attached to the molecules of interest, or spin labels when they are attached covalently (a.k.a. site directed spin labelling) to the molecules of interest [55]. Nitroxide radicals have a very common usage as the spin labels, often with a cysteine-specific ligand [56]. As an example for the usage of the Nitroxides as the spin probes, TEMPO radicals can be considered (Figure 1-9), which are commonly used to investigate the properties of membranes and the phase transitions dynamics [59]. Structurally, the nitroxides have the unpaired electron shared between the nitrogen and oxygen in nitrogen centered ring, and stabilized with the adjacent methyl groups. In this section, paramagnetic properties of the nitroxides will be introduced. Nitrogen has spin quantum numbers (m_l) equal to -1, 0 and +1, meaning that there are 3 allowed spin orientations (Figure 1-9). Each of the two energy levels of the electron are further split into 3 levels because of the hyperfine interaction of electron and nucleus, which create 3 peaks in the absorption spectrum (Figure 1-9).
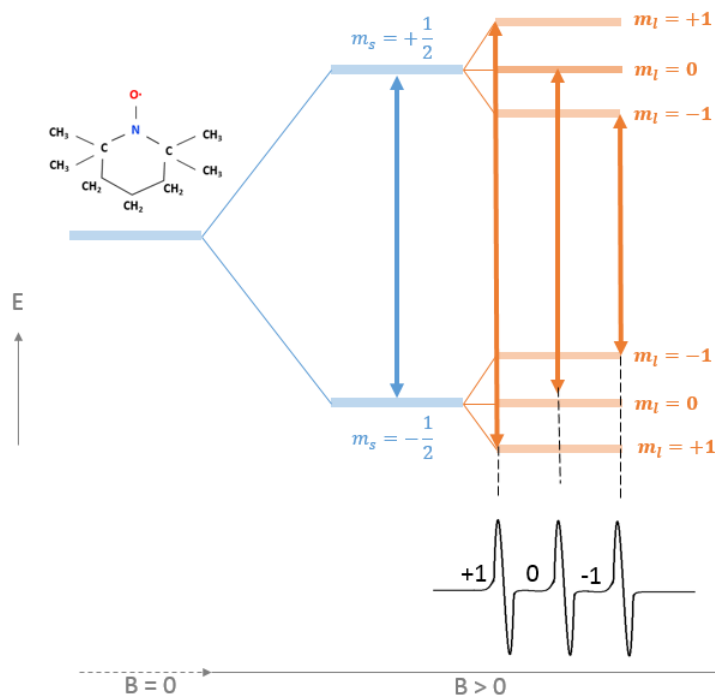
Figure 1-9 The energy splitting of a nitroxide spin probe. The energy splitting that is associated with the m_s quantum numbers (blue bars) in the external field (B) undergoes a further splitting (orange bars) because of the hyperfine interaction with the Nitrogen nucleus associated with the m_l quantum numbers. The corresponding derivative absorption spectrum is given below the energy diagram. The structure of TEMPO is also given in the figure.

Both $\hat{g}$, and $\hat{A}$ are diagonal for the Nitroxides. The unpaired electron density is localized in the p_z orbital of the N-O bond and oriented along the molecular z-axis. The values of the diagonal elements of the both tensor is determined for most of the Nitroxide spin labels. As stated in the above sections, the anisotropy in $\hat{g}$, and $\hat{A}$ causes each peak to have different broadenings and the amount of broadening is a function of T_2, which primarily depends on the tensor values and τ_c. For nitroxide probes in solution, the manifold broadening is directly proportional with the τ_c. Various models at various time scales have been proposed to describe and model the EPR line shapes in order to extract the information about the motion parameters of the probes in solution.

1.3 The EPR spectrum of Co(II)-substrate radical pair

In this study, one of the main focuses is the time-dependence of the CW-EPR spectrum of the Co(II)-substrate radical pair. In this section, the characteristic features of this spectrum (Figure 1-10) will be introduced in terms of the EPR theory information that is given in the section 1.2.

The paramagnetic features that are seen in the EPR spectrum of the Co(II)-substrate radical pair originates from two different spin populations: Co(II) and substrate radical. The EPR spectrum of the free Co(II) when there is no other paramagnet is given in the Figure 1-10 (top). The spectrum has an axial symmetry with the $g_x = g_y > g_z$, where the axial components correspond to the $g_{//}$ features in the high field, and the z-component corresponds to the $g_\perp$ in the low-field regions. The nuclear spin of the cobalt ion $(I = {}^7\!/_2)$ creates the 8 hyperfine splitting, and the interaction of the d_z2 orbital with an axial nitrogen ligand (see Figure 1-1 for the structure of the coenzyme) forms 3-fold split of each of the 8 hyperfine lines. The first two low-field hyperfine lines overlap with the $g_\perp$ peak and becomes difficult to detect with the X-band frequency resolution.
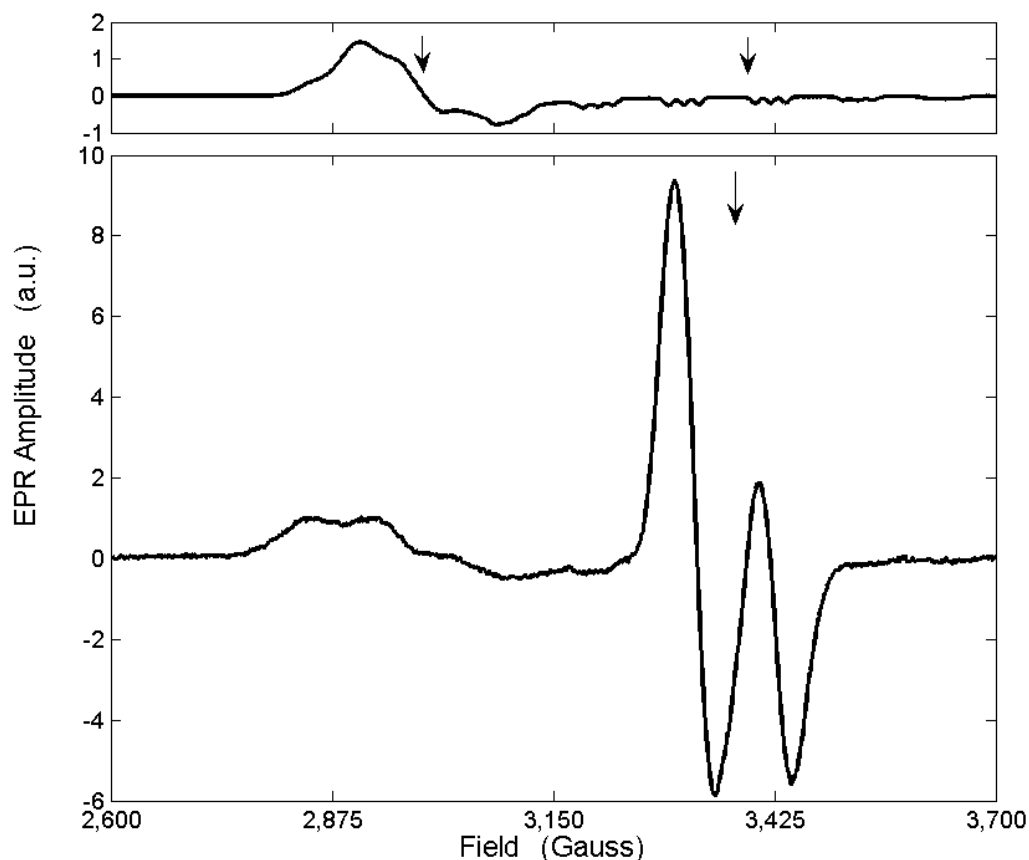
Figure 1-10 Top: The EPR spectrum of the free Co(II). The $g_\perp = 2.26$ and $g_{//} = 1.99$ position is shown with arrows. EPR conditions: microwave frequency, 9.447 GHz; microwave power, 20 mW; magnetic field modulation, 10 mT; modulation frequency, 100 kHz. Bottom: The EPR spectrum of the Co(II)-substrate radical pair at 120 K. The $g_{//} = 2.00$ position is shown with an arrow. EPR conditions: microwave frequency, 9.449541 GHz; microwave power, 20 mW; magnetic field modulation, 10 mT; modulation frequency, 100 kHz.

In the Co(II)-substrate radical pair system, two paramagnetic centers are coupled through the weak and strong interactions. The weak coupling is formed through the dipole-dipole interaction, and the splitting that it creates often not visible with the X-band CW EPR spectroscopy due to the detected noise. The strong coupling that is the spin-spin interaction between the radical and the unpaired d_z2 electron of the Co(II) creates the characteristic biradical triplet EPR spectrum which is shown in Figure 1-10, bottom.

The scope of the project

Although the EAL minimal mechanism has been studied for more than 40 years [60-63], it still holds many controversies today. The controversies are recently concentrated on portraying the role of the solvent-coupled enzyme dynamics on the EAL catalytic action. Studies about the structural resolution of the active site [23, 25, 43, 44] and the dynamic transitions that the biological systems possess [64-66] have provided valuable information about these controversies. Having a better handle on the kinetics of the single steps in the EAL minimal mechanism is required to complement the structural and dynamical data. CW-EPR has been a suitable tool in order to achieve this goal.

EAL reaction cycle has the Co(II)-S• pair state as the only accumulating paramagnetic species. The previous time-resolved CW-EPR studies have been concentrated on the kinetics of the enzyme: (1) from ternary complex to the Co(II) S• pair state accumulation (steps **1-3** in Figure 1-5) [67], or (2) from accumulated and trapped radical to the product states (step **3-6** in Figure 1-5) [68, 69]. In other words, the former showed the formation of the Co(II)-S• pair, whereas the latter showed the decay of it.

The studies that focused of the formation of the Co(II) S• pair state showed that the radical pair separation and the first Hydrogen transfer steps (**1** and **2** in Figure 1-5) are synchronous, which is also supported by the transient nature of the Ado• and the hydrogen isotope results indicated that the radical rearrangement step (**3** in Figure 1-5) is the rate-limiting step [31, 67, 70]. These two features of the formation kinetics yielded the rapid formation and accumulation of the Co(II) S• pair state, which makes it perfectly suitable for cryotrapping. When cryotrapped, the Co(II) S•

pair state can then be annealed at higher temperatures to monitor the kinetics of the subsequent steps in the minimal mechanism [68, 69].

In the previous CW-EPR studies on the EAL kinetics, the instrument dead time relative to the observed kinetics has set a limit on the temperature range at which the experiment is held [67-69]. Until now, the highest temperature that has been reached in a time-resolved CW-EPR study is 230 K, which is relatively low compared to the physiological conditions [68, 69]. One way to overcome this limitation is to use a slower substrate analogue in order obtain a slower kinetics [67].

Among the challenging questions that are summarized in the above sections about the structural, mechanistic and the energetic features of the AdoCbl-dependent enzymes, this study aims mainly to address the unknowns of the kinetics of the (a) rearrangement of the substrate radical and (b) Co-C bond cleavage in the EAL holoenzyme (Figure 1-5). Two different spectroscopic approaches will be employed to achieve (a) and (b); electron paramagnetic resonance (EPR) and ultraviolet-visible（UV-vis）spectroscopy, respectively. With this kinetics information, the ultimate aim is to contribute the kinetic resolution of the single steps in the minimal reaction mechanism, and elucidate the effects of the enzyme-solvent coupled dynamics on the reaction kinetics.

This study aims to:

(i)   Manifest the kinetics of this AdoCbl-dependent enzyme, EAL, with a single step resolution and project the notions that are obtained by low-temperature studies to the kinetics that is observed under the physiological temperatures.

(ii)   Associate the kinetics of the enzyme catalysis with the solvent dependent enzyme dynamics.

The plan to achieve these goal, respectively:

(i)   Extending the temperature range of the time-resolved kinetics studies to the higher temperatures by utilizing the slower substrate analogues; (S)-2-aminopropanol (2-AmPrOH) and ethylene glycol (EG). Using these substrate analogues makes the monitoring of the reactions feasible at higher temperatures; T= 220-255 K with 2-AmPrOH using CW-EPR as the instrument, and T= 273-298 K with EG using the optical spectroscopy as the instrument.

(ii)   Using nitroxide spin probes to understand the motion of the solvent and the effect of this motion on the active site components.

Chapter 2

Characterization of the Radical Rearrangement Reaction in B12-Dependent Ethanolamine Ammonia-Lyase Probed over the temperature range of 210-250 K by using Aminopropanol as Substrate

2.1 Background

EAL is an adenosylcobalamin (AdoCbl, coenzyme B_{12})-dependent enzyme [13, 14] that facilitates the conversion of ethanolamine and both enantiomers of 2-amino-1-propanol [27, 71] represented by the multi-step minimal mechanism (Figure 1-5) that has been established through both steady-state [28, 72, 73] and transient-kinetics [29, 67-69, 74] studies. The forward reaction starts with the homolysis of the Co-C bond between the central Co(III) in AdoCbl and the upper axial ligand, 5′-deoxyadenosine which forms a low-spin Co(II) and a 5′-deoxyadenosyl radical (Step 1 in Figure 1-5). The high reactivity of this radical is utilized by the enzyme as a hydrogen exchange agent from substrate (Step 2 in Figure 1-5) and to the substrate radical (Step 4 in Figure 1-5), which first forms the substrate radical and then the product, respectively. The substrate radical accumulates in the steady-state turnover and couples with the Co(II) to produce a distinctive EPR signal which can be observed time-dependently in two ways: (1) the formation of this signal that is the accumulation of the Co(II)-substrate radical pair in the DMSO/water cryosolvent mixture (Step 1-3 in Figure 1-5) [67], or (2) the decay of this signal that is the reaction of the cryotrapped Co(II)-substrate radical pair through the radical rearrangement step and onwards [68, 69, 73, 75, 76]. The previous studies for the latter, characterize the kinetic features of the decay of the Co(II)-substrate radical pair between $T = 193 – 230$ K, and also indicate a protein dynamical transition which is stated as the protein-glass transition at $T = 214 – 219$ K [76]. We used the time-resolved continuous wave-EPR (CW-EPR) for the characterization of the kinetics of the ethanolamine ammonia lyase (EAL, EC 4.3.1.7) from *Salmonella typhimurium* over a temperature range of $220 – 250$ K. Our results uncover the temperature dependence of the kinetic and energetic features of the EAL catalytic reaction, and when interpreted in the light of dynamics of the solvent

coupled protein dynamics and complemented with results of the previous studies, becomes rather an indirect measure of the effect of the solvent-coupled protein dynamics on the enzyme catalytic function.

In this study, we characterized the radical chemistry upon the formation and accumulation of the Co(II)-substrate radical pair in the reaction of substrate 2-aminopropanol. We used the slow-reacting substrate analogue, 2-aminopropanol $(k_{cat} = 0.12 \pm 0.01 \ s^{-1}$ for 2-aminopropanol compared to the $k_{cat} = 30.0 \pm 0.1 \ s^{-1}$ for aminoethanol [60]). Our results showed that the 2-aminopropanol derived Co(II)-substrate radical pair state present a suitable system for quantifying the decay of the Co(II)-substrate radical pair. The decay to the EPR-silent product states follows a biexponential behavior, with the temperature-dependencies of the observed slow and fast phases undergoing a transition which could originate from a protein dynamical transition that is stated in the previous studies [76, 77]. In addition, the low-temperature conditions revealed a second, non-native pathway of radical pair decay, which is also following a biexponential reaction kinetics. Also, utilizing a slower substrate analogue enabled us to reach to the higher temperatures that have not been accessible so far due to the dead-time of the spectrometer. Hence, we have reached a new, and higher temperature regime to understand the kinetics and the dynamics of the decay of Co(II)-substrate radical pair. We also proposed a three state – two step model to encounter the microscopic rates that is associated with the single reaction steps in the minimal reaction mechanism, which yield a more accurate depiction of the observed transition in the temperature-dependent kinetics of the enzyme.

2.2 Materials and Methods

2.2.1 Enzyme Preparation

EAL of *S. typhimurium* (EC 4.3.1.7) was overexpressed in *Escherichia coli* and purified according to the previous descriptions [41, 78]. Alcohol dehydrogenase/NADH coupled spectrophotometric assay is performed to determine the enzyme activity, which is 20−30 μmol/min/mg with aminoethanol as the substrate.

2.2.2 Sample Preparation

All chemicals were purchased from commercial suppliers (Sigma-Aldrich or Fisher). EPR samples were prepared on ice and under red light. The EAL to 120 μM and the coenzyme to 480 μM were mixed in a 10 mM potassium phosphate buffer (pH 7.5) and transferred to the 4 mm outside-diameter (OD) EPR tube. After a 1-minute incubation, the 2-aminopropanol to 10 mM was added directly to the EPR tube and this started the reaction to accumulate the Co(II)-substrate radical pair. The sample was mixed immediately after the addition of the substrate using a vortexer for 4 s, then quickly put in liquid nitrogen – isopentane temperature bath for cryotrapping the Co(II)-substrate radical pair at $T \approx 150$ K. The time that passed after the addition of the substrate until the cryotrapping is 10 - 12 s. The sample preparation protocol was similar to the previous studies [68, 69, 75, 76], except for the direct addition of the substrate to the EPR tube, and instead of mixing the reactants with protein in a test tube and then transferring to the EPR tube. With this method, the time between the substrate addition and the cryotrapping was decreased significantly. This decrease yielded an up to 30% increase of the EPR amplitude of the Co(II)-substrate radical pair.

2.2.3   Continuous-wave EPR spectroscopy

The CW-EPR experiments were performed on a Bruker E500 EPR spectrometer with a Bruker ER4123 SHQE X-band cavity resonator. The temperature control is maintained by an assembly based on the N_2 gas flow (which is controlled by a ball flow indicator; King Instrument Co.) from the 250 LN_2 storage dewar through a coil which is placed in an open-lid, 4-L dewar containing the ethanol-dry ice cooling bath at approximately 200 K. This is a temperature that is close to the temperatures at which the decay experiments are held (220 – 250 K), and the decay temperatures could be maintained with a less of a gas flow rate (20 – 30 cc/min) compared to that of LN_2 temperature bath (40 – 50 cc/min). This not only provides a more effective use of the N_2 gas but also the temperature is observed to be more stable in time when the flow is not too high. Also, the runtime of the experiments were not limited, owing to the ability to continuously refill the cooling bath.

2.2.4   Time-resolved EPR Spectroscopy

Before each experiment, the decay temperature is calibrated with a ± 0.5 K precision in the ER4131VT cryostat system in the Bruker E560 spectrometer with Oxford Instruments ITC503 temperature controller with a CernoxTM Probe. Once the temperature is maintained at the cavity, an only-buffer sample is loaded to pre-tune the microwave bridge which eases the tuning with the cryotrapped Co(II)-substrate radical pair state samples, and hence decreases the spectrometer dead-time that is mostly caused by the tuning process. The EPR sample is loaded to the pre-tuned cavity directly at the decay temperature, and the microwave bridge is tuned one more time in about 20 – 40 s, which is a relatively small time span compared to the full decay time of 3 x 10^4 – 5.4 x 10^4 s. The time from the initiation of the acquisition and completing the first sweep is a total of

41.48 s which consists of a 20.97 s conversion time and a 20.48 s sweep time (5.12 ms time constant). The delay time between each spectrum is 50-120 s. The center field is at 3100 G, and the width for the magnetic field sweep is 1200 G which is recorded at 1024 point resolution. The decay measurements are held at the 220 – 250 K, with 5 K increments, and each temperature point is measured at least 3 different times. The EPR conditions are the same for all the experiments, and set as following; microwave frequency, 9.3413 GHz; microwave power, 20 dB; magnetic field modulation, 10 mT; modulation frequency, 100 kHz.

2.2.5 Kinetic Analysis

The EPR spectrum of the Co(II)-substrate radical pair in EAL has two predominant features: one low-field peak from the low-spin Co(II) at $g\sim2.2$ and a high-field feature around $g\sim2.0$ that is associated to the substrate radical. The change in the amplitude of these features is observed as a measure of the decay of the Co(II)-substrate radical pair. The EPR spectra are collected until the EPR peak-to-trough amplitude of the substrate radical feature decayed to (8.8 ± 5.8) % of its initial value. The acquired spectra are smoothed by cubic spline interpolation, in order to overcome the low signal to noise ratios that are seen towards the end of the decays.

The observed decays of the amplitude values are fitted to a biexponential function by using the expression:

$$A_i(t) = A_1\, e^{-k_1 t} + A_2 e^{-k_2 t} + C \qquad\qquad \text{Equation 2-1}$$

where A_i is the observed EPR amplitude, A_1 and A_2 are the amplitudes for the two first-order rate constants, k_1 and k_2 respectively, and C is the constant representing the baseline amplitude value at $t = \infty$. The observed EPR amplitudes are normalized to their $t = 0$ values from the fit ($A_i(0) =$

$A_1(0) + A_2(0))$ for the comparison of the different decays in terms of the relative amplitude parameters on a common scale.

$$A(t) = \frac{A_i(t) - C}{A_i(0) - C}$$
<div align="right">Equation 2-2</div>

where $A(t)$ is the normalized amplitude, $A_i(0)$ is the amplitude point at $t = 0$ and C is the constant parameter found by the fitting to Equation 2-1. The normalized EPR amplitudes were then fitted to a biexponential function:

$$A(t) = A_s e^{-k_s t} + A_f e^{-k_f t}$$
<div align="right">Equation 2-3</div>

where $A(t)$ is the normalized EPR amplitude, k_s and k_f are the slow and fast first-order rate constants, and A_s and A_f are their corresponding normalized component amplitudes.

2.2.6   Optical Measurements

Sample Preparation

The complete preparation and measurement is performed under red dim light to prevent photolysis of the coenzyme. The EAL is pre-mixed with 50 μl of the buffer, and sonicated for about 15 s for a clear transmission of the light. All the sample ingredients are held in a temperature bath that matches with the temperature of the cuvette-holder in the UV-visible spectrometer, in which the Co(II)-substrate radical pair decay will be observed. Substrate 2-AmPrOH is added to

12 µM in the EAL (1 mg/ml) and AdoCbl (12 µM) mixture in a 1.5 ml visible-range quartz cuvette to start the kinetic measurement. The first 20 s after the addition is lost to the mixing of reactants, and the rest is collected as the increase in the absorption of Co(III) at 525 nm.

UV-visible Spectroscopy

The temperature-controlled UV-visible spectroscopic measurements are performed on a Shimadzu UV-1601 optical bench spectroscopy with a Neslab refrigerated circulating bath of a water – methanol (as an antifreeze) mixture connected to the metal cuvette holder through an insulated tubing. In order to prevent the fog formation, dry gas (N_2) flow at 20 cc/min maintained in the sample compartment. The experiments were performed at 278.25 K in the 300-700 nm wavelength range with the scan speed set at slow (about 460 nm/min) for the spectral acquisition. For the one-wavelength kinetic measurement the wavelength set at 525 nm, and recorded at every 0.1 seconds.

2.3   Results

2.3.1   Time-dependence of the Co(II)-substrate radical pair EPR spectrum following temperature-step reaction initiation

The EPR spectrum of the Co(II)-substrate radical pair in EAL and its dependence on time following the *T*-step initiation at 230 K is shown in Figure 2-1. The zero-time EPR line shape in Figure 2-1 is characteristic of the Co(II)-substrate radical pair formed with 2-aminopropanol substrate [28, 29, 79]. The Co(II) features are broadened compared to the isolated Co(II) by the inhomogeneous broadening of the unpaired electron that is localized on substrate C1, and has the most predominant peak at $g_\perp \approx 2.26$. Also, substrate radical creates a split signal around $g_\parallel \approx 2$

through the weak interactions, such as dipole-dipole coupling and isotropic exchange. For the structural characterization of the Co(II)-substrate radical pair, theoretical simulations can be performed on the EPR line shape to obtain the zero-field parameters; D and E that measure the dipolar interaction along the *z*-axis and the differences of the magnetic dipole interactions along *x*- and *y*-axes, respectively. For an axial system, E is accepted as zero, so that D becomes the only parameter that includes the dependence between the two electrons (R_{ee}). The simulation results for the 2-aminopropanol-generated Co(II)-substrate radical pair gave a distance of $R_{ee} = 11.1$ Å between the substrate radical and the Co(II) in the cobalamin [30]. Isotropic exchange interaction represents the mutual orientation of the electrons in the overlapping orbitals and yields either broadening of the EPR spectra when the interaction is inter-molecular, or appearance of the new EPR lines in the spectrum when the interaction is intra-molecular (e.g. for biradical). According to the previous simulations, the 2-aminopropanol-generated Co(II)-substrate radical pair has an antiferromagnetic exchange interaction constant of $|J| = 324$ MHz [30, 42].
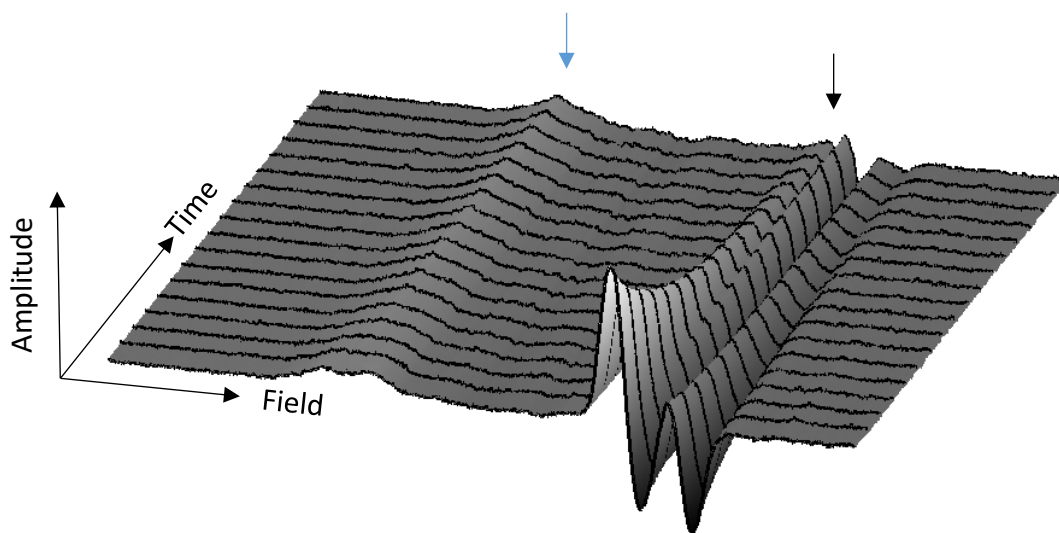
Figure 2-1 Dependence of the raw EPR spectrum of the Co(II)-substrate radical pair in EAL on time, that is decayed at 230 K. The $g = 2$ position is shown with a black arrow, and $g = 2.26$ position is shown with a blue arrow. EPR conditions: microwave frequency, 9.3413 GHz; microwave power, 20 mW; magnetic field modulation, 1.0 mT; modulation frequency, 100 kHz.

During the course of the decay of the Co(II)-substrate radical pair state, as the Co(II) and radical signal amplitudes decrease, two new features emerge; a narrow radical signal at about $g_{||} \approx 2$ position, and a new Co(II) peak around $g_{\perp} \approx 2.26$. This indicates the formation of a non-native Co(II) and radical species. The EPR amplitude of this Co(II) and radical species reaches a constant level and stays stable during the time scale of the kinetics experiments ($1.3 \times 10^4 - 6.7 \times 10^4$ s). The results show that the native Co(II)-substrate radical pair decays following the T-step and is absent at long times, and that a new Co(II) and radical species increases in amplitude, over the

same time period. In order to resolve the decay and growth kinetics of the two species, a spectral deconvolution approach is required.

2.3.2   Deconvolution of the time-dependent Co(II)-radical EPR spectra

In order to obtain the spectra of the native and non-native species separately, a deconvolution routine was applied on the Co(II)-substrate radical EPR spectra. The deconvolution is based on the subtraction of the native-only features from the raw Co(II)-substrate radical spectra, and hence obtaining the EPR spectra of non-native species. Therefore, acquiring the native-only features was the first step. This was possible, because the non-native species appear over time, so the first spectra of the Co(II)-substrate radical pair decay at $t = 0$ s does not have any non-native features.

The second step was producing a time-dependent spectral series for the decay of the native-only features in the Co(II)-substrate radical spectra. The decay of the Co(II) peak has an overlap with the formation of uncoupled Co(II) peak at the $g_\perp$ region. On the other hand, the radical component of the Co(II)-substrate radical pair, which is located at the $g_{||}$ region, is not affected by this interference. Hence the decay of the peak-to-trough amplitude of the substrate radical signal is a representative of the time-dependence of the native reaction. The EPR spectrum of Co(II)-substrate radical pair at $t = 0$ s which is postulated to be free of any non-native features, is scaled to these amplitude values at each time point, in order to generate a time-dependent series of spectra that represents only the native reaction (Figure 2-2). This spectrum shows the decay of the Co(II) signal as well as the coupled Co(II)-substrate radical component. The generated "native reaction only" spectra series was then subtracted from the observed spectra to obtain the spectra series of the formation of the uncoupled species (Figure 2-3). Figure 2-2 and Figure 2-3 represent the

resulting native- and non-native-only spectral series for the decay of the Co(II)-substrate radical

pair at 230 K, respectively.
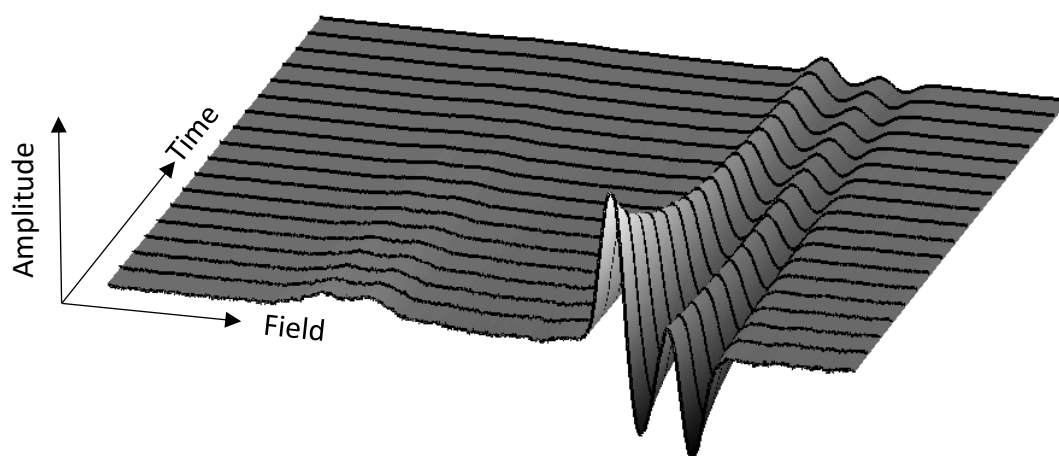
Figure 2-2 Time dependence of the deconvoluted "native-only" EPR spectra of the Co(II)-substrate radical pair at $T = 230\ K$. EPR conditions: microwave frequency, 9.3413 GHz; microwave power, 20 mW; magnetic field modulation, 1.0 mT; modulation frequency, 100 kHz.
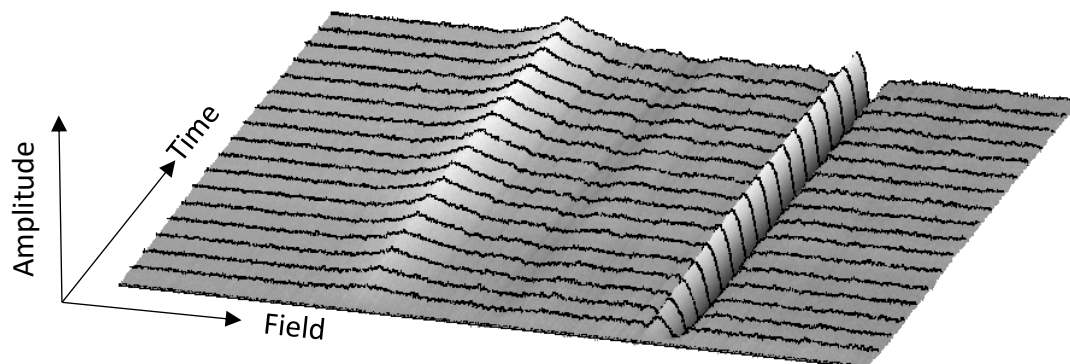
Figure 2-3 The time dependence of the deconvoluted EPR spectra of the uncoupled non-native reaction at $T = 230\ K$. EPR conditions: microwave frequency, 9.3413 GHz; microwave power, 20 mW; magnetic field modulation, 1.0 mT; modulation frequency, 100 kHz.

The deconvolution routine that is prescribed above is applied to all the time-dependent spectra that are collected between $T = 220 - 250$ K.

2.3.3   Time and Temperature dependence of the Co(II)-substrate radical pair decay

EPR spectroscopic measurements

Time dependence of the decay of the cryotrapped Co(II)-substrate radical pair was observed between 210 K and 260 K. The amplitude of the Co(II)-substrate radical pair is defined by the amplitude of the trough of the substrate radical amplitude in the $g_{||}$ region.   The trough

amplitude was used, because it is free of interference from overlap of the uncoupled radical signal. The observed decay of this amplitude value is plotted with respect to time for further analyses and fitting. In Figure 2-4, one decay dataset at each temperature is shown. The time axis is truncated at $t = 1.2 \times 10^4$ s which is when the 250 K decay ends. The decay curves at 255 K and the 260 K were stopped at the earlier times with respect to the rest of the data, because the completion of the decay occurs over a shorter time interval than the rest. The shape of the decay curves indicate a biphasic behavior, with a respectively fast loss of the initial amplitude within the beginning of the decay time, and a slower phase towards the end of the decay. The layout of the decay curves at different temperatures followed the expectation by having the fastest decay at the highest temperature, and vice versa. Moreover, the decays at the warmer (240 K to 260 K) and the colder temperatures (210 K to 230 K) are grouped together in terms of the observed kinetics.
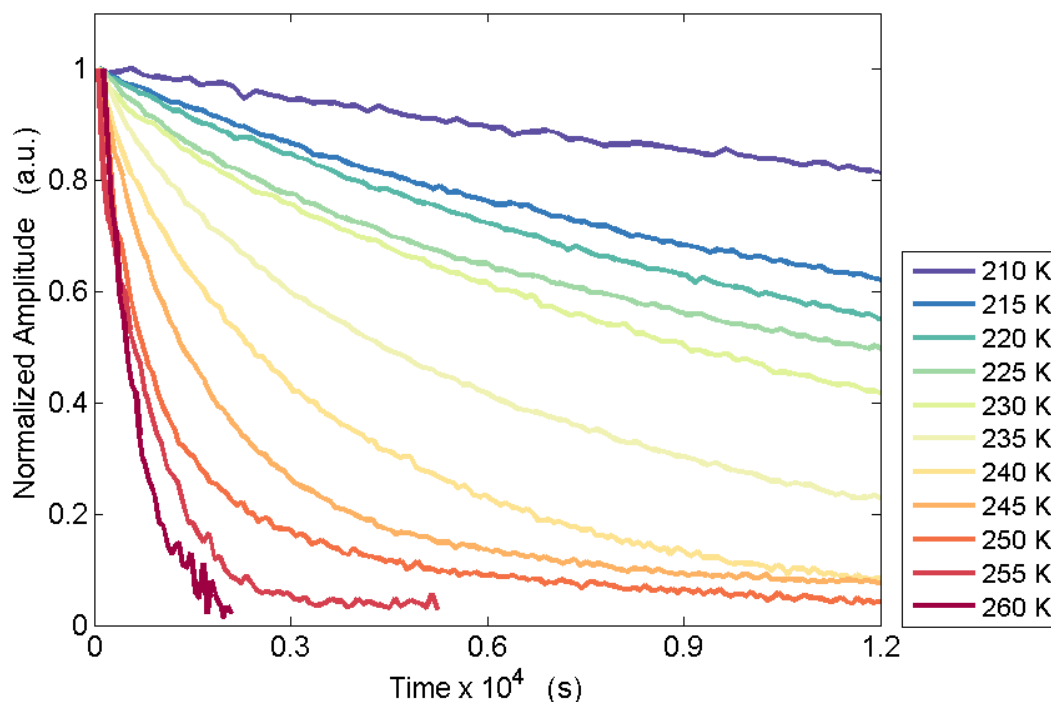
Figure 2-4 Time-dependence of the normalized EPR amplitude of the substrate radical pair state in EAL in the frozen aqueous solution from $T = 210$ K to $T = 260$ K. The EPR amplitude is calculated from the difference between the trough of the split feature around $g_{||} \approx 2$ region and the low-field baseline. The data are truncated at $t = 1.2 \ x \ 10^4 \ s$ to match the full time scale of the decay of the substrate radical pair state in EAL at $T = 250$ K. See Figure 2-9 for the complete decay curves without the truncation.

Optical spectroscopic measurements

A high-T decay at 278 K, which lies in the physiological, fluid-solution temperature range, was achieved by observing the Co(II)-substrate radical pair kinetics by using UV-visible spectroscopy. UV-visible spectroscopy was used, because of the dramatic loss of amplitude of the EPR signal, under the higher T, solution conditions. UV-visible spectroscopy detects the absorption spectra of the cobalamin species in the EAL minimal mechanism. The Co(II) in the substrate radical pair is converted to Co(III) in the product species, and this creates a loss in

absorbance around 470 nm peak and an increase in absorbance around 525 nm shoulder, which is characteristic of the Co(II) to Co(III) conversion. The full absorption spectrum is collected two times, one before the addition of the 2-AmPrOH and other one from the end of the time-course data, which is shown in Figure 2-5. In this figure, the Co(II) to Co(III) conversion can be seen in the change of the peak absorbance values at the corresponding wavelengths (shown by arrows).
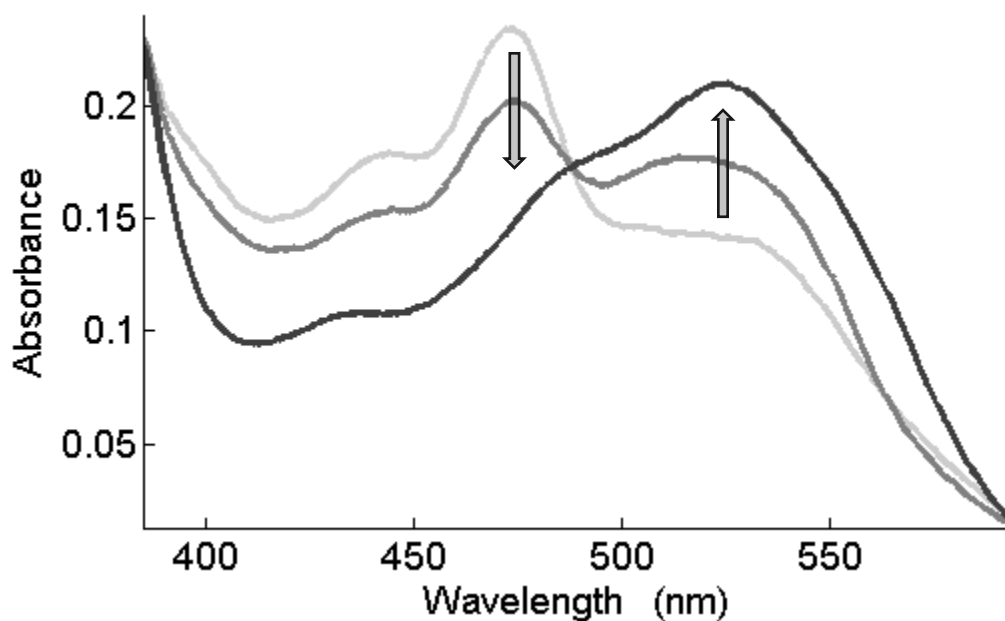
Figure 2-5 The absorption spectrum of the cob(II)alamin in the presence of the EAL before the addition of the substrate, 2-AmPrOH is shown in light gray line, and the formation of the absorption spectra of the cob(III)alamin formation after the addition of the 2-AmPrOH to the EAL and cob(II)alamin mixture is shown. The direction of the overlaying arrows show the direction of the change in the optical density at 470 nm and 525 nm.

The time-course data of the rise of the 525 nm cob(III)alamin absorbance peak is fitted to a single exponential function (Figure 2-6). The observed rate parameter ($k_{obs,UV}$) that is obtained from the single exponential fitting is 0.056 s^{-1}.This value is in accord with the previously reported

value (0.12 s⁻¹ at 298 K and 0.26 s⁻¹ at 300.15 K [14, 52]) and will be used as an additional

parameter to interpret the kinetic data that is obtained from the CW EPR spectroscopy.
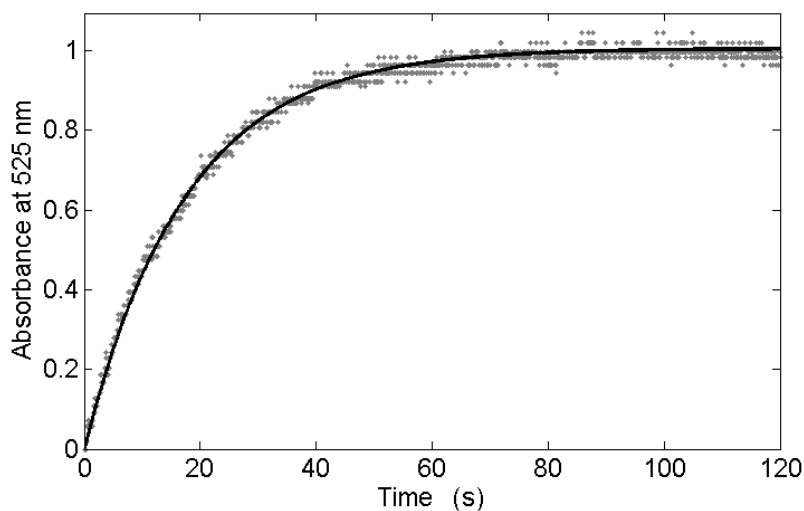
Figure 2-6 The time-dependent rise of the cob(III)alamin absorbance at 525 nm during the decay of the Co(II)-substrate radical pair as observed with UV-visible spectroscopy. The overlaid best fit single exponential function is shown in red.

Temperature dependence of substrate/product exchange with the active site

In the frozen aqueous solutions, EAL creates an environment, that surrounds the protein, that is known as the mesodomain within its boundaries with the crystal solvent [77, 80]. The mesodomain is an interstitial layer of solvent that lies between the protein and the ice grain boundaries of the frozen water. The mesodomain contains the solutes expelled from the ice crystalline domains during freezing, such as the 2-aminopropanol substrate and buffer [77, 80].

The mesodomain between the EAL and the ice-water structures is frozen, solid at $T \leq$ 220 K. Therefore, once the mesodomain is frozen, the decay of the Co(II)-substrate radical pair would not be interfered with the formation of new Co(II)-substrate radical pairs because the

diffusion of the free substrate radicals to the active site is blocked. In this section, this assumption will be tested in order to see whether the mesodomain starts *melting* at the selected decay temperatures.

To test the assumption, a decay was run at a relatively low temperature, 220 K, where the mesodomain is frozen. After the decay goes through the fast and slow phases with about 10% of the initial EPR amplitude remaining (blue spectrum line in Figure 2-7 and Figure 2-8), the temperature of the sample is increased to higher temperatures for 5 ± 1 min and then decreased back to 220 K to observe the change in the remaining EPR amplitude. If there is no fluidization of the mesodomain environment around the protein present, more of the Co(II)-substrate radical should decay than it would if the sample was kept at 220 K for the same time interval (green, red, and yellow spectral lines in Figure 2-7). On the contrary, if the solvent undergoes a transition from solid to fluid, around the protein, there should be new Co(II)-substrate radical pair species forming and an increase of the amplitude after the temperature jump as shown by the black dashed spectrum line in Figure 2-8. The experiment that is depicted here showed that the substrate-enzyme interface undergoes a transition that allows the binding of the free substrate to the active site in exchange for bound products. Therefore, the Co(II)-substrate radical pair decay data that are collected above 250 K have been eliminated from further analyses, because the melting of the mesodomain allows the free substrate to enter the active site, from solution, and new Co(II)-substrate radical pair species.
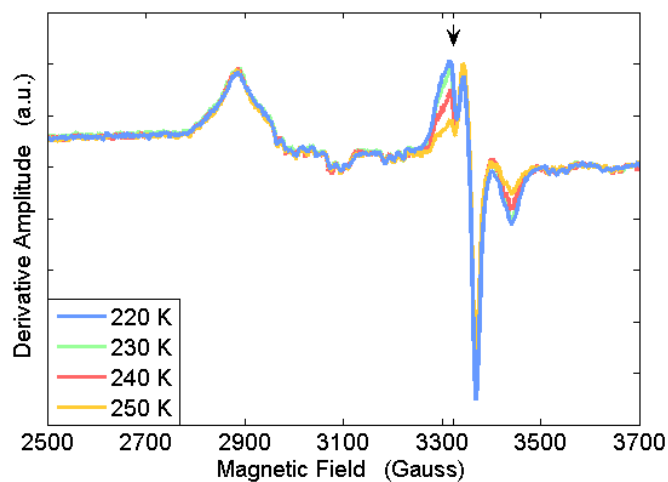
Figure 2-7 Decrease of the remaining EPR amplitude of the Co(II)-substrate radical pair state after decaying for 1.3×10^5 s at 220 K (blue line) after the cryostat temperature is increased from 220 K to 230 K, 240 K, 250 K (green, red and yellow line respectively).
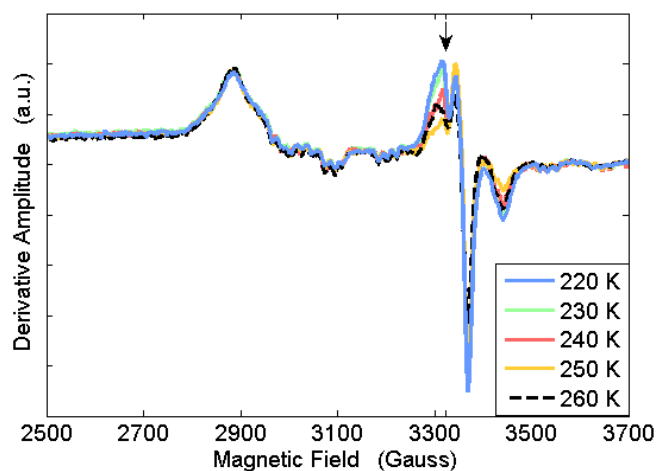
Figure 2-8 Emergence of a new Co(II)-substrate radical pair state population when cryostat temperature is increased to 260 K (black dashed line).

Kinetic fitting results of the Co(II)-substrate radical pair decay

The time-course data of the decay of the Co(II)-substrate radical pair decay at $T = 220 -$ 250 K were fitted to a biexponential function that is described in Section 2.2.5. The decay of the

Co(II)-substrate radical pair with the overlaid best-fit biexponential curves for representative data at 220 K, 230 K, 240 K and 250 K is shown in Figure 2-9. In this figure the decays are shown in their complete runtimes. At higher temperatures this limit is reached faster compared to the lower temperatures, hence the runtimes are shorter. The biexponential fitting was excellent at each temperature point with an average root mean square deviation value of 0.9981 ± 0.0015 for the fitting to the complete data sets at each temperature (Table 2.1).
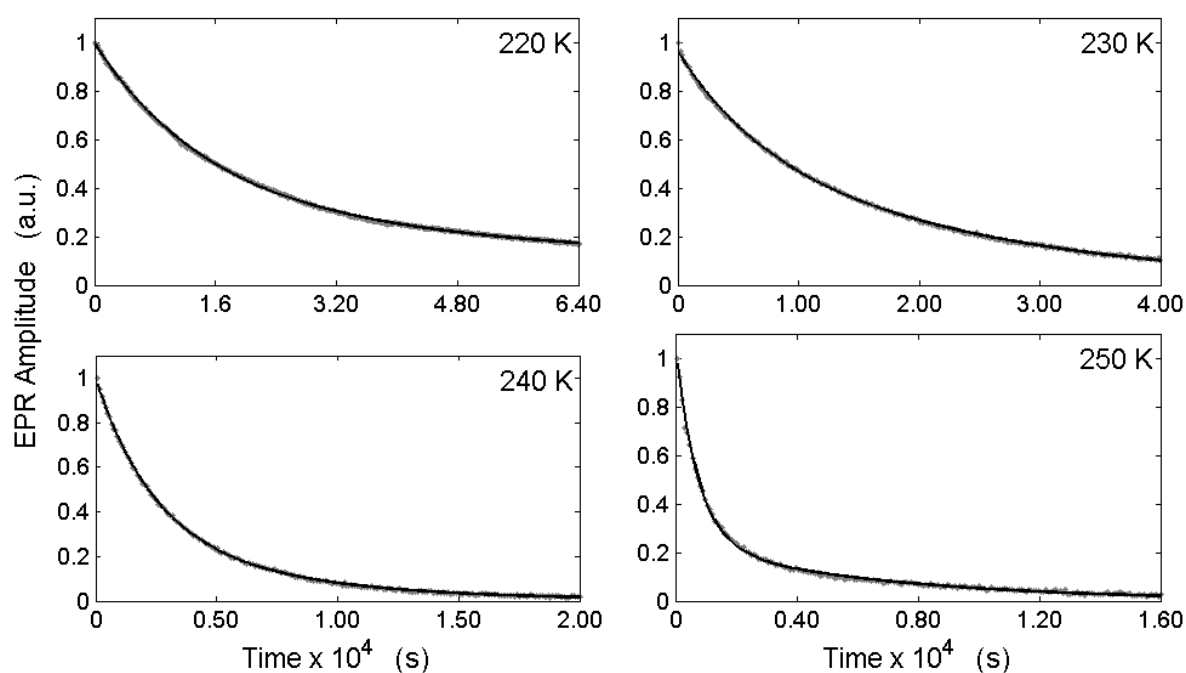
Figure 2-9 Decay of the amplitude of the (S)-2-aminopropanol-generated Co(II)-substrate radical pair state as a function of time at selected temperatures from 220 – 250 K and overlaid best-fit biexponential function (black line). The associated temperature values are given in the title of the plots.

The biexponential function that is shown in Equation 2-3 is fitted to the decay data between 220 K and 250 K. The fit parameters give the observed first order fast and slow rate constants and the relative percentages of the EPR amplitude that decay with these rate constants (Table 2.1).

Table 2.1 First-order rate constants and amplitude parameters for the biexponential fitting to the decay kinetics of the 2-aminopropanol-generated Co(II)-substrate radical pair between the temperatures 220 – 250 K*. Parameters represent the mean values, ± standard deviation, for at least three separate decay measurements.

T (K)	A_s	$k_{obs,s}$ x 10^{-4} (s^{-1})	A_f	$k_{obs,f}$ x 10^{-3} (s^{-1})	$R^{2\dagger}$
220	0.70 ± 0.05	0.21 ± 0.04	0.30 ± 0.05	0.17 ± 0.05	0.9976
225	0.70 ± 0.03	0.34 ± 0.04	0.30 ± 0.03	0.23 ± 0.01	0.9989
230	0.81 ± 0.10	0.85 ± 0.24	0.19 ± 0.10	0.62 ± 0.12	0.9994
235	0.79 ± 0.09	1.14 ± 0.04	0.21 ± 0.09	0.70 ± 0.22	0.9995
240	0.73 ± 0.12	2.61 ± 0.20	0.27 ± 0.12	0.92 ± 0.34	0.9993
245	0.13 ± 0.06	0.52 ± 0.16	0.87 ± 0.06	0.60 ± 0.03	0.9960
250	0.29 ± 0.08	1.15 ± 0.34	0.71 ± 0.08	1.36 ± 0.17	0.9964

* The 210 and 215 K decay data are not included in the analysis because the amplitude decayed to >50% of initial amplitude, and therefore, accurate two-component fits could not be obtained.
† R is the Pearson's correlation coefficient

The first treatment of the observed data was the empirical kinetic fitting, extracting the rate constants from the fits, and comparing the observed rate constants with the other type of data that is obtained from UV-visible experiments and literature. In the further analyses, the kinetics of the uncoupled signal that is described in the above sections will be examined in a similar approach, and a microscopic kinetic model will be implemented, in order to acquire the microscopic rate constant for individual reaction steps, instead of the observed, or empirical rate constants.

2.3.4　Time and temperature dependence of the uncoupled signal formation

The EPR spectra of the non-native Co(II) and radical species is obtained by the deconvolution procedure that is described in Section 2.3.2, so that the time-course kinetics of these non-native species can be found. However, in order to treat the formation of the non-native species in comparison with the decay of the native Co(II)-substrate radical pair, we need concentrations of each species rather than the amplitudes of the EPR spectra. In spectroscopic methods, the area under the absorption curve (A.U.C.) gives the concentration value for the absorbing species (after the conversion using a concentration standard). Since the EPR spectroscopy produces first-derivative lines of the absorption curve because of the field-modulation and phase-sensitive detection scheme, a double-integration of the EPR spectrum is required to obtain the A.U.C.

Therefore, the double integration of the raw EPR spectrum gives the A.U.C., which can be a direct measure of the concentration of the Co(II)-substrate radical pair if a spin standard is used. In this project, only the comparison of the concentration values of the native and the non-native signal is needed, therefore comparing the A.U.C. was sufficient without the conversion to the concentrations obtained by using a spin standard. An example of the integration procedure is given in Figure 2-10 that shows the $t = 0$ s first-derivative EPR spectrum at the top and the integral of this spectrum at the bottom for the representative temperature of 220 K. The gray highlighted segment of the spectra in Figure 2-10 shows the substrate radical component of the Co(II)-substrate radical lineshape with the overlapping high-field portion of the Co(II) component of the radical pair lineshape at the $g_{\parallel}$ region. The remainder of the spectrum that is shown in black has the Co(II) features. The A.U.C. values for the substrate radical component of the Co(II)-substrate radical lineshape corresponds to the area under the gray-highlighted segment up to the black-dashed line, which represents the Co(II) absorption.
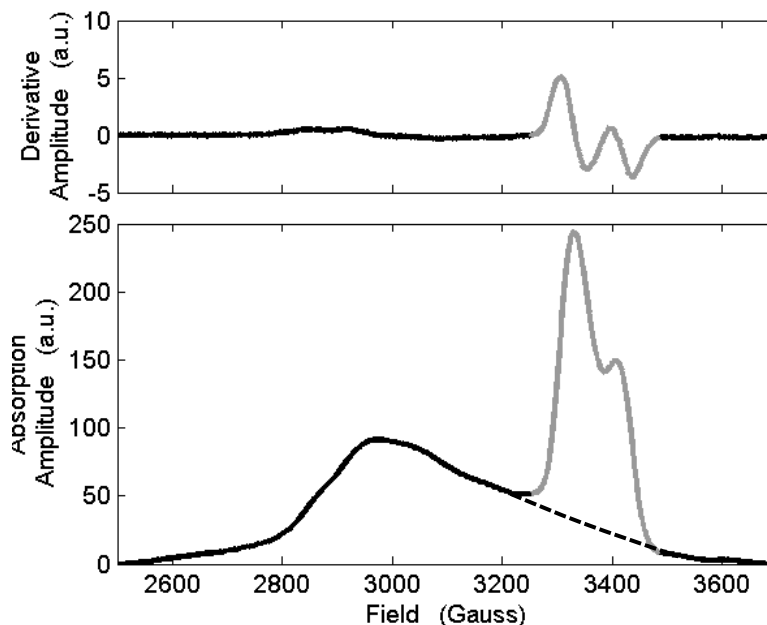
Figure 2-10 The $t = 0$ s first-derivative EPR spectrum of the Co(II)-substrate radical pair at 220 K (Top), and the integral of this signal which represents the EPR absorption after spectrum (bottom). The substrate radical component of the Co(II)-substrate radical lineshape is highlighted with gray lines in the spectra.

The A.U.C. values should give a 1:1 ratio for the Co(II) and the substrate radical for the initial spectrum. In this project, the EPR spectrum of the Co(II)-substrate radical pair is collected by sweeping the field between 2500 – 3700 G. The field span is kept at the smallest possible range that includes the Co(II) peak and the substrate radical component of the Co(II)-substrate radical lineshape, as well as a sufficient baseline from the two ends of the line, and yet yields a minimum sweep time, so that time-resolution of the full-spectrum data acquisition scheme is enhanced. Therefore, the small Co(II) features that normally show up to 3900 G were not present in the data sets. In order to test the accuracy of the double integration procedure by checking if the A.U.C. of the Co(II) and the radical features is 1:1, we made a correction for this early truncation of the signal (18% of the A.U.C. of the Co(II) is lost to the early truncation). A new measurement is done with

a full-field sweep between 2400 – 4100 G, and the ratio of the A.U.C. of the Co(II) features between the field sweep that is used in the decay experiments (2500 – 3700 G) to the full sweep (2400 – 4100 G) is taken as a correction factor for the early truncation. After the correction, the Co(II) features gave a 1:1 ratio with the radical features in the Co(II)-substrate radical pair spectra that is collected between 2500 – 3700 G.
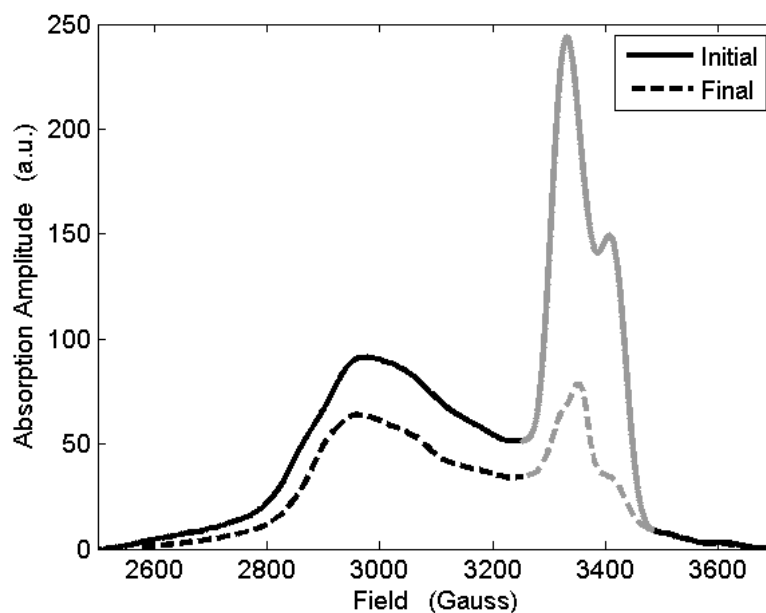
Figure 2-11 Comparison of the EPR absorption spectra of the Co(II)-substrate radical pair that is collected at the beginning of the decay (Initial: solid line spectrum) and the end of the decay (Final: dashed line spectrum) at 220 K. The substrate radical component of the Co(II)-substrate radical lineshape are highlighted with the color gray.

The double-integration procedure was repeated for the first-derivative spectrum of the Co(II)-substrate radical pair that was collected at the end of the decay (Final Spectrum [See the dashed absorption spectrum in Figure 2-11]). If there was no non-native reaction path observed, the 1:1 ratio for the Co(II) and the substrate radical concentrations should been preserved over the

course of the decay, and at the end of the decay. However, in the case of this project where the formation of a new Co(II) signal that is *uncoupled* to the native substrate radical decay is clearly seen, the ratio has changed in the favor of the Co(II) species. The final absorption spectrum has a Co(II) concentration that is higher than the total of the residual substrate radical and uncoupled radical at the $g_{||}$ region (Figure 2-11). The difference between the cobalt concentrations of the initial and final spectrum gives the proportion of the Co(II) that decayed with the substrate radical in the native reaction path. This information can be used to obtain the relative percentages of initial spin concentration that reacts by the non-native and uncoupled reaction paths. According to these calculations, the (26.9 ± 6.3) % of the initial Co(II) spin population undergoes the non-native reaction in this example, for 220 K. The percentage of the uncoupled Co(II) that is formed at each decay temperature relative to the total starting Co(II)-substrate radical pair is given at Table 2.2.

Table 2.2 The percentages of the uncoupled Co(II) that is formed at the end of the decay with respect to the initial Co(II)-substrate radical pair.

T (K)	% Uncoupled Co(II)
220	0.15 ± 0.07
225	0.28 ± 0.03
230	0.26 ± 0.06
235	0.26 ± 0.12
240	0.36 ± 0.05
245	0.30 ± 0.12
250	0.28 ± 0.06

The kinetics of the formation of the uncoupled Co(II) species is found by the subtraction of the Co(II) peak at $g_\perp$ from the low-field baseline in the deconvoluted spectra series of uncoupled reaction (Figure 2-3). These first-derivative EPR amplitudes are then scaled to the relative spin concentration values found by the double-integration method that is described above. After the

scaling, the time-dependent formation of the uncoupled Co(II) relative to the initial total spin concentration is obtained (Figure 2-12). In Figure 2-12, the rise of the uncoupled Co(II) concentration is given. The total initial Co(II) concentration corresponds to the unity in Figure 2-12. From Figure 2-12, one sees that the rate of the uncoupled Co(II) signal rise increases with increasing temperature.
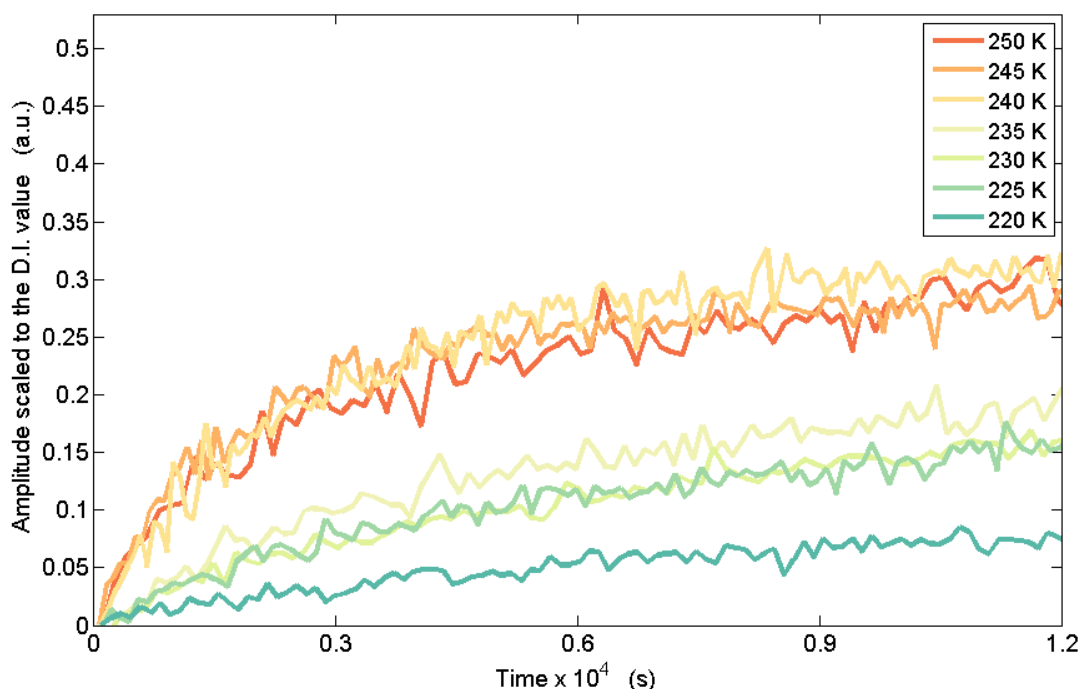
Figure 2-12 Time-dependence of the uncoupled Co(II) formation that is observed during the decay of the Co(II)-substrate radical pair. The raw amplitude values are calculated by the subtraction of the Co(II) peak from the low-field baseline in the deconvoluted uncoupled Co(II) species formation spectra, and then scaled to the area under the absorption curve which is equivalent to the double integral (D.I.) value of the first-derivative EPR spectrum. Therefore, the kinetics of the formation is obtained from the deconvoluted spectra, and the amplitudes are found by the relative percent concentration of the uncoupled Co(II). The colors indicate the rise of the uncoupled Co(II) signal at different temperatures.

The formation of the uncoupled Co(II) is fitted to a double exponential curve to investigate the observed kinetics of this non-native reaction path:

$$A'(t) = (A'_s + A'_f) - (A'_s e^{-k'_{obs,s}t} + A'_f e^{-k'_{obs,f}t})$$

Equation 2-1

where the A' is the A.U.C.-scaled EPR amplitude of the uncoupled Co(II) with observed slow and fast amplitude parameters, A'_s and A'_f, which correspond to with the rates $k'_{obs,s}$ and $k'_{obs,f}$, respectively.
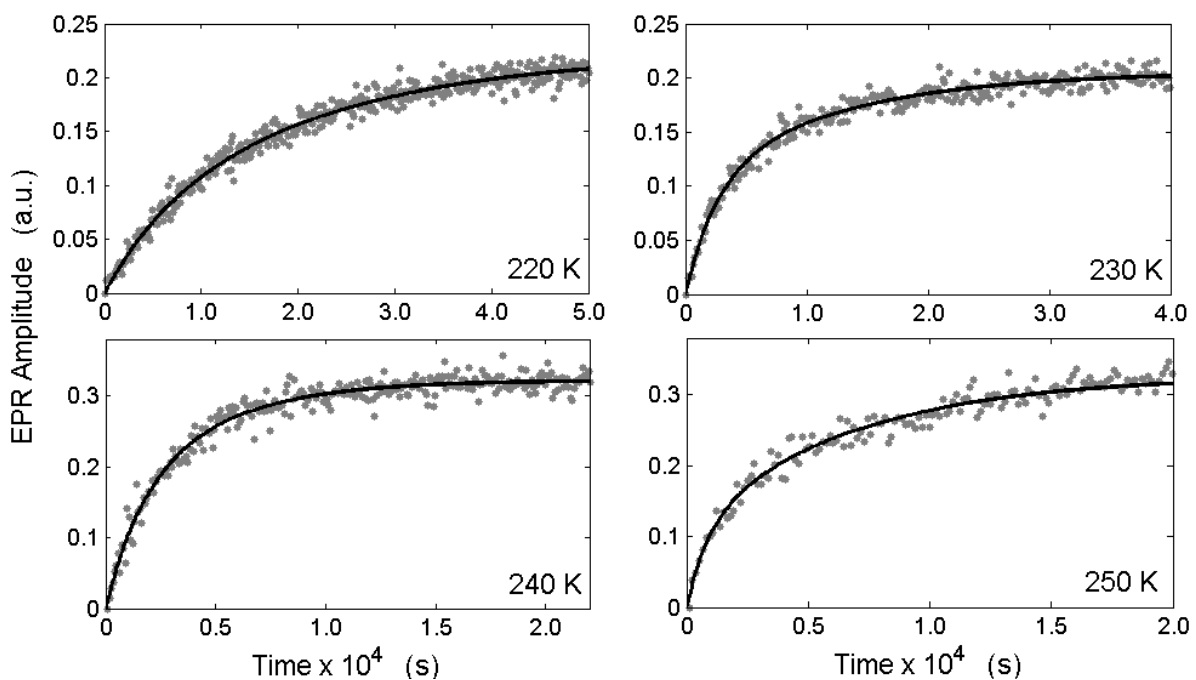
Figure 2-13 The biexponential fitting to the formation of the A.U.C-scaled uncoupled Co(II) EPR amplitudes. The data is shown in grey and the black lines represent the fits.

The fits to the representative data at 220 K, 230 K, 240 K and 250 K are given in Figure 2-13, and the mean values and standard deviations of the fitting parameters the fits of all datasets at 220, 230, 240, and 250 K are given in Table 2.3. Similar to the decay of the Co(II)-substrate radical pair, the formation of the uncoupled Co(II) has two phases. The formation of the uncoupled Co(II) has a lower final concentration than the total initial Co(II) amplitude, hence the signal-to-noise ratio was poor by comparison (Figure 2-13). This yielded the higher standard error for the fit parameters, and lower quality of the fits (Table 2.3)

Table 2.3 The fitting parameters of the biexponential fit to the uncoupled Co(II) formation curves.

T (K)	A'_s	$k'_{obs,s}$ x 10^{-4} (s^{-1})	A'_f	$k'_{obs,f}$ x 10^{-3} (s^{-1})	$R'^{2\dagger}$
220	0.72 ± 0.03	0.19 ± 0.02	0.28 ± 0.03	0.17 ± 0.07	0.9976
225	0.74 ± 0.01	0.34 ± 0.04	0.27 ± 0.01	0.23 ± 0.01	0.9988
230	0.81 ± 0.10	0.85 ± 0.24	0.19 ± 0.10	0.62 ± 0.12	0.9994
235	0.79 ± 0.09	1.14 ± 0.04	0.21 ± 0.09	0.70 ± 0.22	0.9995
240	0.73 ± 0.12	2.61 ± 0.20	0.27 ± 0.12	0.92 ± 0.34	0.9993
245	0.13 ± 0.06	0.52 ± 0.16	0.87 ± 0.06	0.60 ± 0.03	0.9960
250	0.29 ± 0.08	1.15 ± 0.34	0.71 ± 0.08	1.43 ± 0.11	0.9964

† R′ is the Pearson's correlation coefficient for the biexponential-fitting to the uncoupled Co(II) formation curves

2.4   Discussion

2.4.1   Observed kinetics of the Co(II)-substrate radical decay

The time dependency of the CW-EPR and the optical spectroscopic data reveals the observed kinetic parameters of the Co(II)-substrate radical pair decay (see Section 2.3.3). In this section, the temperature dependency of these observed kinetic rates in the form of the Arrhenius plots (ln$k$ vs T^{-1}) will be established.
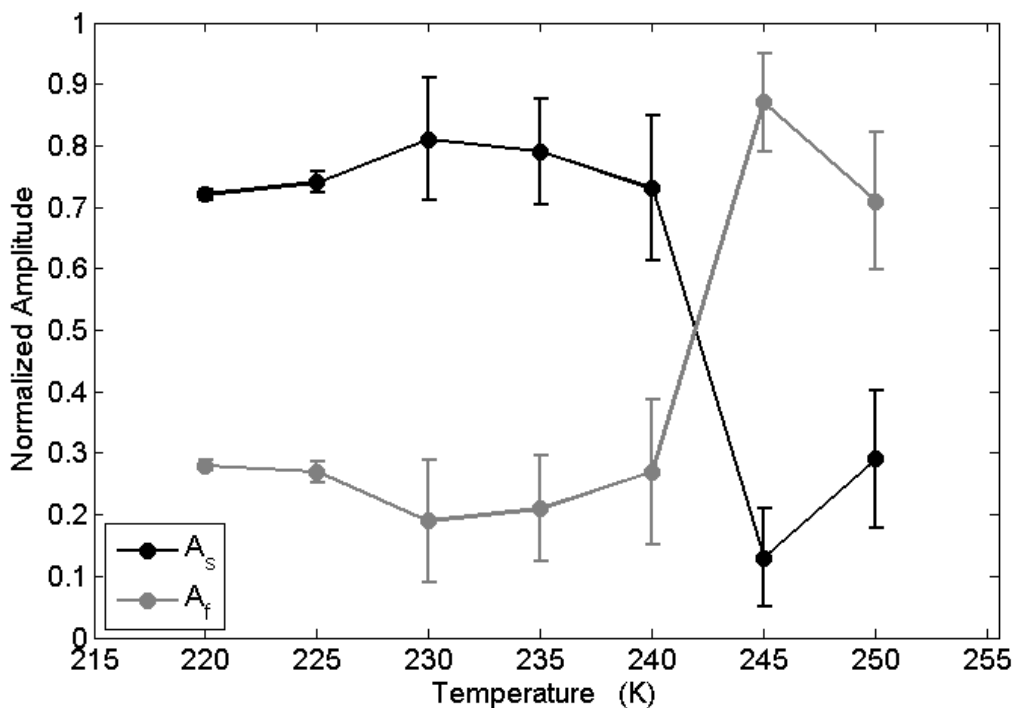
Figure 2-14 The normalized weights for the fast and slow phases of the Co(II)-substrate radical pair decay that is found by the exponential fit parameters.

The relative fast and slow phase amplitudes that are listed in Table 2.1 are plotted with respect to the temperature (Figure 2-14). According to Table 2.1 and Figure 2-14, the $75.9 \pm 4.1\%$ of the Co(II)-substrate radical pair amplitude decays with the slow phase up to 245 K, and $21.1 \pm 1.1\%$ of the Co(II)-substrate radical pair amplitude decays with the fast phase. At the temperatures

above 245 K, the 24.1 $\pm$ 4.1% of the initial amplitude decays with fast phase, whereas the 78.9 $\pm$

1.1% of the initial signal decays with the slow phase. Therefore the dominant phase of the observed

kinetics switches from the slow phase to the fast phase after 240 K.
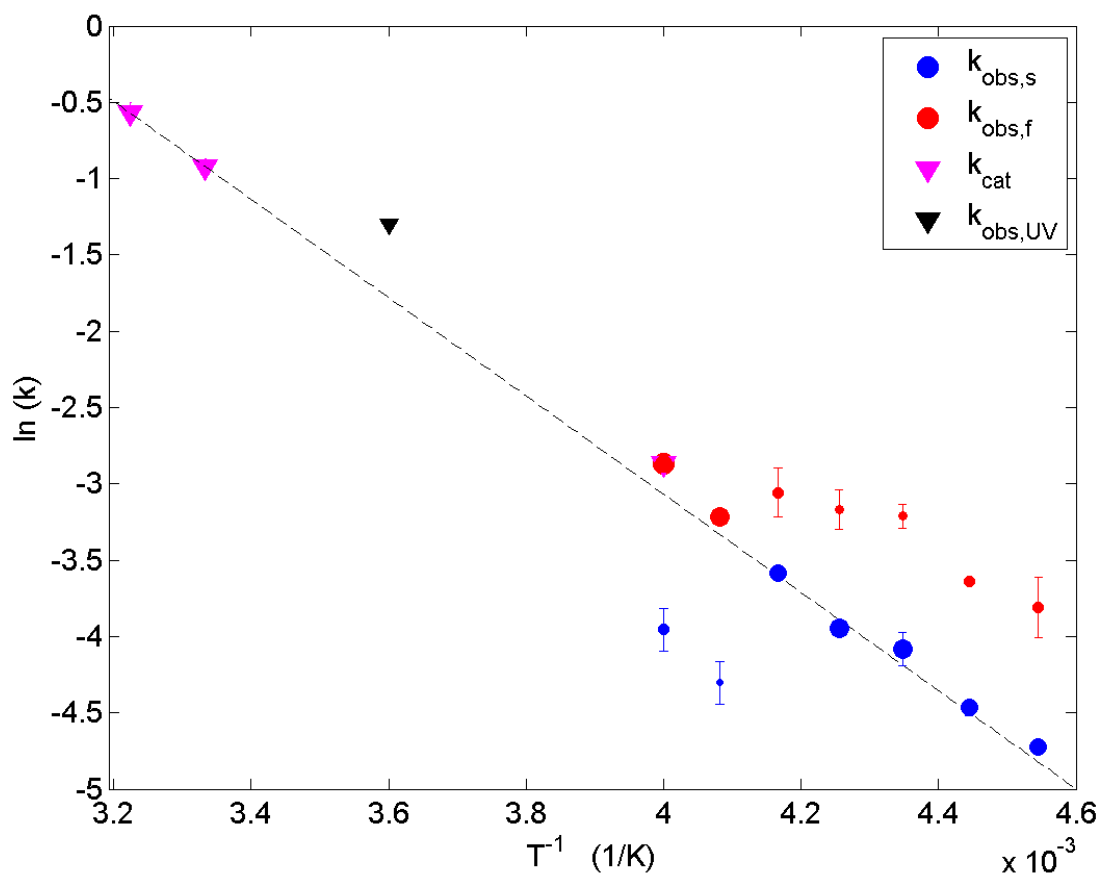
Figure 2-15 The Arrhenius plot for the fast and slow components of the observed Co(II)-substrate radical pair decay kinetics. Blue and red solid circles show the slow ($k_{obs,s}$) and the fast ($k_{obs,f}$) rate constants respectively. The diameters of the circles are obtained from the relative amplitude parameters (A_s and A_f) that are listed on Table 2.1 and shown in Figure 2-14. Therefore, the bigger solid circles indicate that the corresponding rate constants are more dominant than the smaller solid circles. The black solid triangle represents the first-order rate constant of the decay at 278 K ($k_{obs,UV}$) that is found by the time-course UV-visible measurement of the Co(II)-substrate radical pair decay, and solid magenta triangles represent the turnover number (k_{cat}) at 298 K [52], and at 310 K [14]. The overlaid dashed line represent the linear fit to the k_{cat} values at the two most physiological temperature values; 298 K and 310 K.

The Arrhenius plot is shown in Figure 2-15. The amplitude parameters of the kinetic fitting (A_s and A_f) reflected by the sizes of the markers that represent the first-order rate parameters ($k_{obs,s}$ and $k_{obs,f}$). Hence, the temperature-dependent switch in the kinetic amplitudes that is shown in Figure 2-14 becomes visible in the Arrhenius plot also. The transition of the dominant amplitude weights from slow phase to fast phase after 240 K that is shown in Figure 2-14, can also be seen in the Arrhenius plot also with the transition of the dominant phase (shown with larger markers) from slow to the fast at the same temperature. In the same plot, two more types of data points are, (i) $k_{obs,UV}$, the rate constant that is obtained by the time-resolved UV-visible kinetic measurement of the Co(II)-substrate radical decay at 278 K (see 0), and (ii) k_{cat}, the reported turnover rates at 298 K and 310 K [14, 52]. A linear fit is applied to the turnover rate data which matched well with the Co(II)-substrate radical decay data that are collected at the cryogenic temperatures using CW EPR. The linear Arrhenius relation from the physiological temperatures to the low-temperature CW EPR data shows that: (1) Our CW-EPR data corresponds to the native reaction. This unbroken relation suggests that the mechanism of the reaction remains the same at the 220-250 K temperature range. (2) At the low-temperature values, the EAL is reacting in a single step, which we is proposed as the "radical rearrangement" step (Step **3** in Figure 1-5) in the previous studies [31, 67-70]. Thus, the observed rate constants corresponds to the kinetics of this single step. As in (1) above, the kinetics of this single step (which is the central, bond rearrangement step in EAL catalysis) represents the native reaction step. The observed rate constant for Co(II)-substrate radical decay that is found by the UV-visible spectroscopy measurement also fits well to the line, considering that it has conducted under very different conditions; i.e. using liquid sample, and at a higher temperature. As an overall note; the match of

the k_{cat} at 298 K [52], and at 310 K [14] with the dominant observed kinetics indicates that 2-aminopropanol-generated Co(II)-substrate radical pair decay in the low-T aqueous solvent system represents the reactions with the native substrate well at the physiological conditions considerably good. As an additional speculation, the abrupt change in the Arrhenius kinetics and the dominant amplitudes suggest a solvent dynamical effect that influences the core-catalytic reaction.

In this study, the initial Co(II)-substrate radical pair population went through two different reaction paths: the native path which is proposed to be the rearrangement step (Step **3** in Figure 1-5) in the minimal reaction mechanism, and also a non-native path which forms a Co(II) population that is not coupled to the substrate radical. This uncoupled Co(II) could represent a dysfunction that nevertheless represents an event involved in the native reaction, and can serve as a new observable to understand the native reaction.

One way to make speculations about the structural origin of this non-native Co(II) formation in the (S)-2-aminopropanol-generated Co(II)-substrate radical decay is to make comparisons with the same signal in the aminoethanol-generated Co(II)-substrate radical decay. Since the native substrate does not show a significant formation of the non-native Co(II) [68, 69], the stereochemistry of the aminopropanol could be the origin of the non-native Co(II) formation in (S)-2-aminopropanol-generated Co(II)-substrate radical decay. The past literature on the (S)- and (R)-enantiomers of the aminopropanol shows the inversion of the configuration of the (R)-enantiomer before the amino group migration, and the flipping of the (S)-enantiomer before undergoing the HT2 step [44, 81]. These are indicative of the interconversion of the configurations during the reaction cycle. Also, the involvement of the rapid internal rotation of the methyl group during the radical rearrangement step is reported [82]. One of the stereochemical configurations that the aminopropanol undergoes may be locked under the conditions of the low-temperature

experiment. The inability to react through the native pathway on the native reaction time scale, because of steric constraints on substrate radical reorganization prior to amine group migration, may lead to the deleterious reaction of the highly-reactive, carbon-based, primary radical to form non-native products. The Co(II), which is ~11 Å distant from the 2-aminopropanol radical, is a relatively stable s=1/2 species, and does not undergo a similar, destructive reaction.

Although our current understanding of the structural origin of the uncoupled reaction path remains speculative, with the deconvolution of the non-native spectra, we can fully establish the observed kinetic features of this reaction. With our current knowledge, we have found the percentage of the initial Co(II) that went through the non-native path (Table 2.2), and examined the observed kinetics of this non-native reaction path that is summarized in the Figure 2-12, Figure 2-13 and Table 2.3. In the next section, we will insert the observed kinetics data of the native and non-native reaction paths into a detailed, microscopic kinetic model, in order to further elaborate our understanding.

2.4.2   Introduction of the Kinetic Model

The observed decay of the cryotrapped Co(II)-substrate radical pair to the product species consists of at least two individual reactions, (1) the migration of the amino group between the two substrate carbons (C1 and C2), and (2) the second hydrogen transfer step, which forms the product species (Figure 1-5). The rest of the steps are for the formation of the product species that is going to be released and cannot be distinguished using the CW-EPR and optical spectrometer. In order to explain the observed decay phenomenon, the known structural and dynamic information are used to form a quantitative kinetic model, Aas well as logical assumptions. With a kinetic model

that incorporates both the native Co(II)-substrate radical pair decay and this non-native path, we

can reproduce of the kinetics of the parallel reaction that forms the uncoupled species and the

native reaction kinetics.

The microscopic model that is described in Scheme 2-1, is chosen as the minimal model

that accounts for the observed biexponential kinetics of both the native and non-native pathways.

$$S_1^\bullet \xrightarrow{k_1} PH$$

$$k_3 \updownarrow k_4$$

$$S_2^\bullet \xrightarrow{k_2} X$$
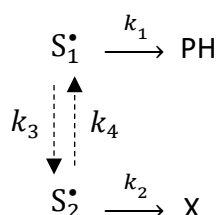
Scheme 2-1 The proposed kinetic model for understanding the structural and dynamical features of the (S)-2-aminopropanol-generated Co(II)-substrate radical decay data. The $S_1^\bullet$ and $S_2^\bullet$ corresponds to the two configurational substates of the initial Co(II)-substrate radical pair population where $S_1^\bullet$ goes through the native reaction path to produce the native product species (PH), and $S_2^\bullet$ goes through the non-native reaction path to produce the uncoupled Co(II) species (X).

Our kinetic model is based on the interconversion of the two initial configurationally

different spin substates, with four postulates:

1. The initial (S)-2-aminopropanol-generated Co(II)-substrate radical pair state (S$^\bullet$) is

   partitioned into two configuration states of unknown initial relative concentrations where

   the equation $S^\bullet = [S_1^\bullet] + [S_2^\bullet]$ holds for all the time.

2. The $S_1^\bullet$ state is the portion of the S$^\bullet$ in which the system has the configuration that is

   favorable for the direct, native reaction, and undergoes the radical rearrangement step with

   a forward reaction rate of k_1.

3. The $S_2^{\bullet}$ is the portion of the $S^{\bullet}$ state that present in a configuration that is in an unfavorable configuration for the direct native reaction, and follows a non-native reaction path that yields accumulation of the uncoupled Co(II) species with a forward reaction rate.

4. The $S_1^{\bullet}$ and $S_2^{\bullet}$ are interconvertible with the reconfiguration rates of k_3 and k_4.

In the proposed minimal mechanism, the Co(II)-substrate radical pair goes through the radical rearrangement step, and the second hydrogen transfer in the minimal reaction mechanism (Figure 1-5). It is evident from the accumulation of the Co(II)-substrate radical pair state in the steady-state turnover of the enzyme, and the substrate $^{14}N/^{15}N$ isotope effect on the steady state kinetic parameters due to the transfer of the amino group in the radical rearrangement step [52, 73] that the radical rearrangement step is the rate limiting step in the steady-state turnover. Since the product radical cannot be distinguished from the Co(II)-substrate radical pair in the EPR spectra, the HT2 step and the rate-limiting rearrangement step constitute a single forward reaction in our model to address the native reaction path , with an effective rate constant, k_1 (Scheme 2-1). The $S_2^{\bullet}$ population goes through first-order reaction step, also, to form the non-native products. Since the intermediate steps (if any) is not known for the non-native path, this would be the simplest reaction that can describe this formation.

In the following section, this model will be used to simulate the data, by solving the set of coupled differential equations that show the time-dependence of the concentrations of each species.

2.5   Simulation of the kinetic model and data-fitting

The observed decay data of the Co(II)-substrate radical pair corresponds to the sum of the two initial spin populations; $S^{\bullet} = [S_1^{\bullet}] + [S_2^{\bullet}]$ that is introduced in the kinetic model. In the model,

the $[S_2^\bullet]$ state represents the fraction of the initial Co(II)-substrate radical pair population that has the configuration to undergo to the non-native reaction path and produce the uncoupled Co(II) species, which is denoted by X in the model. The time-dependence of the formation of the uncoupled Co(II) is calculated by the deconvolution method described in section 2.3.2, that corresponds to the X in the model. The native product that is formed by the reaction of the $S_1^\bullet$ population, PH, is fitted to the data that is calculated by the subtraction of the uncoupled Co(II) formation data from the inverse of the observed data of the Co(II)-substrate radical pair decay.

In this section, the kinetic rate parameters, k_1, k_2, k_3 and k_4 and the initial normalized concentrations of $S_1^\bullet$ and $S_2^\bullet$ in the kinetic model are estimated by fitting the model species, $S^\bullet$, X and PH, to the experimental time-course data of the Co(II)-substrate radical pair decay, uncoupled Co(II) formation, and the formation of the native product species, respectively. The parameter estimation is performed by using the MATLAB Simbiology toolbox routine. The simulation results are presented for a representative data set at each temperature in Figure 2-16. In Figure 2-16, the red, green, and the blue lines represent the simulated time-course behavior of the $S^\bullet$, X and PH, respectively. These three lines are fitted simultaneously to the corresponding experimental data that is shown in black dots in Figure 2-16. The average estimated rates, the Pearson's correlation coefficients for the fittings and initial normalized concentrations of the two spin populations, which give the best-fitting simulations for at least three repetitions at each temperature, are listed in Table 2.4 and Table 2.5.
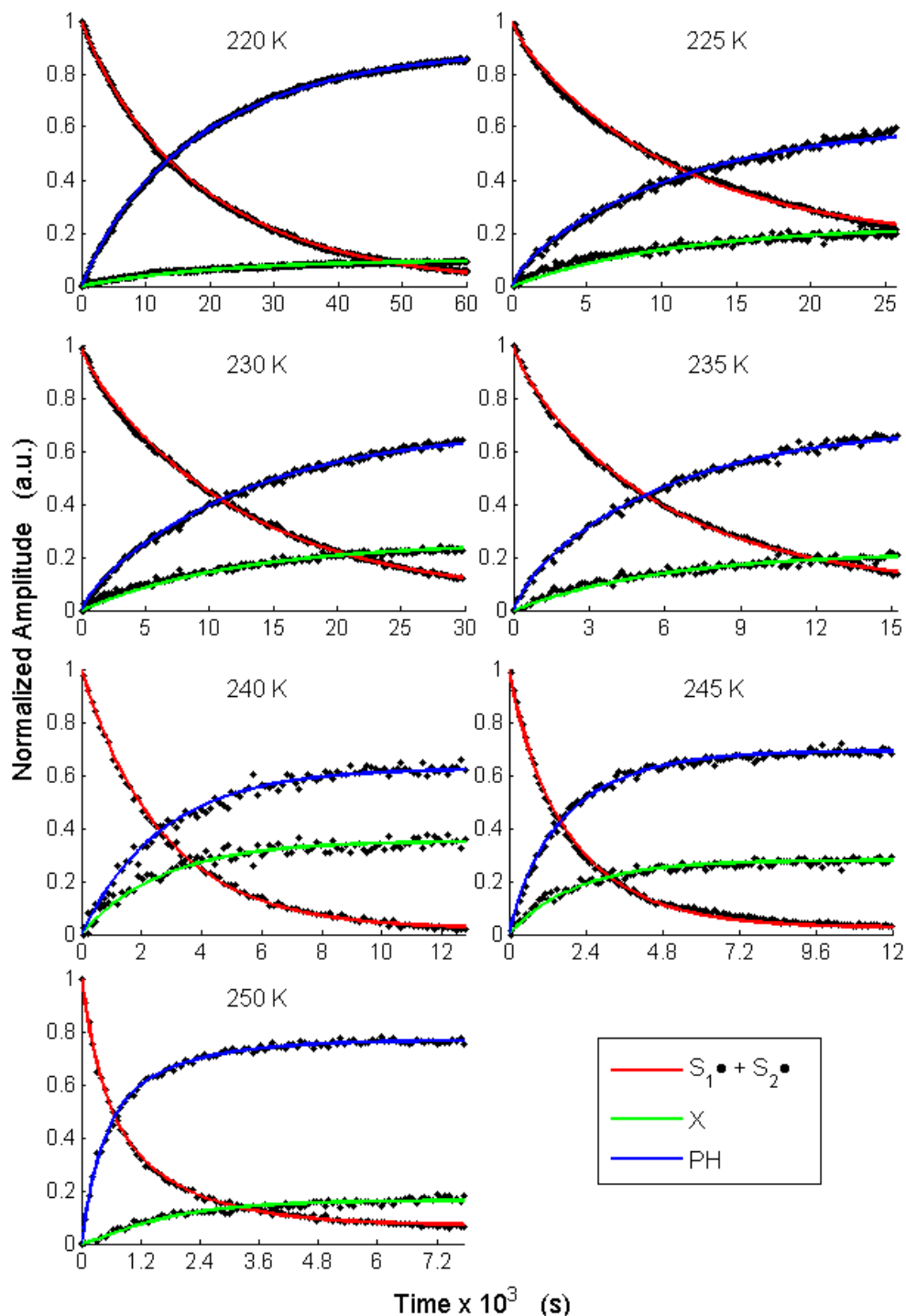
Figure 2-16 Simulation of the substrate radical decay and uncoupled species rise, overlaid on the experimental substrate radical decay and derived uncoupled species rise, for representative data sets over the temperature range of 220-250 K. The red, green and blue curves represent the time-dependence of the simulation species $[S_1^{\bullet}] + [S_2^{\bullet}]$, X and PH which are fitted to the experimental data for the Co(II)-substrate radical pair decay, the formation of the uncoupled Co(II) and the native product species, respectively. The associated experimental data is shown with black dots.

The fitting of the simulation concentration values to the experimental data are satisfactory at almost all of the temperatures (Figure 2-16). Only the sudden initial rise of the uncoupled Co(II) signal is not captured at 225 K and 230 K with the given estimated parameters, however, this rise may be artificial as the EPR amplitude of the uncoupled Co(II) starts off with zero so the initial portion of the uncoupled Co(II) rise has a poor signal-to-noise ratio compared to the Co(II)-substrate radical signal. The estimated rate values and initial spin concentrations for the simulation fitting are averaged for at least three different measurements at each temperature and presented in Table 2.4 and Table 2.5. Also in Table 2.4, the Pearson's coefficient values are averaged for the fitting of the simulation to the experimental data. The estimated parameters, initial concentrations and their corresponding standard deviations show that the simulation fitting to the experimental data produce consistent results.

Table 2.4 The estimated rate parameters for the simulation fitting to the experimental data.

T (K)	k_1 x 10^{-3} (s^{-1})	k_2 x 10^{-4} (s^{-1})	k_3 x 10^{-3} (s^{-1})	k_4 x 10^{-3} (s^{-1})	$R'^{2\dagger}$
220	0.12 ± 0.05	0.18 ± 0.07	0.16 ± 0.09	0.14 ± 0.05	0.9941
225	0.24 ± 0.02	0.35 ± 0.03	0.46 ± 0.17	0.21 ± 0.11	0.9919
230	0.43 ± 0.02	0.41 ± 0.12	0.92 ± 0.59	0.27 ± 0.11	0.9948
235	0.73 ± 0.12	0.50 ± 0.10	0.82 ± 0.29	0.24 ± 0.07	0.9932
240	1.19 ± 0.29	1.55 ± 0.28	1.04 ± 0.71	0.48 ± 0.30	0.9916
245	1.77 ± 0.10	1.74 ± 0.63	0.15 ± 0.02	0.34 ± 0.09	0.9869
250	2.88 ± 0.32	2.29 ± 0.34	0.10 ± 0.09	0.36 ± 0.15	0.9880

† R′ is the average of the Pearson's correlation coefficients for fitting of the simulation data of the [S$_1^\bullet$] + [S$_2^\bullet$],, X and PH to the experimental data.

Table 2.5 The percent initial concentrations of the proposed initial configurations, $S_1^{\bullet}$ and $S_2^{\bullet}$.

T (K)	$[S_1^{\bullet}]$	$[S_2^{\bullet}]$
220	0.60 ± 0.02	0.40 ± 0.02
225	0.48 ± 0.07	0.52 ± 0.07
230	0.44 ± 0.19	0.56 ± 0.19
235	0.31 ± 0.08	0.69 ± 0.08
240	0.25 ± 0.10	0.75 ± 0.10
245	0.30 ± 0.02	0.70 ± 0.02
250	0.54 ± 0.05	0.46 ± 0.05

The temperature dependence of the estimated rate parameters is shown in the form of the Eyring plot, for the two reaction rates, k_1 and k_2 and for the two reconfiguration rates, k_3 and k_4 (Figure 2-17 and Figure 2-18). The k_1, k_2 and k_3 show a linear Eyring relation with the inverse temperature values and the k_3 has an abrupt break from the linear fashion of Eyring plot after 240 K (Figure 2-17, Figure 2-18).
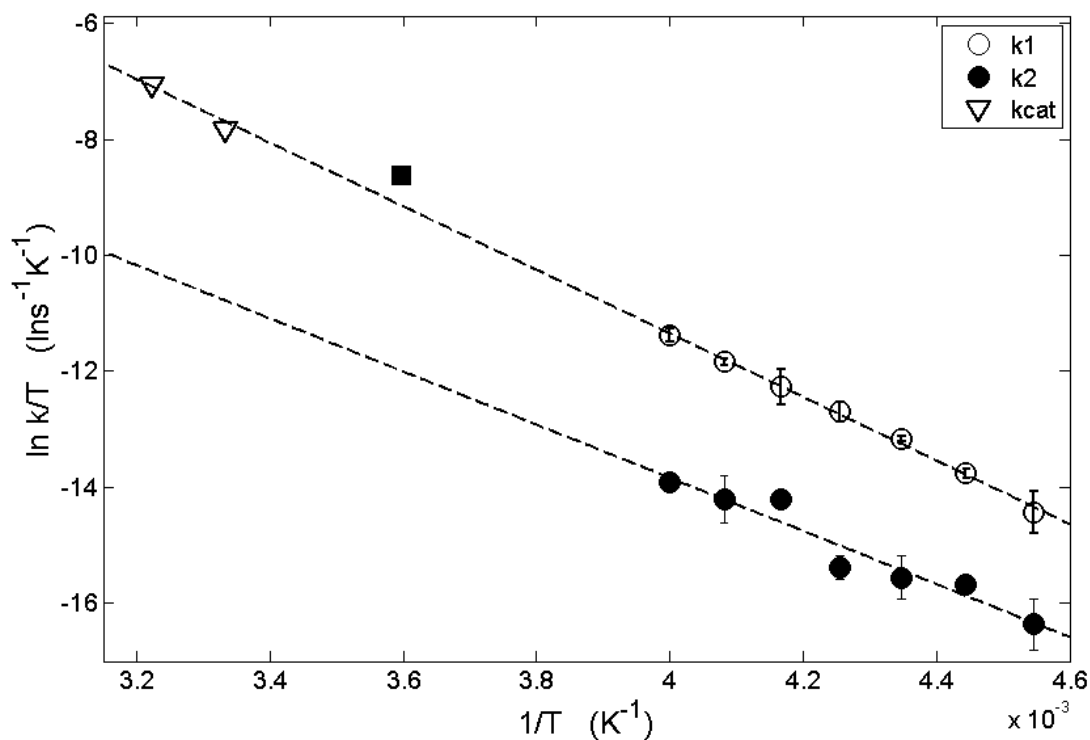
Figure 2-17 Eyring plots for the two simulation rates, k_1 and k_2 (open and full circles, respectively) that are estimated by fitting the associated simulation data to the experimental data of the Co(II)-substrate radical decay. The upper and lower best-fit linear lines are fitted to the k_1 and k_2 data respectively. Black open triangles represent the turnover number (k_{cat}) at 298 K [52], and at 310 K [14]. The solid square represents the rate that is obtained from the UV-vis spectrum measurements. The data are from Table 2.4 and the fit parameters are listed in Table 2.6.

In Figure 2-17, the extrapolation of linear curve that is fitted to k_1 which is assigned to be the forward rate for the native reaction is matching with the reported turnover rates (k_{cat}) for the 2-AmPrOH-generated Co(II)-substrate radical decay at higher, physiological temperatures.
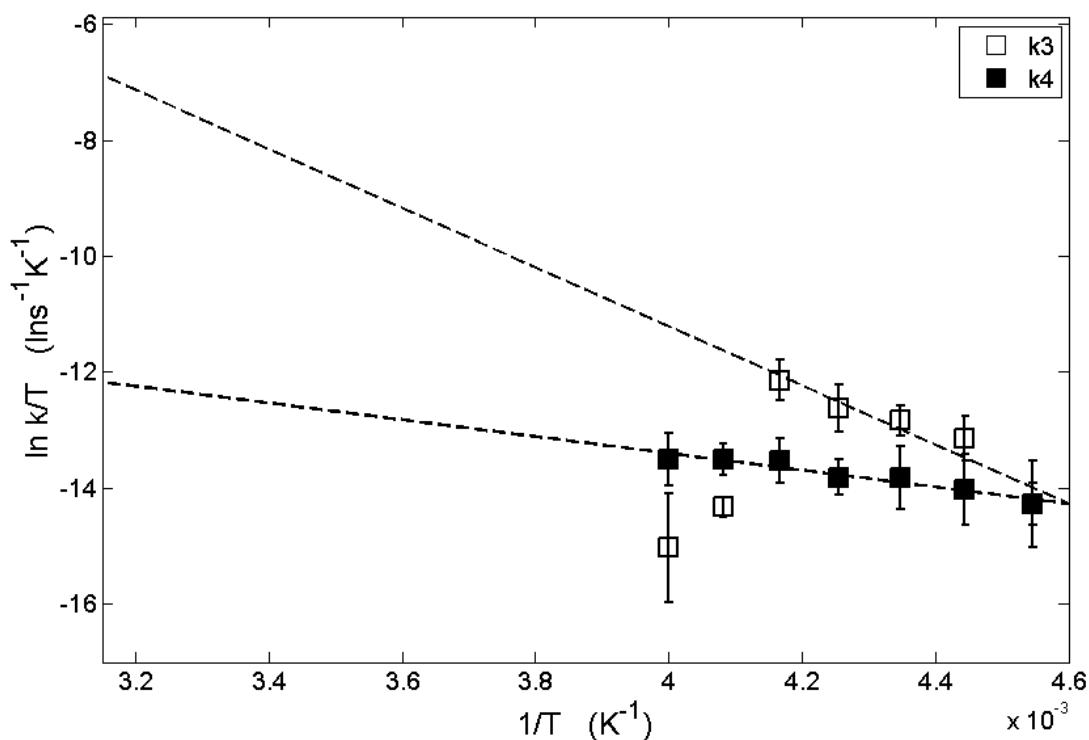
Figure 2-18 Eyring plots for the two simulation rates, k_3 and k_4 (open and full squares, respectively) that are estimated by fitting the associated simulation data to the experimental data of the Co(II)-substrate radical decay. The black dashed lines are the best-fit linear functions. The 245 K and 250 K temperature points are not included in the linear fits because of the abrupt change in the linearity of the data after 240 K for the k_3 rate. The data are from Table 2.4 and the fit parameters are listed in Table 2.6. The transparent areas colored with the shades of gray are to emphasize the three different temperature regimes.

The rate constants of the k_3 and k_4 also give a linear Eyring relation except the k_3 rates at 245 and 250 K. The k_3 rate corresponds to the reconfiguration rate of the $S_1^{\bullet}$ state to the $S_2^{\bullet}$ state, therefore the lower k_3 values indicate that the $S_1^{\bullet}$ state configuration becomes more stable in terms of free energy at 245 K and 250 K. This could be a result of a relaxation that occurs above 240 K in the local region of $S_1^{\bullet}$ configurational space, in a shorter time-scale compared to the reaction kinetics. It is evident from the substrate/product exchange experiment that the active site geometry undergoes a solvent-dependent configurational change that results with the substrate/product

exchange (See section 2.3.1). The protein confirmation could be starting to change around 245 K that yields an increase in the configurational mobility, and may also cause the relaxation of the $S_1^\bullet$ configuration to a lower-energy state.

The dependence of the weights of the initial $S_1^\bullet$ and $S_2^\bullet$ states is shown in Figure 2-19. The weights of the initial $S_1^\bullet$ and $S_2^\bullet$ states have the same amplitude within one standard deviation of ±0.13 at all the temperatures, with the average values of 0.42 and 0.58, respectively.
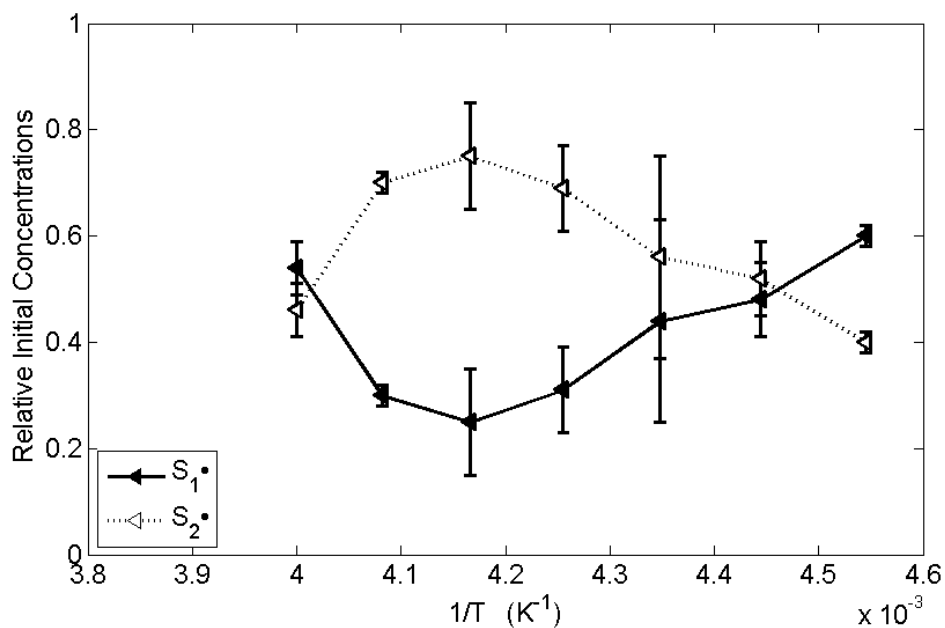
Figure 2-19 The temperature-dependence of the weights of the initial concentrations of the two configurational states, $S\bullet_1$ and $S\bullet_2$ presented in full and open triangles, respectively. Three regions that show characteristic properties is highlighted with the different shades of gray. The data is from Table 2.5.

Table 2.6 Kinetic and thermodynamic parameters determined from Eyring plot linear fittings to the the simulation rates k_1 and k_2, k_3 and k_4.

	$\Delta H^\dagger$ (kcal/mol)	$\Delta S^\dagger$ (cal mol^{-1} K^{-1})	$\Delta G^\dagger{}_{240}$ (kcal/mol)	R^{2a}
k_1	10.9 (±0.7)	-26.2 (±3.0)	17.2 (±0.02)	0.9969
k_2	9.1 (±2.9)	-38.3 (±12.1)	18.3 (±0.1)	0.9309
k_3^b	10.1 (±5.8)	-28.9 (±25.4)	17.1 (±0.3)	0.9104
k_4^c	2.9 (±0.9)	-62.3 (±4.0)	17.8 (±0.02)	0.9263
K_{43}	-7.3 (±5.9)	-33 (±26)	0.8 (±0.3)	

[a]R is the Pearson's correlation coefficient
[b,c]The 245 K and 250 K temperature points are excluded from the linear fit because of the abrupt change in the linear behavior.

The kinetic and thermodynamic parameters are calculated by the linear Eyring fit parameters and shown in Table 2.6. This energetic reading from the Eyring plots can be summarized on a 2-D free energy curve (FEC) depiction (Figure 2-20). In Figure 2-20, the horizontal dimension represents the activation entropic features of the states ($\Delta\Delta S^\ddagger$), and the vertical dimension represents the activation enthalpy difference between the states ($\Delta H^\ddagger$). As seen in Table 2.6, the $\Delta H^\ddagger$ parameter is smallest (2.9 kcal/mol) for the $S_2^\bullet$-state which is, by the model definition, connected to the $S_1^\bullet$-state through the same barrier. Also, the $S_2^\bullet$-state, from the k_2 and k_4 entropy parameters, possesses a relatively higher entropic configurational space than the $S_1^\bullet$-state. The free energy difference between the two states is small (Table 2.6), which is consistent with the observation that the initial $S_1^\bullet$- and $S_2^\bullet$-state concentrations are the same. Therefore, with the $S_2^\bullet$-state being higher in entropy and enthalpy than the $S_1^\bullet$-state, the initial Co(II)-substrate radical pair state partitions into two sequential states according to our model. The HT1 step

deposits the $S_2^{\bullet}$-state which represents the many different configurations of the substrate and protein, and the protein guides the substrate to the configuration that is favorable for the rearrangement reaction, which is corresponding to the $S_1^{\bullet}$-state. However, as the substrate and the protein configurations in $S_2^{\bullet}$-state exceed their viable lifetimes, a destructive reaction occurs to form the non-native species. This interpretation is supported by $S_1^{\bullet}$- and $S_2^{\bullet}$-states being indistinguishable by the EPR spectroscopy and the formation of the barrier between the two in a non-Arrhenius way between 250 K and 277 K.
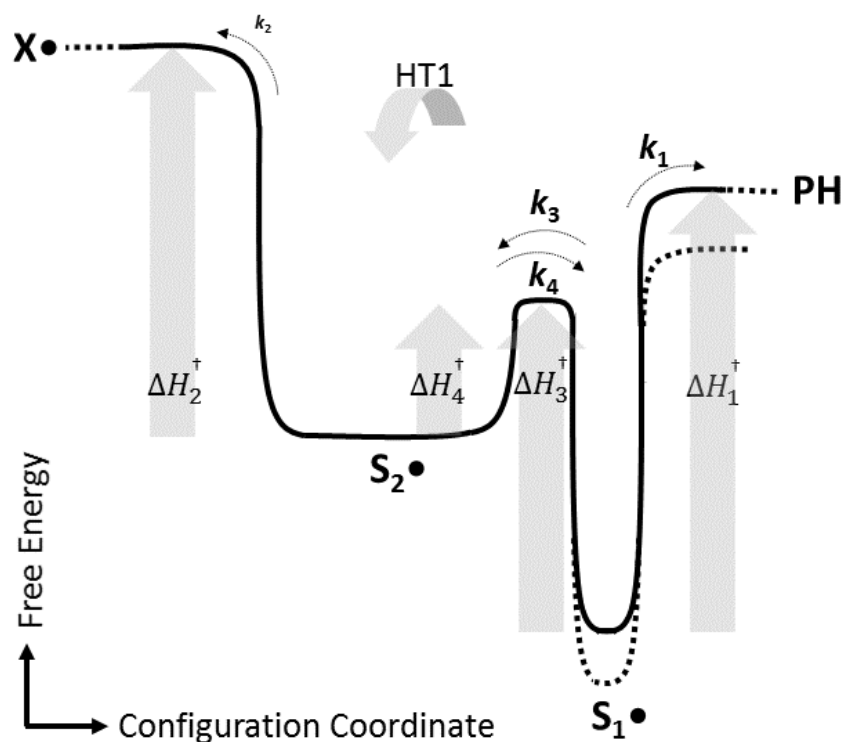
Figure 2-20 The schematic 2-D FEC representation of the minimal kinetic model. The blue arrow is attributed to the relaxation that the $S\bullet_1$ state undergoes at 245 and 250 K, and the dashed curve corresponds to the $S\bullet_1$ state energy profile at 245 and 250 K.

The native and non-native pathways respond differently to the change in T, which is evident from the T-dependence behavior of k_3 compared to the k_4 (Figure 2-18). This is shown in the FEC representation by the dashed lines for the $S_1^{\bullet}$-state to PH barrier region, as the enthalpy and free energy of the $S_1^{\bullet}$-state decreases at $T > 240$ K. In other words, the linear Arrhenius relation deviates from the linearity abruptly within a temperature range of 5 K in favor of the native reaction. The abrupt kink in the Arrhenius relation is an indicative of a change in the kinetics because the intrinsic properties of the chemical reaction, itself do not create an abrupt effect on the Arrhenius profile. This identifies the presence of specific configurations and configurational fluctuations that guide the native pathway, relative to the non-native pathway.

2.6   Conclusions

One of the main conclusions is, this study achieved its primary goal: Investigating the kinetics of the Co(II)-substrate radical decay in EAL at higher temperatures than the previous studies focusing on the same step in the EAL catalytic action [67-69]. In the previous CW-EPR studies, because the observed kinetics is fast compared to the instrument dead-time at higher temperatures, the highest temperature that the kinetic experiments were held was 230 K [68, 69]. In this study, we used the slower substrate analogue, 2-aminopropanol, to be able to time-resolve the enzyme kinetics at the temperatures as high as 250-260 K. The kinetics of the 2-aminopropanol-generated Co(II)-substrate radical pair decay at 220-250 K is manifested at the single-step resolution with the observed kinetics corresponding to the kinetics of the radical rearrangement step in the EAL minimal mechanism (Step **3** in Figure 1-5). Moreover, the kinetics of this single step is found to be an admissible representative of the native system when observed under the physiological conditions, as well as the previous low-T CW-EPR studies. Our UV-

visible spectroscopic measurement also supported this result and showed that we obtained solid kinetics information considering that UV-visible spectroscopy requires very different solvent and experimental conditions compared to the CW-EPR.

The kinetic information obtained by the CW-EPR and UV-vis spectroscopy is studied at two levels:

(I)   Observed kinetics: The time-dependence of the EPR amplitudes at $220 - 250$ K show a clear bi-phasic behavior with amplitudes of 78% and 22% ($\pm 5\%$) of the total spin population. The most striking feature of this observed behavior is the transition of the dominant phase from slow to the fast phase at ~240 K. This transition could be attributed to a solvent dynamical transition that enhances the enzyme kinetics. Another important finding is the emergence of another reaction path that is uncoupled to the native reaction. This reaction path is deconvoluted from the observed reaction so that we are able to analyze it separately, which in turn provide a space for structural speculations for the native kinetics, and enabled us to propose a minimal kinetic model.

(II)   The minimal kinetic model: The native radical rearrangement step is resolved into two sub-steps, and two sequential states are identified on the native radical rearrangement pathway: $S_2^{\bullet}$ state, relatively high entropy/enthalpy state, in a configuration corresponding to the terminal radical pair separation state and $S_1^{\bullet}$ state that is "enabled" and reconfigured for the radical rearrangement step. Reconfiguration proposed to be primarily in the protein. Also, an unprecedented, non-native pathway of deleterious radical reaction is identified from $S_2^{\bullet}$ state that

can be used to assess whether the influence of an identified protein dynamic effect ("kink" in the Arrhenius T-dependence) is "generic," or, whether the dynamical effect is specific to native pathway: Different regions of the FEC have different T-dependencies. This selective change in the FEC along configurations that conduct the native, forward reaction, identifies the presence of specific protein configurations and configurational fluctuations that guide the native pathway in EAL.

Overall, time-resolved kinetics investigation of the Co(II)-substrate radical pair in EAL using CW-EPR showed that the observed kinetics corresponds to the native radical rearrangement reaction, only with the a portion of the initial Co(II)-substrate radical pair remains in a different protein-active site configuration which yields the observation of a non-native reaction path in addition to the native reaction. The kinetic modelling of the observed reactions showed the partition of the radical rearrangement step into two sub-states and presented evidence for possible protein-driven configurational fluctuations that is enabling the radical rearrangement reaction in EAL.

Chapter 3

Spin Probe Investigation of the EAL Mesodomain Structures in Frozen Aqueous Solution in the Presence of Aminopropanol

3.1 Introduction

Many spectroscopic studies that aim to understand the functional and physical properties of proteins provide a limited understanding of the physical picture, because they treat the protein as isolated species from its surroundings. In reality, protein structure exhibits fluctuations around local minima as a result of the thermal energy, and protein conformational substates are hierarchically organized, as described by the energy landscape [83]. In this dynamical picture, understanding the dynamical properties of the solvent around the protein is a key to understand the internal protein motions, because of the role of the solvent in coupling thermal motions in the medium outside the protein with motions in the protein interior, including the active site [84, 85]. Since the water molecules that surround the protein, i.e. the "hydration shell", do not solidify at the same temperature as the bulk aqueous solvent, the dynamical properties of the water, and hence the protein motion associated with it, could be studied in a very broad temperature range that goes far below the freezing point of the bulk water [86]. In frozen aqueous solutions, solutes and water form a mesodomain phase at the ice crystallite boundaries [77]. For the past few decades, some sophisticated experimental techniques such as high-resolution X-ray structure analyses [87, 88], the Mössbauer effect with synchrotron radiation [89, 90], inelastic neutron scattering [91, 92] and dielectric spectroscopy [93, 94] have been used in studies that investigate the dynamics of the solvent, the coupling of solvent and protein dynamics, and the effect on protein function.

The past literature on different proteins and experimental conditions indicates a dynamical transition that the protein in the frozen aqueous solution undergoes, which is referred to as the protein "glass" transition. This protein "glass" transition reportedly occurs over a range of 180 – 200 K in hydrated protein powders, and in the absence of a bulk aqueous solvent [91, 95, 96]. With decreasing temperature through the transition, the internal atomic motions decrease in amplitudes

and increase in the time-scales of the fluctuations. The nature and the source of this transition which is common for different proteins is yet to be understood. The studies that focused on the solvent as the origin of the dynamical transition suggest that the hydrated proteins exhibit large-scale collective motions which are referred to as α-fluctuations, that are characterized by a relatively high activation enthalpy ($\Delta H^{\ddagger}$) [86], and also small-scaled displacements that are known as β-fluctuations, that are characterized by a relatively high activation entropy ($\Delta S^{\ddagger}$) [86, 97]. The change in the α-relaxation is suggested to be the cause of the protein-glass transition, as the α-relaxation becomes slower than the β-relaxation below approximately 200 K, equal with β-relaxation around 200K, and faster than β-relaxation above 200 K [92].

One of the experimental techniques for the protein-dynamical studies is EPR spectroscopy which is used to investigate with spin probes, such as TEMPOL. The solvent and shell motions are addressed directly, not the protein-solvent coupling, by the observation of the mobility of the spin-probes that are present in the hydration shell and the bulk water, and also spin-labels that are attached to the protein structures [98, 99]. In this study, the dynamics of the spin probe, TEMPOL in the frozen aqueous solution of EAL and aminopropanol will be investigated by using EPR spectroscopy over a temperature range of 160 – 265 K. The tumbling of the free spin probe (TEMPOL) that resides in the mesodomain structures in the EAL+water mixture shows that, with increasing temperature, the mesodomain undergoes a change in fluidity that leads to detectable tumbling motion of the TEMPOL at 235 K [77]. It is also proposed that, during the catalysis of the decay of the Co(II)-substrate radical pair, the free energy landscape undergoes a transition which is indicative that the glass-like transition temperature (T_g') is reached [76, 77].The observed kinetics of the aminopropanol-generated Co(II)-substrate radical decay also undergoes a transition in the observed kinetics around the same temperature (see section 2.4.1). The synchronicity of the

two transitions may indicate the effect of the solvent dynamics on the kinetics of the enzyme. In this study, the transition will be determined in the presence of 2-aminopropanol, in order to cover the mesodomain dynamics of the exact same system that is kinetically investigated in Chapter 2.

3.2   Materials and Methods

Sample Preparation

The TEMPOL (4-Hydroxy-TEMPO, Sigma-Aldrich, St. Louis, MO) and the (S)-2-amino-1-propanol were purchased from commercial suppliers (Sigma-Aldrich) and used as received. The EAL is prepared according to the descriptions presented in section 2.2.1. The EAL is present at 120 μM and the aminopropanol is added to 10 mM in the 10 mM potassium phosphate buffer (pH 7.5). The TEMPOL stock solution is dissolved at 10 mM with DMSO [1% (v/v)] is added to 0.2 mM and the sample is transferred to a 4 mm O.D. EPR tube to be frozen in the liquid nitrogen – isopentane temperature bath at $T \approx 150$ K, and stored in liquid nitrogen.

CW-EPR Measurements

The CW-EPR data is collected on a Bruker E500 EPR spectrometer with a Bruker ER4123 SHQE X-band cavity resonator. The temperature control is maintained by a N_2 gas flow unit (which is controlled by a ball flow indicator; King Instrument Co.) from a 250 LN_2 storage dewar through a coil which is put in a liquid nitrogen temperature bath. The temperature is raised from 160 K to 265 K in 5 K increments, and after the 5 min temperature stabilization, the EPR spectra are collected with multiple scans at each temperature point. The EPR experimental conditions are as follows: microwave frequency, 9.449397 GHz; microwave power, 20 dB; magnetic field modulation, 1.0 mT; modulation frequency, 100 kHz.

The experimental CW-EPR spectra were simulated using EasySpin, which is a MATLAB toolbox [100]. Free (random) tumbling of the TEMPOL was assumed.

3.3   Results

3.3.1   EPR Spectroscopy of TEMPOL

Before presenting the results, the characteristics of the X-band EPR signal of the TEMPOL is introduced in this section. The spin probe TEMPOL has a nitroxide-based unpaired electron ($S = 1/2$) which produces an EPR lineshape that is based on the hyperfine interaction of this unpaired electron with the ^{14}N nucleus ($I = 1$) (Figure 3-1). The hyperfine (HF) splitting of the three energy levels that is associated with the quantum numbers m_{l} and the anisotropic hyperfine (AHF) splitting that is observed in the powder samples are shown in the energy level diagram in Figure 3-1. The theory behind the spin probe EPR lineshape is also introduced in section 1.2.2.
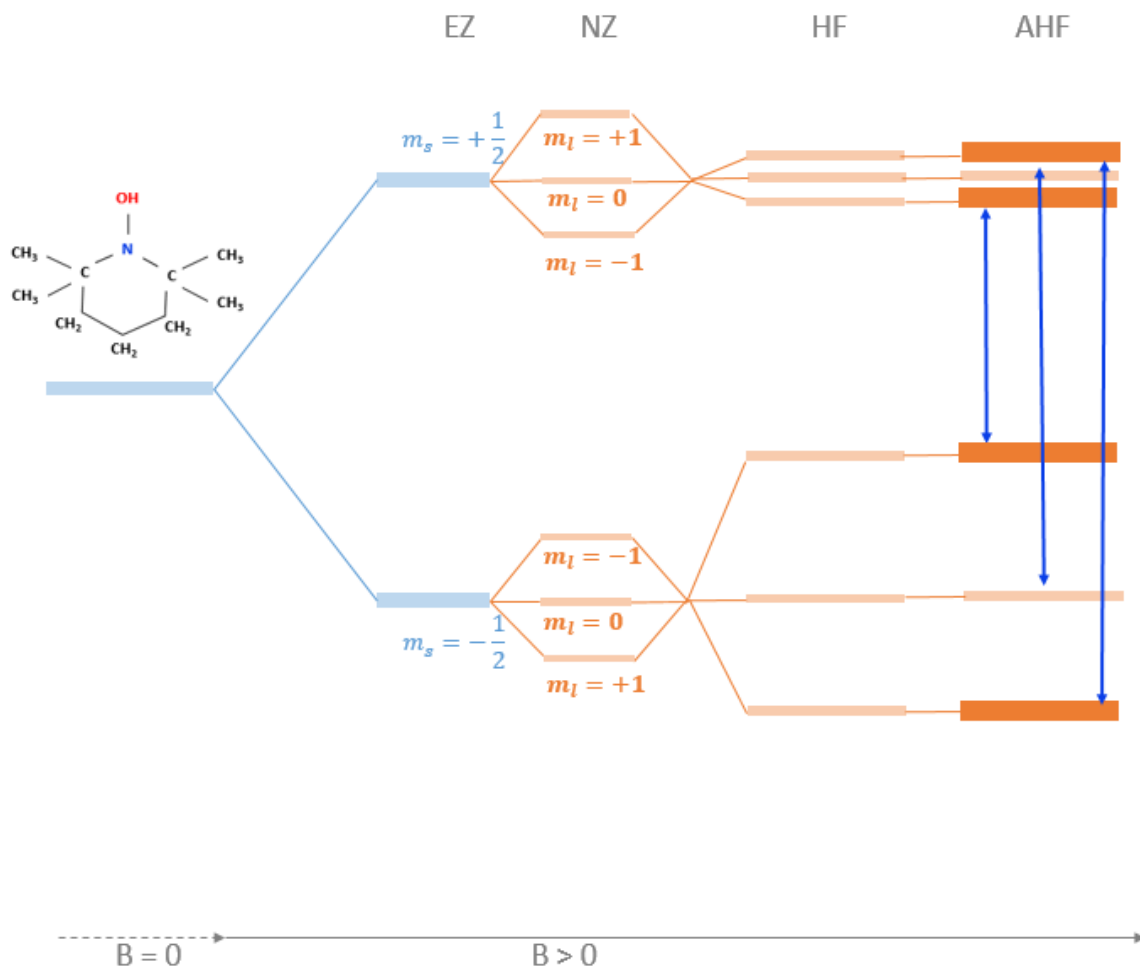
Figure 3-1 The energy level diagram of the HF splitting of TEMPOL is shown. The structure of TEMPOL is on the left. The transitions that are as a result of the AHF are shown with blue arrows.

EPR can detect the tumbling motion of TEMPOL with rotational correlation times that are between 10^{-10} and 10^{-7} s. The EPR lineshape stores the information about the TEMPOL tumbling that occurs in the sample. When TEMPOL is freely tumbling in a liquid solvent, the anisotropy of the $\hat{g}$ and $\hat{A}$ diminishes as the off-diagonal elements are reduced to small values and averaged out. In this study we pass through the entire range of rigid to rapid tumbling with increasing temperature, since the temperature rise yields the mesodomain melting which creates a

liquid-like environment for the residing TEMPOL. The diagonal terms for $\hat{g}$ and $\hat{A}$ for TEMPOL are estimated by an EasySpin rigid-limit simulation and found to be $g_{xx} = 2.0120, g_{yy} = 2.0130, g_{zz} = 2.0073$ and $A_{xx} = 20.9\,G, A_{yy} = 19.699\,G, A_{zz} = 103.2\,G$. For TEMPOL in solution (i.e. at high temperatures in this study) the broadening of the EPR peaks shows a decreased effect of the $\hat{g}$- and $\hat{A}$-anisotropy. However, the powder samples preserve the $\hat{g}$- and $\hat{A}$-anisotropy which results from both the Gaussian and inhomogeneous broadening of the EPR lineshape. In this study, this rigid-limit corresponds to the low temperatures at which the solvent is frozen. In this study, the temperatures 180-220 K in pure water, towards rigid limit, the outer linewidth of the EPR lineshape is equal to the $2A_{zz}$ value, whereas, at the higher temperatures, as TEMPOL becomes closer to the limit of rapid tumbling, the linewidth becomes equal to the orientation-independent isotropic hyperfine coupling constant ($2A_{iso}$). It is also evident from previous studies, that the addition of the sucrose increases the temperature where the transition from rigid-limit to the free tumbling occurs [77, 80]. In this study, since the goal is to understand the dynamics of the Co(II)-substrate radical decay pair (Chapter 2), the TEMPOL samples were prepared to represent the conditions of Chapter 2, hence no sucrose is added to the solution. The EPR lineshape of TEMPOL is simulated by introducing the $\hat{g}$ and $\hat{A}$ diagonal elements (also A_{iso} for the high-temperatures) and MW frequency value of the specific experiments as known parameters, and the correlation time (τ_c) and the linewidth (*lw*) as the unknown parameters to be estimated. Here, τ_c is associated with the rapidity of TEMPOL tumbling Brownian motion, and *lw* is a measure of the convolutional (Gaussian or Lorentzian) broadening of the EPR line. With these parameters, that are varied and optimized in the simulations, the mobility of TEMPOL and its dependence on temperature will be quantified for the presence of EAL and AmPrOH.

In the following section, the EPR spectra of TEMPOL that are recorded at the temperatures between 195 K and 265 K are shown overlaid with the best-fit EasySpin simulations that are run by using the Chili function [100]. The Chili function of the EasySpin toolbox computes the EPR spectra in the slow-motional regime where the random TEMPOL tumbling motion occurs.

3.3.2   The EasySpin Simulations of the EPR spectra of TEMPOL

With the EasySpin simulation toolbox, an EPR spectrum can be simulated by using various variables, some are to be estimated within the given range and initial guesses, and some are to be introduced as known parameters. In this study, the $\hat{g}$ and $\hat{A}$ diagonal elements are introduced as known parameters, and fixed to the values that were found by the previous rigid-limit simulations. Therefore, only the parameters that are associated with the TEMPOL molecular motions; τ_c and *lw*, are varied for the spectral fitting. The fitting is achieved by using two models: (i) assuming the TEMPOL mobility can be defined with one component, and (ii) assuming the TEMPOL molecular motion has two different components with different τ_c and *lw* values.

The 1-Component Simulations of the EPR spectra

In this set of results, the EPR spectra are simulated by assuming that TEMPOL mobility is modeled by a 1-component spin system with uniform τ_c and *lw* values that are specific to each temperature (Figure 3-2). In Figure 3-2, the simulated spectra are shown overlaid with the experimental spectra at 195-265 K. The low temperatures correspond to the rigid regime, where the spin probe is tumbling more slowly than the lower limit of the X-band EPR sensitivity to the motion ($< 10^7 \text{ s}^{-1}$). Even at these low temperatures, for the sake of consistency with the high

temperature data, the "Chili" function is used. The fit parameters that are obtained from 1-component EasySpin simulation fitting are listed in Table 3.1.

Figure 3-2 CW-EPR spectra (black curves) of TEMPOL spin probe in the aqueous solution of EAL and 2-AmPrOH at 195 – 265 K, overlaid with the EasySpin 1-component simulations (red curves). The light gray lines on 195 K plots indicate the $2A_{zz}$ reading from the EPR curve. The same gray lines are also shown on 220 K plot, together with the black lines that indicate the $2A_{zz}$ reading at 220 K, for comparison. The $2A_{iso}$ reading also marked for 265 K on the respective plot. The fit parameters are listed in Table 3.1.

The arrows on the 195, 220 and 265 K EPR spectral fitting plots in Figure 3-2 indicate the outer line width which corresponds to the *z*-component of the anisotropic hyperfine tensor at the rigid limit. The outer line width value at 195 K plot is shown with light gray lines, and with black lines at 220 K. On the 220 K plot, the 195 K the outer line width values (light gray) are also shown for visually inspecting the decrease in the outer line width that starts at 220 K. For quantitative inspection, at 195 K, the outer line width is 148 G (414.3 MHz) and this value remains approximately same up to 215 K; whereas, at 220 K it decreases to 140 G (391.9 MHz). This decrease indicate the solvent undergoes a dynamical transition that allows TEMPOL to become more mobile. Starting from 220 K and above, the mesodomain transitions from a rigid state to a detectably dynamical state that allows the free rotation and thermal motions of the spin probe. On the 265 K plot in Figure 3-2, the outer line width value is shown where the spin probe is closer to the free tumbling with a time scale of $\sim 10^{-8}$ s that is found by the inverse of the outer line width.

Table 3.1 The parameters that are obtained from the 1-component EasySpin simulation fitting to the EPR data. The simulation fits are shown in Figure 3-2.

T (K)	$\log(\tau_c)$	*lw*	RMSD
195	-4.96	0.87	0.024
200	-5.09	0.82	0.021
205	-5.48	0.81	0.019
210	-6.44	0.79	0.018
215	-7.06	0.76	0.017
220	-7.54	0.72	0.017
225	-7.87	0.66	0.026
230	-8.18	0.55	0.026
235	-8.49	0.32	0.022
240	-8.48	0.16	0.020
245	-8.88	0.22	0.020
250	-9.20	0.20	0.010
255	-9.64	0.20	0.011
260	-10.02	0.25	0.011
265	-9.59	0.22	0.011

The dynamical transition that the visual inspection of the simulated EPR spectra indicates is supported quantitatively by the estimated simulation parameters. The $\log(\tau_c)$ values show an increase in the TEMPOL tumbling. At 195 K, the probe is at the rigid limit with a $\log(\tau_c)$ value of -4.96. This value changes as the temperature increases, and at 220 K reaches to -7.54 which indicates the TEMPOL tumbling.

The 2-Component Simulations of the EPR spectra

The 1-component simulated spectra captured the dominant features in the CW-EPR spectra of TEMPOL in the presence of 2-AmPrOH and EAL. This dominant features correspond to the slower component of the TEMPOL tumbling, and as the temperature increases, the faster component of the TEMPOL tumbling becomes dominant. The 1-component simulations seem to be failing to fit all the spectral features that is present. In order to investigate the contribution of another component of motion, a 2-component EasySpin fitting procedure is implemented, and the results are shown in Figure 3-3.
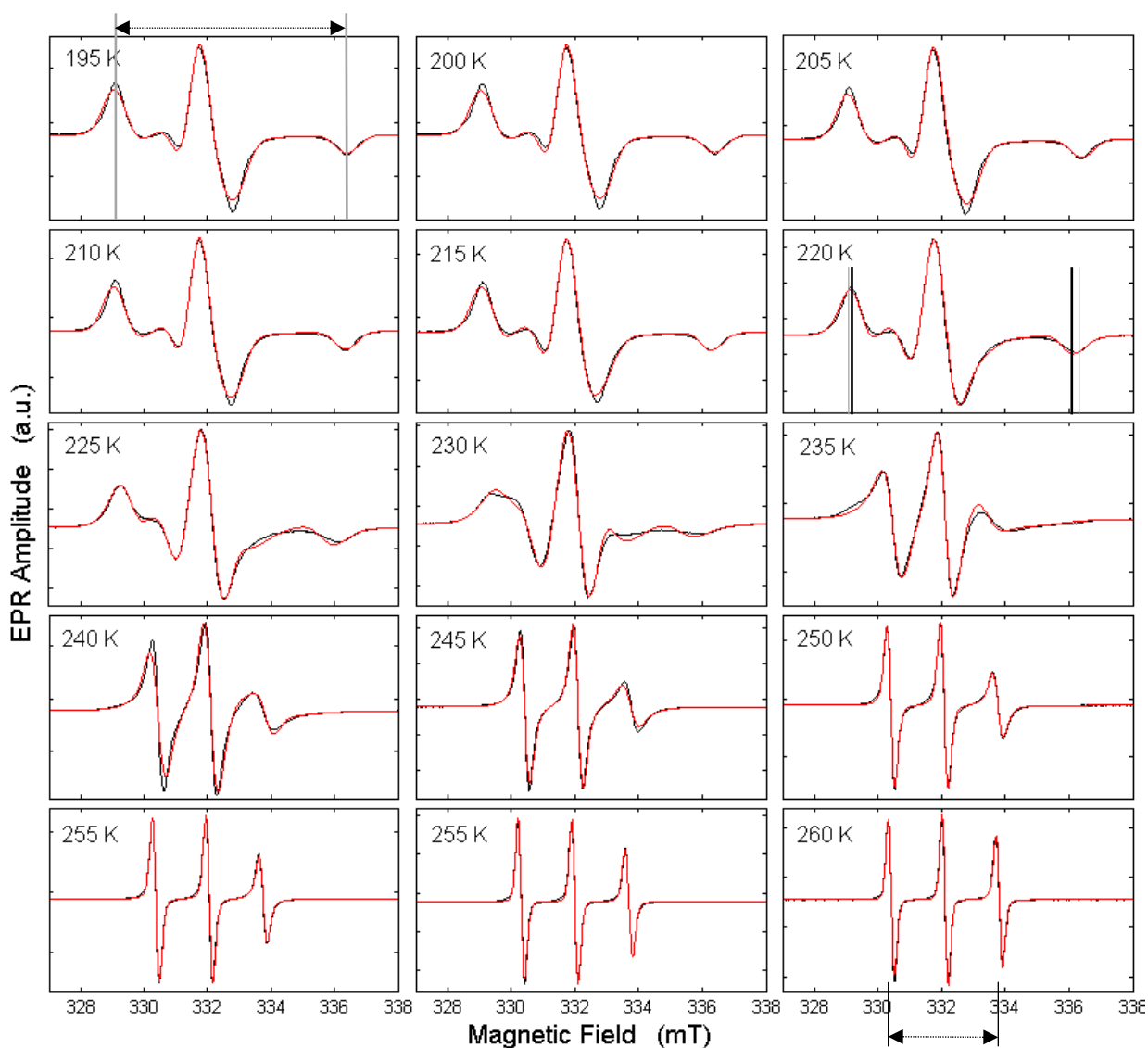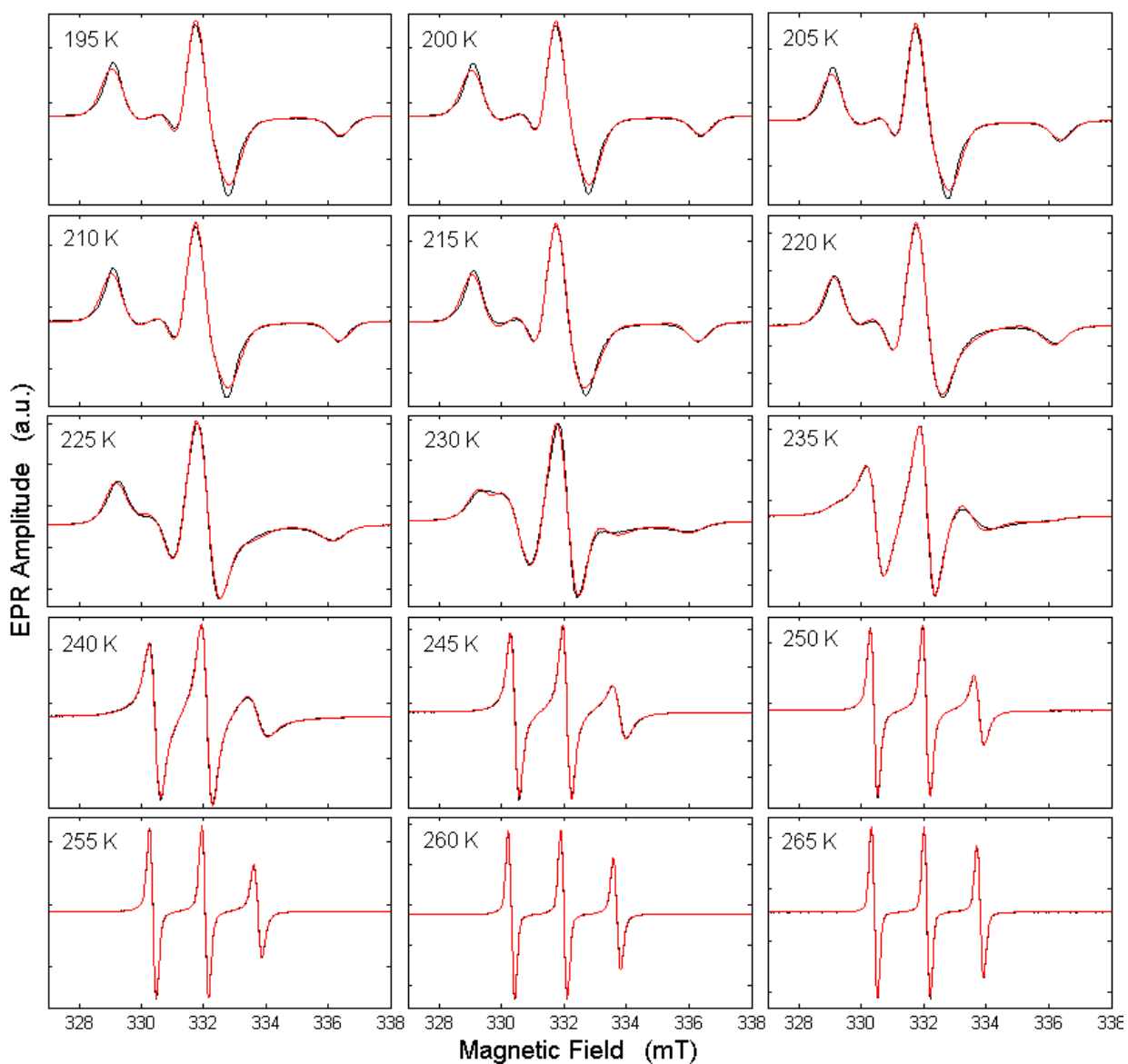
Figure 3-3 CW-EPR spectra (black curves) of TEMPOL spin probe in the aqueous solution of EAL and 2-AmPrOH at 195 – 265 K, overlaid with the EasySpin 2-component simulations (red curves). The fit parameters are listed in Table 3.2

The $\log(\tau_c)$ and *lw* parameters that are obtained from the 2-component simulation fitting
are listed in Table 3.2.

Table 3.2 The parameters that are obtained from the 1-component EasySpin simulation fitting to
the EPR data. The simulation fits are shown in Figure 3-2.

T (K)	Component 1			Component 2			RMSD
	$\log(\tau_c)$	lw	Weight	$\log(\tau_c)$	lw	Weight	
195	-5.30	0.71	0.48	-5.08	1.03	0.52	0.023
200	-5.39	0.67	0.35	-5.25	0.96	0.65	0.021
205	-5.88	0.63	0.38	-5.28	0.95	0.62	0.022
210	-6.63	0.53	0.19	-6.37	0.90	0.81	0.016
215	-7.40	0.86	0.62	-6.50	0.66	0.38	0.021
220	-7.87	0.78	0.52	-7.08	0.67	0.48	0.015
225	-8.14	0.81	0.49	-7.55	0.58	0.51	0.011
230	-8.37	0.63	0.61	-7.70	0.54	0.39	0.016
235	-8.60	0.27	0.47	-8.19	0.66	0.53	0.011
240	-8.81	0.24	0.62	-8.39	0.66	0.38	0.012
245	-9.04	0.21	0.67	-8.63	0.60	0.33	0.008
250	-9.25	0.19	0.73	-8.92	0.56	0.27	0.005
255	-9.47	0.16	0.77	-9.13	0.59	0.23	0.004
260	-9.70	0.17	0.80	-9.34	0.60	0.20	0.004
265	-9.90	0.18	0.82	-9.70	0.63	0.18	0.004

3.4   Discussion

The EasySpin simulation fitting to the EPR spectra of TEMPOL in the frozen solutions
that contain EAL and AmPrOH suggests that the amplitude of the molecular motion in the solvent
mesodomain reaches the dimension scale of the TEMPOL molecule at about 220 K. Thus, the
motion of the spin probe becomes EPR-detectable at $\geq$ 220 K on as the amplitude of the motion
enters the window of X-band EPR sensitivity. This is evident from the visual inspection of the
decrease in the outer line width that starts to show at 220 K, as stated before. Below 220 K, the
spin probe is considered in rigid limit. With the EasySpin function that assumes a mobile spin
probe, the 1-component simulations captured the peak features and fitted to the EPR spectra well.

The 2-component simulation fittings do not improve the goodness of the fits as seen in Figure 3-2 and the RMSD values that are listed in Table 3.1 and Table 3.2. Therefore the 1-component simulations are accepted for 195 – 220 K for the final evaluation of the data.

At $225 < T \leq 235$ K, the 1-component simulations fail to reproduce the high- and low-field peaks (Figure 3-2), which shows that the spin probe motion have more than one component of motion at these temperatures. The 2-component simulations of the EPR spectra at 220 – 235 K (Figure 3-3) represent unequivocally better fits with two approximately equal populations of "fast" and "slow" molecular motion components (Table 3.2). The temperature dependency of the respective weights of the two populations indicates a transition that starts at 235 K that causes the fast component to become more dominant. At 250 K and above, the fast component reaches an average weight of 0.8 compared to that of 0.2 for the slow component (± 0.02). The predominance of the fast component appears as a return to the 1-component behavior (Table 3.2) at the above 250 K temperatures. Therefore, the spin probe mobility has two components at 225 – 250 K and the spectra at these temperatures are fitted by 2-component simulations. Above 250 K, as the contribution of the slow component to the motion becomes ignorable, and the 1-component simulations fit satisfactorily to the spectra, 1-component simulations will be used for further discussion.

The temperature dependencies of the fit parameters that are obtained from the simulation fitting are shown in Figure 3-4 and Figure 3-5. The aforementioned dynamical transition, as well as the emergence of the two phases of motion are reflected in the figures.

The $\log(\tau_c)$ values are shown with respect to temperature in the semi-logarithmic plot in Figure 3-4. After entering the X-band EPR detection sensitivity window at 220 K, the TEMPOL

motions continue with one component up to 225 – 230 K range, around which the solvent enters the dynamical transition region. Between 230 and 250 K, while a population of TEMPOL molecules exhibits the fast tumbling which could be seen as the continuation of the 1-component motion phase at the low temperatures, there also exists a slower TEMPOL population which remains on a slower scale motion. The respective weights of the two populations with respect to temperature are shown in Figure 3-5. Above 250 K, the EPR spectra are fitted by 1-component simulations.
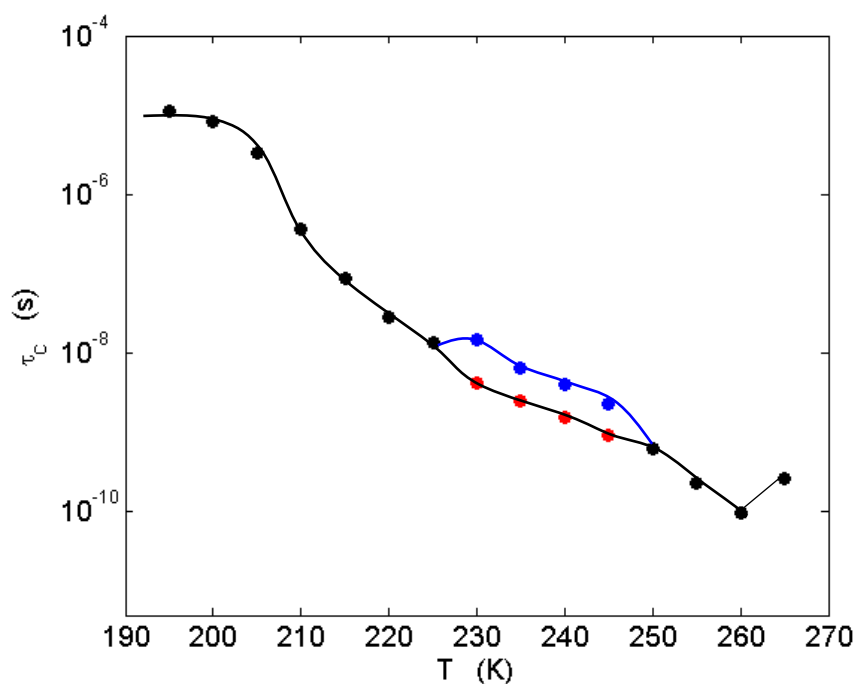
Figure 3-4 The temperature-dependence of the τ_c values of the TEMPOL in EAL and AmPrOH. The solid black lines show the τ_c values from the 1-component simulations. The blue and the red lines are the τ_c values from the 2-component simulations. The overlaid lines are drawn for the visualization of the bifurcation of the TEMPOL τ_c values at the solvent dynamical transition region at ~ 225 – 250 K. The associated data are listed in Table 3.1 and Table 3.2.

As seen in the temperature-dependence of the respective weights of the two populations in the 2-component simulations in Figure 3-5, the slow and fast populations have closer proportions

with each other at the beginning of the transition, and the slow population starts decreasing after

235 K. Above 250 K, the fast component of the motion of the TEMPOL molecules are dominant,

so the 1-component simulations are used for these temperatures.
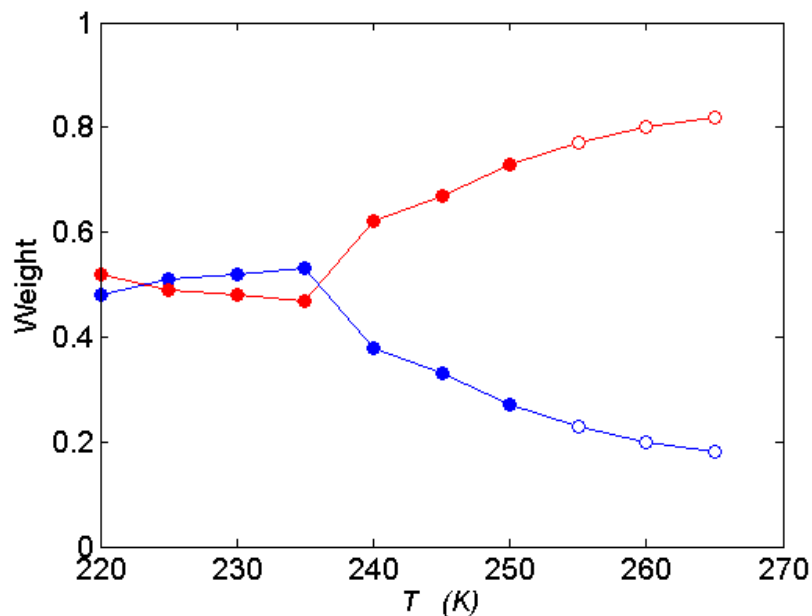
Figure 3-5 The weights of the two populations in the 2-component simulations are shown with respect to temperature. The 2-component simulations are used for the temperatures 230 – 250 K, which are shown with full circles and highlighted with the drawn curves in blue and red colors for the slow and the fast phases, respectively. After 250 K, the circles become open and the curves are drawn with dashed lines to emphasize the fact that at these temperatures the 1-component simulations are accepted, because of the apparent decrease in the weight of the slow component compared to the fast component. The associated data are listed in Table 3.1 and Table 3.2.

3.5 Conclusions

The 1- and 2- component simulations and their fit parameters indicate four temperature regions:

(I) 190 – 225 K: At 215 K, the tumbling time is in the order of 10^{-7} s and becomes detectable with the X-band EPR which has a sensitivity window of 10^{-7}- 10^{-10}. Below 215 K, the TEMPOL molecules are either immobilized in the mesodomain structures, or exhibiting slow rotational-diffusive motions that cannot be detected. Therefore the first critical temperature in this study is 215 K, at which the amplitude of the TEMPOL molecular and atomic motions enters the detection window. Because of the sensitivity window, a protein glass-like transition which is observed in proteins at 180 – 200 K in the absence of the bulk aqueous solvent cannot be observed at the low temperature end. Therefore:

> ➤ TEMPOL motion is not detectable by X-band EPR below 215 K.

> ➤ At 220 – 230 K, the motion becomes detectable, and has one component.

(II) 230 – 245 K: The spectra feature a second component of TEMPOL motion with approximately equal amplitudes until 245 K. At this temperature range, the mesodomain structure could be entering another solvent-dynamical transition region where the thermal motions of the TEMPOL constitute two populations with different tumbling rates. This could be because of a heterogeneity in the solvent structure as the solvent-dynamical transition occurs.

(III) 250 – 260 K: the slowly-tumbling TEMPOL population disappears, and the TEMPOL tumbling becomes a one-component motion again. At 240 K mark, the heterogeneity

in the solvent structure may be diminishing and allowing TEMPOL tumbling to be more uniform.

(IV)   260 – 265 K: The crystalline water that resides at the boundaries of the mesodomain starts "melting" and allows the diffusion of the EAL that is locked in these boundaries to the mesodomain. This increase in the concentration of the EAL reflects as an increase in the viscosity of the mesodomain, which may be the reason for the slowing of the TEMPOL motion in the mesodomain that is seen in above 260 K.

These temperature ranges are overlapping the critical temperatures for the decay of the Co(II)-substrate radical pair decay that is studied in Chapter 2. First, both the Arrhenius relation of the observed rates (Figure 2-15) and the microscopic k_3 rate (Figure 2-18) shows a transition at T>240 K. This transition was speculated to be originated from the solvent-dependent configurational relaxations; as the solvent conditions change the active site geometry, the substrate configuration that undergoes the native reaction is proposed to be favored. In this chapter, we had a supporting evidence that 240-245 K is indeed a critical temperature in terms of solvent transitions, as stated in the temperature region II above, within this temperature TEMPOL starts showing a two-component motion, which is the indication of an ongoing dynamical transition that TEMPOL has to adapt. The mobility that just started to increase in this temperature region may yield an increase in the protein active site mobility too, and this can make the substrate favor its native conformation.

Another important temperature that appears in the Chapter 2, and again was considered to be related to the solvent dynamics was found by the substrate/product exchange experiments. It is shown that the excess substrate that is locked in the crystal water at low temperatures starts its diffusion back to the protein active site, which is indicative of a major solvent transition, i.e.

mesodomain melting, that occurs at T>250 K in Chapter 2. In this chapter, this temperature point is covered in both regions III and IV above. At 250 K mark, the TEMPOL mobility became a 1-component motion again, which means that the solvent becomes homogeneous again after the transition in the previous region, the mesodomain also could start melting within this temperature range, however the melting became evident at 260 K in this chapter. At T>260, the rotational correlation time showed an increase, which means the T-value decreased and the viscosity increased in the solvent around TEMPOL. This fits to the idea of mesodomain melting, as the crystal-water boundaries start melting and the locked EAL can diffuse in the mesodomain, the EAL concentration in the mesodomain increases to make the mesodomain at highest viscosity and make TEMPOL have larger rotational correlation times.

In future, in order to accompany the results of this chapter with the kinetics measurements that are held at Chapter 2, new kinetics measurements of the Co(II)-substrate radical decay may be planned at temperatures at T<220 K temperatures. Because, we showed in this chapter that the decrease in the rotational correlation time (hence the increase in the T-value) that occurs around at 200-215 K (region I in the above list) signifies the TEMPOL molecular motion that has a comparable length scale with the protein side chain or substructure motions. Therefore, the lowest temperature in the Co(II)-substrate radical decay measurements does not cover the temperature range at which the TEMPOL results are in the same length scale with the protein structural motion.

Chapter 4

**Characterization of Adenosylcobalamin
Homolysis and Co(II)-Radical Pair Formation
by using Ethylene Glycol as Quasi-Substrate**

4.1   Introduction

4.1.1   Literature Review

EAL catalyzes the deamination of the aminoethanol and (R)- and (S)-2-aminopropanol through the multistep reaction cycle (see Chapter 1.1.2). In this minimal proposed mechanism, the adiabatic radical rearrangement step is the central reaction which has the homolytic cleavage of the Co-C and the hydrogen-transfer reaction on one side that is forming the radical state, and reverse hydrogen-transfer and recombination of Co-C bond reactions on the other side to reform the diamagnetic state. In order to elucidate the role of the protein in stabilizing and utilizing the -otherwise- highly reactive radicals, understanding the kinetic, mechanistic and energetic properties of this reaction cycle at single-step resolution is essential. In Chapter 2, the EPR spectroscopy is used with a cryoenzymologic approach in attempt to elucidate the reaction steps that are set after the accumulation of the Co(II)-substrate radical pair. In this chapter, the goal is understanding the features of another key step, which is the homolytic cleavage of 5'-deoxyadenosylcobalamin to form Co(II) and Ado• (Figure 1-5), by using optical absorption spectroscopy at the ultraviolet-visible (UV-vis) band.

The features of the Co-C bond cleavage in EAL holoenzyme have been studied extensively as the holoenzyme accelerates the cleavage rate by approximately 10^{12} -fold compared to that of the cofactor in free solution [33, 35, 36, 101]. The question of how the enzyme yields the facile cleavage of Co-C bond still remains open-ended despite several proposed hypotheses involving the compression [102-104] or the lengthening [105] of the axial Co-N bond, the distortion of the corrin ring structure by the surrounding side chains [106-109], and the structural effect of the binding of the substrate [110, 111]. Although the nature of the role of the holoenzyme on the Co-

C bond cleavage has not yet been fully understood, previous studies revealed important structural, kinetic and dynamical properties of this reaction. The studies using FT-Raman [112], resonance Raman [113, 114] and X-ray crystallography [115] led to a better understanding of the structural properties of the coenzyme B_{12} and the identification of the different ligand conformations. Later, in 2009, Wang and Warncke studied the kinetics of the formation of the 2-aminopropanol generated-Co(II)-substrate radical pair, using EPR spectroscopy with a DMSO/water cryosolvent system for kinetically arresting the reaction complexes, and made accompanying low-temperature UV-vis spectroscopy and photolysis measurements as well [67, 116], to show EAL configurational entropic contributions to the Co-C bond cleavage.

This study focuses on the kinetics of the Co-C bond cleavage in the AdoCbl-enzyme complex in a fluid solution, and at near-physiological temperatures (5 – 23 ℃) by using UV-vis absorption spectroscopy. The observation of the Co-C bond cleavage at higher temperatures, compared to the previous studies, was possible with the use of a slower quasi-substrate, ethylene glycol (EG) [49, 50, 117]. The EG promotes the EAL catalytic activity from the Co-C bond cleavage step to the product formation. However, EG has been reported to inactivate EAL after a single turnover by coordinating a different ligand of the coenzyme to the 6th position of the Co center [49]. It is speculated from the spectral analyses that the cobalamin can be replacing the 5'-deoxyadenosyl upper ligand with a sulfhydryl group from presumably a cysteine residue in the active site [49].

The potential for UV-vis spectroscopy for monitoring the time-dependent kinetics of the Co-C bond cleavage is pivotal, as the UV-vis spectroscopy stands as one of the most well-established, accurate, simple, versatile and cost-effective techniques for investigating biological

systems with an organometallic cofactor that have distinct spectral features for different oxidation levels [118].

4.1.2 Basics of the UV-Vis Absorption Spectroscopy

UV-visible absorption spectroscopy is the interaction of matter with the absorbed radiation which falls within the visible range (400-700 nm) in the electromagnetic spectrum. The absorption of the different frequencies of the UV-vis radiation is typically associated with two types of transitions in the electronic configurations of molecules:

a) bonding to anti-bonding ($\pi \rightarrow \pi^*$)

b) non-bonding to anti-bonding (n$\rightarrow \pi^*$)

Transition metal complexes absorb visible light because of several factors, such as the geometry of the complex, oxidation state of the metal or the coordination of the ligands that cause the splitting of the d-orbitals. The interaction between the molecular orbitals of $3d$ metal and the ligand orbitals forms π bonding and n non-bonding orbitals, and the transitions between these and when electromagnetic radiation (i.e. visible light for the optical spectrometers) of correct frequency is absorbed, a transition is occurred from these orbitals to an anti-bonding orbitals. The optical spectrometer records the amplitude of the absorption and wavelengths at which the absorbance occurs.

A typical UV-vis spectrometer contains a combination of tungsten/halogen (visible radiation) and deuterium (UV radiation) lamps as the light sources. The light first passes through a monochromator and then interacts with the sample which is held in a container called cuvette, and also a sample that contains the solvent of the sample as a reference. The transmitted light is

measured with a photodetector and converted to absorbance versus wavelength curve. The quantitative knowledge that an absorption spectroscopy gives is the concentration, as the absorbance is directly proportional to it via the Beer-Lambert Law:

$$A_\lambda = \varepsilon_\lambda \times C \times l \qquad\qquad \text{Equation 4-1}$$

where A_λ is the absorbance at a wavelength λ, ε_λ is the constant called as the extinction coefficient, C and l are the concentration and the length of the path the light takes in the cuvette, respectively.

The UV-vis spectroscopy also can be used at a fixed wavelength to acquire the time-dependence of the absorption as a function of time. This function was particularly useful for the steady-state kinetics measurements, for which the substrate is present in excess and the concentration of the enzyme-substrate complexes remains constant [119]. This way, the Michaelis-Menten kinetic analyses are made for the catalytic rates and parameters of an enzyme.

4.1.3   Optical Features of AdoCbl

Vitamin B$_{12}$ cofactors have a Co(III) at the center of the corrin ring which is known as cobalamin when axially coordinated by a nitrogen from the tethered base DMB, and as AdoCbl when the 5′-deoxyadenosine (Ado) is the upper axial ligand (see Figure 1-1 and Section 1.1.1 for more details). The corrin π orbital system contains 14 electrons distributed over 13 atoms (see Figure 1-1) and is reported to display $\pi \rightarrow \pi^*$ electronic transitions in the near-UV to visible region [11]. In Figure 4-1, the UV-vis spectrum of the AdoCbl in the aqueous solvent (10 mM potassium phosphate, pH=7.5) in EAL is presented (solid line). The spectrum has two distinct features at (i) γ-band at UV region (around 340 and 377 nm) and (ii) α/β bands at 525 nm and 490 nm in the

visible region. The α/β features are commonly acknowledged as originating from the same $\pi \rightarrow \pi^*$ electronic transitions with α and β bands representing the electronic transition and vibrational progression along the $C^5 \cdots C^{15}$ axis of the corrin ring, respectively [11, 13, 120].

In this study, the AdoCbl spectra are collected in the presence of the EAL (Figure 4-1, solid line) and EG is added by using a home-made fast mixing method to initiate the Co-C bond cleavage. The cleavage of the Co-C bond creates the 5'-deoxyadenosyl radical (Ado·) and the Co(II) intermediate, which is also known as cob(II)alamin. In order to obtain a pure UV-vis absorption spectrum of cob(II)alamin, the cob(II)alamin is formed artificially by the anaerobic photolysis of the AdoCbl (Figure 4-1, dashed line). This spectrum represents the change in the spectral features as the cleavage reaction occurs; a decrease in the α/β features with new features emerging at around 475 nm and UV-region.
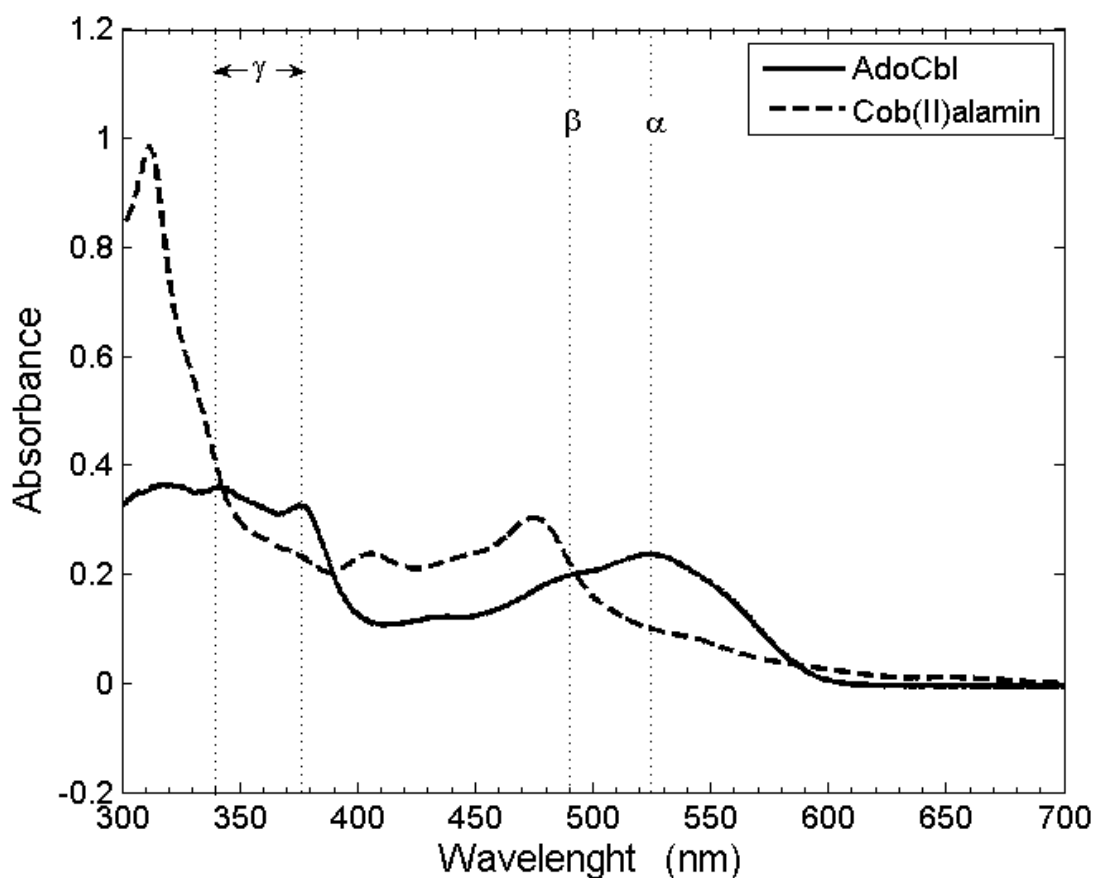
Figure 4-1 The UV-vis absorption spectra for the AdoCbl in EAL (solid line), and cob(II)alamin (dashed line). The grid lines represent the distinct spectral features at the visible region (α and β bands) and UV-region (γ band). The solution for both samples was 10 mM phosphate buffer at pH 7.5. The spectra are recorded at room temperature.

4.1.4 Project Overview

The role of EAL holoenzyme in the acceleration of the rate of the homolytic cleavage of the Co-C bond has not been fully understood yet. Elucidation of the kinetics of the Co-C bond cleavage is essential for obtaining a complete picture of this enzyme-mediated catalysis. However the fast steady-state kinetics of the enzyme limits the temperature range of the single-step kinetics studies to the cryogenic temperatures [67]. In this study, the time-dependent kinetics of the Co-C

cleavage step in the EAL holoenzyme is monitored by UV-vis absorption spectroscopy, at the above-zero temperatures by using EG as the substrate of the enzyme. In addition to gaining access to the kinetics at higher temperatures, this experimental approach will allows us to apply the UV-vis absorption spectroscopy to the kinetic studies of EAL catalysis. So far, the EPR has been used for observing the EAL catalysis [29, 67, 69, 121], and providing the information about enzyme kinetics that is based on the radicals. However, UV-vis absorption spectroscopy allow us to use the cobalamin moiety as the probe for investigating the kinetic features instead of the radical. In summary, the hypothesis of this project is that the EG is a suitable quasi-substrate that enables the observation of the kinetics of the Co-C bond cleavage at the native or physiological T range (5 – 23 $^{\circ}$C) using UV-vis absorption spectroscopy, and will reveal the time-dependent kinetics information of the cleavage at this new, native temperature range.

4.2 Materials and Methods

4.2.1 Sample Preparation

All chemicals were purchased from Sigma-Aldrich or Fischer. The deuterated ethylene glycol (Ethylene Glycol-D4 [HOCD$_2$CD$_2$OH]) is provided from the Cambridge Isotope Laboratories (CIL). The EAL is purified according to the descriptions made in section 2.2.1. The AdoCbl-involved sample preparation steps are done under red dim light because of sensitivity of AdoCbl to the light. The sample volume was defined as 550 µl, which provides a sufficient sample height to allow the passage of the UV-vis spectrometer light when put in a 1 ml quartz cuvette in the spectrometer cuvette-holder. The EAL (1 mg/ml, 12 µM active site) is mixed with 10 mM, pH 7.5 phosphate buffer to make a 500 µl solution, and sonicated for about 15 s twice to homogenize the sample. The EAL+buffer mixture was then transferred to the 1 ml quartz cuvette, and the UV-

vis absorption spectrum was collected as the EAL baseline. Then, the AdoCbl is added to the solution to 12 μM, and another UV-vis spectra was run. In a 200 μl plastic reaction tube, the phosphate buffer was mixed with EG to make a 50 uL solution, and added to the holoenzyme solution to 50 mM to initiate the cleavage reaction. The cleavage reaction was monitored as the decrease of the 525 nm absorption of with respect to time. Approximately the first 20 s of the reaction is missed owing to the instrument dead-time.

4.2.2   UV-visible Spectroscopy

The UV-vis absorption spectra are collected by using a Shimadzu UV-1601 optical bench spectrometer. The temperature was maintained by a refrigerated circulating bath of a water – methanol mixture that is connected to the sample compartment with an insulated tubing. In order to prevent the formation of the fog on the sides of the cuvette, dry gas (N_2) at 20 cc/min flowed to the sample compartment. At the times when the lid of the sample compartment was open for adding the components of the sample, the outside surfaces of the cuvette was forming fog even though the dry gas was flowing. In order to overcome this issue, two modifications are made to the experimental setup:

1. A homemade cover is prepared instead of the original lid of the sample compartment which was made of foam and cardboard for the better heat insulation. A small ~ 2x2 cm flipping lid that is placed right above the sample holder is the key feature of this cover. A 1000 μl - pipette tip could reach to the cuvette through this lid without forming fog.

2. The fast injection of EG was needed to minimize the exposure of the sample compartment to the room temperature. The fastest mixing (~5 s) was achieved with a 1000 μl - pipette

tip. The tip of the pipette tip is cut for about ~1 mm to prevent the bubble-formation during the fast injection. The EG solution is put in the pipette tip beforehand using a 200 µl pipette. Then the holoenzyme sample which was residing in the cuvette was drawn in and out with this EG solution containing pipette tip.

The experiments were performed at 5 – 23 °C. The spectra of the EAL baseline and the EAL holoenzyme after the AdoCbl addition are collected between 300-700 nm with the slow scan speed setting. Starting with the fast (~5 s) EG injection, time-dependent kinetic measurement is observed at 525 nm at every 0.1 s until the absorbance value decreases to a constant. After this kinetic measurement, the final spectrum of the sample is recorded again in the 300-700 nm range.

4.3 Results

4.3.1 Preliminary spectral measurement

The time series of the UV-visible spectra shows the conversion of the AdoCbl to cob(II)alamin with the rise in the β-band absorbance that corresponds to a decrease in the α-band absorbance (Figure 4-2). This result indicates that the cleavage of the Co-C bond occurs. At 13 min a new feature around 495 nm emerges and interferes with the spectra of the catalytic conversion. In Figure 4-3 the peak absorption values at 525 nm and 475 nm for the AdoCbl and cob(II)alamin is converted to the concentration values of the corresponding species for a better inspection of the observed conversion in the α and the β bands. The concentration values are calculated by inserting the molar extinction coefficient (ε_λ) values that are reported in the previous literature in the Beer Lambert Law (Equation 4-1) [122]. According to Figure 4-3, as the AdoCbl concentration decays in time, the cob(II)alamin concentration rises, until the two values meet after

1 hour of the initiation of the reaction. In order to compare the observed kinetics of the two reactions curves, the concentration values are normalized to the $t = \sim 8$ min value (the time point where the two curves stabilize), and the decay of the AdoCbl feature is inverted (Figure 4-3, inset). In Figure 4-3, the overlaid lines are the monoexponential decay and rise functions that are fitted to the two curves with the rates $0.0082\ \mathrm{s}^{-1}$ and $0.0075\ \mathrm{s}^{-1}$ for AdoCbl decay and cob(II)alamin decay, respectively. The kinetics of the two observed curves are close to each other within two standard deviations of each other.
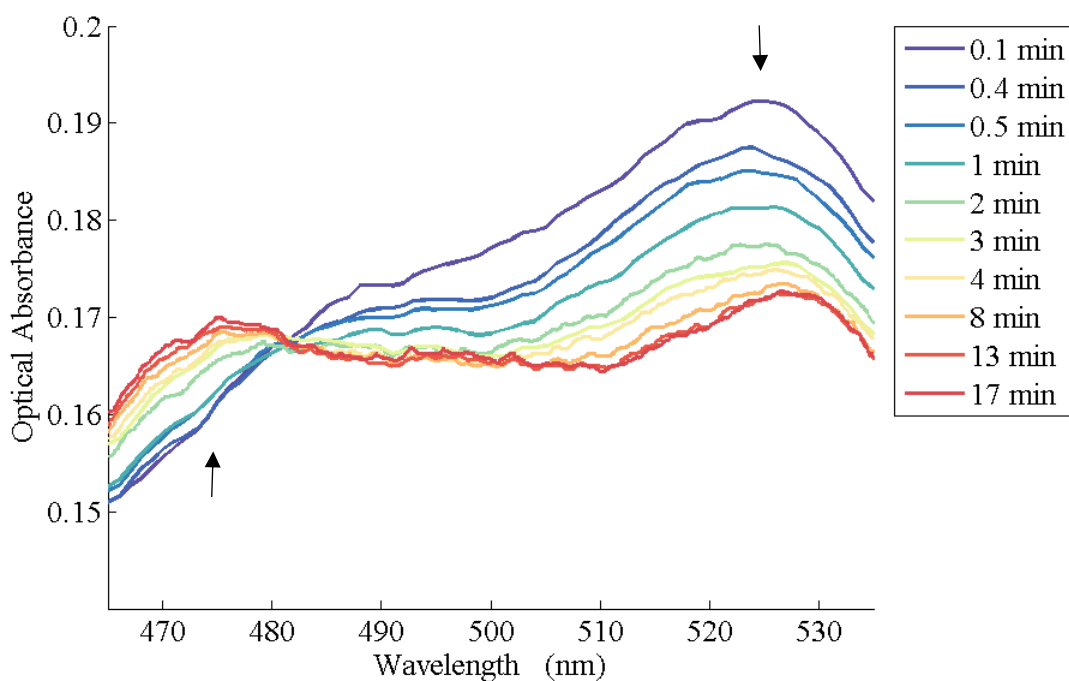
Figure 4-2. The conversion of AdoCbl to cob(II)alamin as a function of time. Spectra were collected immediately after the EG injection, and recorded at the time points that are listed in the figure legend. The progress of the reaction in time is shown by color-coding the spectra at each time point (from blue to red). In order to minimize the sweep time, instead of the $300 - 700$ nm full spectra, only the 460-540 nm wavelength range is swept. The AdoCbl feature at 525 nm is decreasing and the cob(II)alamin feature at 475 nm is decreasing in time as the cleavage reaction occurs (shown with arrows).
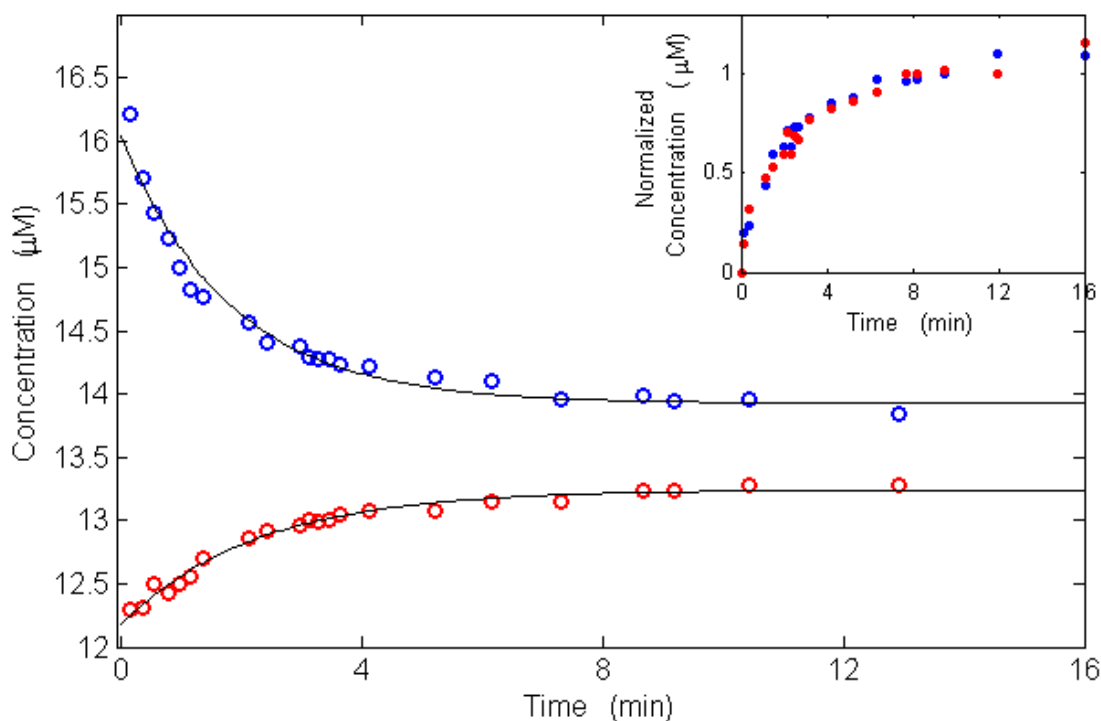
 Figure 4-3 Time dependence of the AdoCbl and cob(II)alamin concentrations for the reaction shown in Figure 4-2. Optical absorption values at 525 nm (blue) for AdoCbl and 475 nm (red) for cob(II(alamin) are converted to the concentration values using the literature values of ε_λ. In the inset, the raw concentration values are normalized to their corresponding values at 9 min because at 13 min a new feature emerges, and the AdoCbl curve is inverted to compare the reaction kinetics.

In Figure 4-3, the change in the AdoCbl concentration is 2.28 μM and this value corresponds to the ∼20% of the total active site concentration. The yield is also low in the previous study accompanying the 525 nm UV-vis spectrum absorption data of the Co-C bond cleavage in the presence of EG, giving a value of approximately 11% from the visual inspection of the time vs. concentration plots provided [49, 117]. Also, the Co-C bond cleavage was studied by the incubation of AdoCbl (labelled with a ^{14}C-5′-deoxyadenosyl moiety) with the EAL in the presence of EG, and the yield for the bond cleavage was found to be 19.4% per active site [49]. From this perspective, the yield that is found in this study is in line with the previous studies. This low yield could be due to the proposed coordination of a new ligand on the central cobalt. A split of the total

initial AdoCbl could be forming a new unknown corrinoid, instead of remaining in the cleaved Co(II) state.

4.3.2 Treatment of the time-coursed kinetics data of single-wavelength absorption

The kinetics of the formation of the EG-generated Co(II)-substrate radical pair is observed in the form of the decrease in the α-band peak (525 nm) of the cob(III)alamin at temperatures 5, 10, 15, 18 and 23 ℃. The Figure 4-4 shows two time-course decay measurements of the optical density at 525 nm OD_{525} at 5 and 15 ℃ as an example of data before further-processing. The conversion of the cob(III)alamin to cob(II)alamin starts with the fast-injection of EG to the cuvette (marked with the yellow stars in Figure 4-4), and the decay of OD_{525} is recorded time-dependently (Figure 4-4). The data after the EG-injection is corrected for the dilution as the EG has a volume of 60 μl of the total final volume of 550 μl. After the EAL baseline correction that is obtained from the EAL-only UV-spectrum and the truncation of the data before the EG-injection, the decay data of the OD_{525} is obtained.
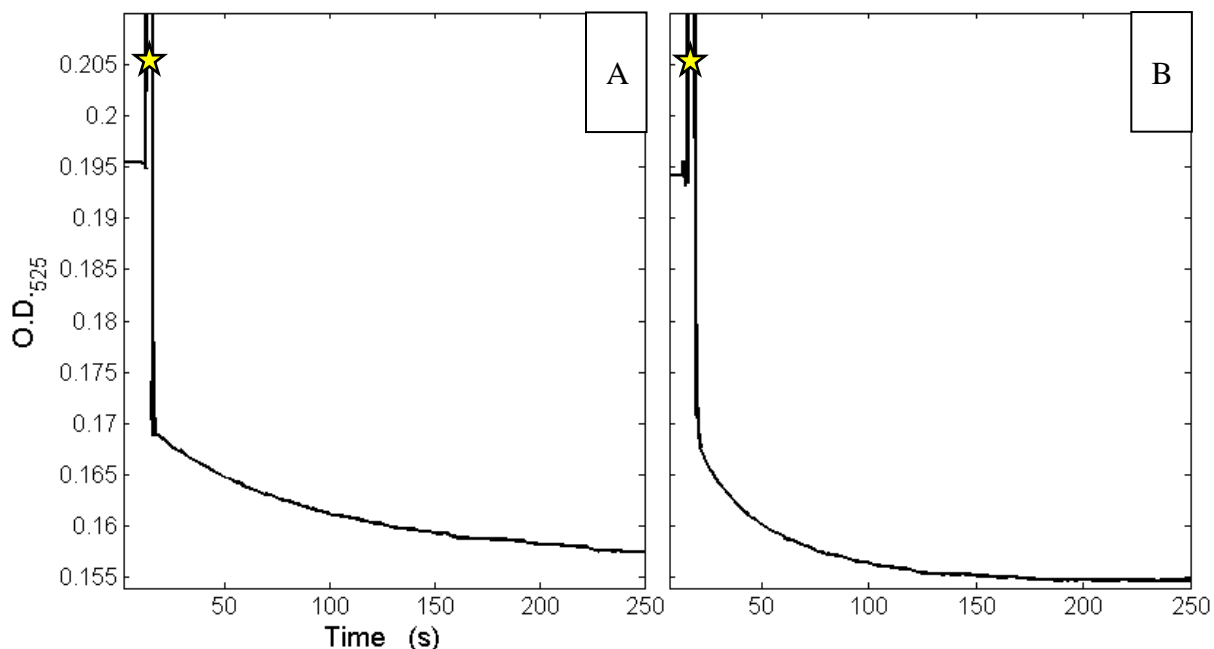
Figure 4-4 Time-course measurement of the decay of the OD_{525} upon the injection of the EG (marked with yellow stars) at 5 (A) and 15 ℃ (B). The sample includes EAL (1 mg/ml), AdoCbl (12 μM), phosphate buffer (10 mM) in a total volume of 490 μl. The 60 μL EG is added to 50 mM at the time points marked with yellow stars.

4.3.3   Dependence of the rate on the substrate concentration

As a second set of preliminary results, the dependence of the observed kinetics on the substrate concentration is measured (Figure 4-5). The EG concentration is varied over a range of 0.5-250 mM while keeping the of the holoenzyme concentration constant. The previous studies, that observe the EG-catalyzed cleavage of Co-C bond in EAL, used excess substrate with different [substrate] : [EAL active sites] ratios that are varying from 30 [49] to 13400 [117]. The concentration range in this measurement corresponds to a [substrate] : [EAL active sites] ratio of about 41 – 21000 and the measurement repeated twice at two different temperatures; 5 and 23 ℃.

Figure 4-5 shows that the observed rate of the reaction remains the same (0.018 ± 0.003 for 5 °C

and 0.101 ± 0.008 for 23 °C). The difference between the initial and the final OD$_{525}$ reading of

AdoCbl remains the same as the substrate concentration increases. The 9.64% (±4.09) of the initial

OD$_{525}$ reading decays at the end of the reaction.
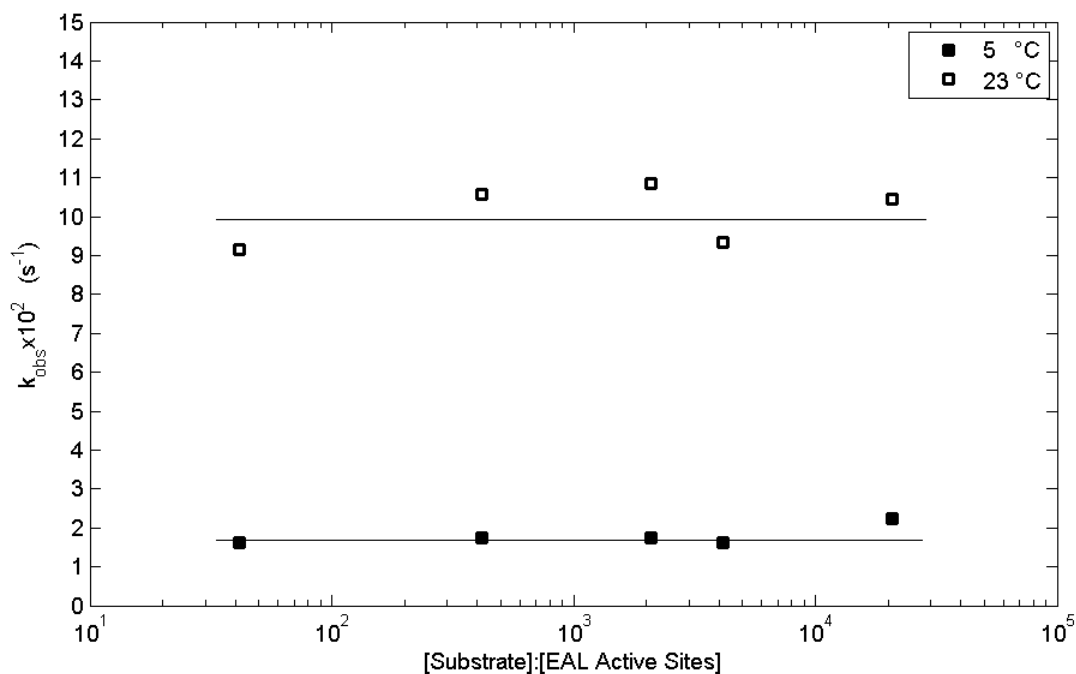
Figure 4-5 Dependence of the observed kinetics of the EG catalyzed Co-C bond cleavage in EAL on the concentration on EG at $T = 5$ °C and 23 °C which are shown with solid and empty black markers, respectively. The lines are the respective best-fit zero-slope lines to the data. The concentration of the EAL active sites is 12 μM.

4.3.4   Time-Course Kinetics Results

The decay of the OD$_{525}$ fits a single exponential function and it is presented in Figure 4-6

overlaid to the decay data. At least 3 measurement are done at each temperature. After each time-

course measurement, a full spectrum is collected for the visual inspection of the cob(II)alamin rise at the β-band (475 nm).
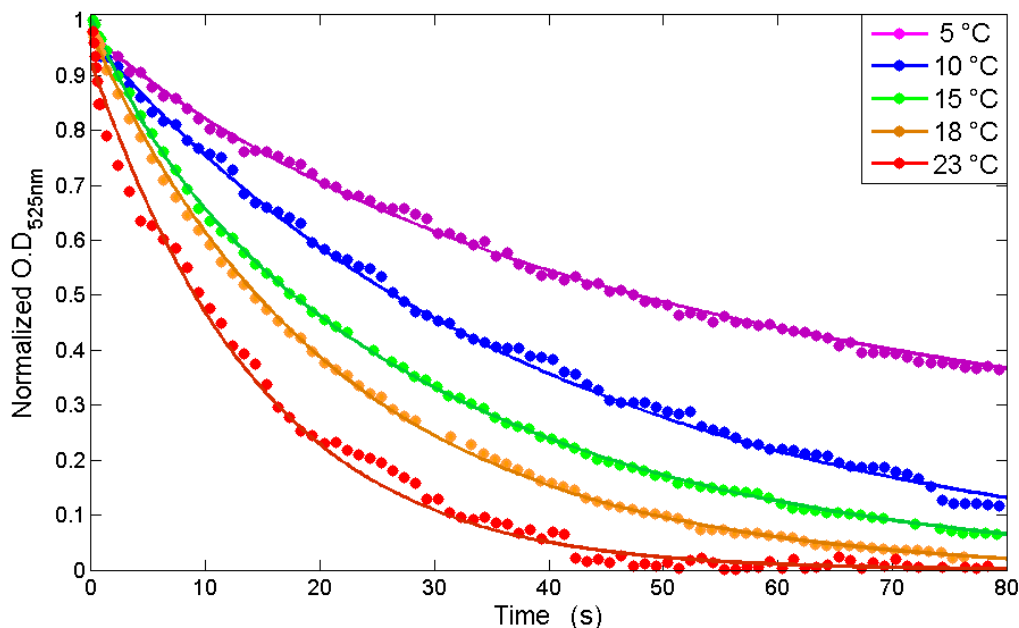
Figure 4-6 Time dependence of the decay of the Co(III) 525 nm absorbance peak at different temperatures with the overlaid single exponential fits. The different colors correspond to the temperatures that are given in the figure legend. The sample includes EAL (1 mg/ml), AdoCbl (12 μM), phosphate buffer (10 mM, pH 7.5) in a total volume of 490 μl. The cleavage is initiated with the addition of 60 μL EG for a final concentration of to 50 mM.

The same measurement is repeated with deuterated EG (EG-d4). The EG-d4 data for the decay of the OD_{525} is also fitted to a single exponential function. The observed rates (k_{obs}) for the OD_{525} decay in the presence of EG and EG-d4, and the ratio of the k_{obs} for ^{1}H/ ^{2}H isotope effect (I.E.) at each temperature are listed in Table 4.1. The average substrate ^{1}H/ ^{2}H isotope effect for all the temperature points is 2.1 $\pm$ 0.4. In addition, the ΔOD_{525} values are calculated from the subtraction of the final OD_{525} values from the initial at each temperature, for both EG and EG-d4. The ratio of the ΔOD_{525} values for EG and EG-d4 was found to be 1.9 $\pm$ 0.5, which is close to total average isotope effect.

Table 4.1 Observed rates that are obtained by the single exponential fitting to the decay of the OD at 525 nm. The column k_H represents the observed rates for the EG, the column k_D represents the observed rates for the EG-d4 and the column k_H / k_D represents the ratio obtained by the division of the k_D to k_H.

T (°C)	k_H (x 10^{-2}) (s^{-1})	k_D (x 10^{-2}) (s^{-1})	k_H / k_D	$\dfrac{\Delta OD_{525,H}}{\Delta OD_{525,D}}$
5	1.08 ± 0.082	0.46 ± 0.022	2.35 ± 0.08	1.92 ± 0.16
10	2.45 ± 0.234	0.94 ± 0.202	2.60 ± 0.24	1.57 ± 0.18
15	3.74 ± 0.217	2.38 ± 0.556	1.57 ± 0.24	2.16 ± 0.06
18	4.61 ± 0.088	2.57 ± 0.062	1.79 ± 0.03	1.92 ± 0.30
23	9.43 ± 0.090	3.69 ± 0.561	2.56 ± 0.15	1.49 ± 0.23

4.4   Discussion

The UV-visible measurements of EG in EAL holoenzyme show that the EG induces the cleavage of the Co-C bond in the coenzyme and the abstraction of hydrogen from the substrate, which is consistent with the results from the previous studies [49, 117].

4.4.1 Comparison of the results with the previous studies

There have been two previous studies that used EG as the substrate of the EAL catalysis, and understanding the results of these studies is essential to interpret the results of this study. First study that specified EG as a quasi-substrate for the EAL kinetics is from 1970 by Babior and made a complete enzymatic analyses on the mechanism of the action of EAL in the presence of EG [49]. Years later, on 2012, Scrutton et al. used EG in their study for investigation of the effect of the EAL on the Co-C bond homolysis using both laser flash photolysis and stopped-flow infrared (IR) techniques, as well as an accompanying UV-vis measurement [117].

Babior studied EAL enzyme catalysis in the presence of AdoCbl and EG using radiometric enzyme assay technique, and the conversion of AdoCbl to the cob(II)alamin is also observed. This study showed that the enzyme catalyzes EG to form the products, but a portion of EG is also reacting with the active site side chains instead of the radical rearrangement step, yielding the AdoCbl coordination with the sulfhydryl group of that residue, which forms a new corrinoid (X-B_{12}) to be gradually converted to hydroxocobalamin. Babior held a UV-vis spectroscopic measurement by adding AdoCbl to start the cleavage reaction in a cuvette containing EAL and AdoCbl and observed the conversion of AdoCbl to the X-B_{12} in 210 s, which had an absorption spectrum with two peaks at around ~535 and ~500 nm in the α band.

In this study, the UV-vis spectra features solely the conversion of the AdoCbl to cob(II)alamin with the decrease of the 525 nm band feature and the rise of the cob(II)alamin feature at 475 nm at the beginning of the decay (until about 10 min of the decay in Figure 4-2). However, at longer times (starting around 10 min after the reaction starts in Figure 4-2), the UV-vis absorption spectra start showing features that are not associated with cob(II)alamin around 492 nm

and 530 nm (see Figure 4-8 and the spectra after 10 min in Figure 4-2). The positions of the α-band peak features of the reported UV-vis absorption spectrum of X-B$_{12}$ are similar to the new features that are shown to be appearing at longer times in this study. This may indicate that after the conversion of the cob(III)alamin to cob(II)alamin upon Co-C cleavage, the substrate abstracts a hydrogen atom from the side chain of an amino acid in the active site and X-B$_{12}$ is derived from this side chain from which the hydrogen atom is taken.

. The formation of X-B$_{12}$ can also be seen in the time-coursed spectra as an increase of the 525 nm absorption signal towards the end of the decay (Figure 4-7). The Figure 4-7 shows a subtle increase after the full decay, and the time-course data stops before observing the rise at later time. The other study that is done at 2012 by Scrutton et al. also features this increase at their UV-vis spectroscopic measurements of the EG-catalyzed Co-C bond cleavage [117].
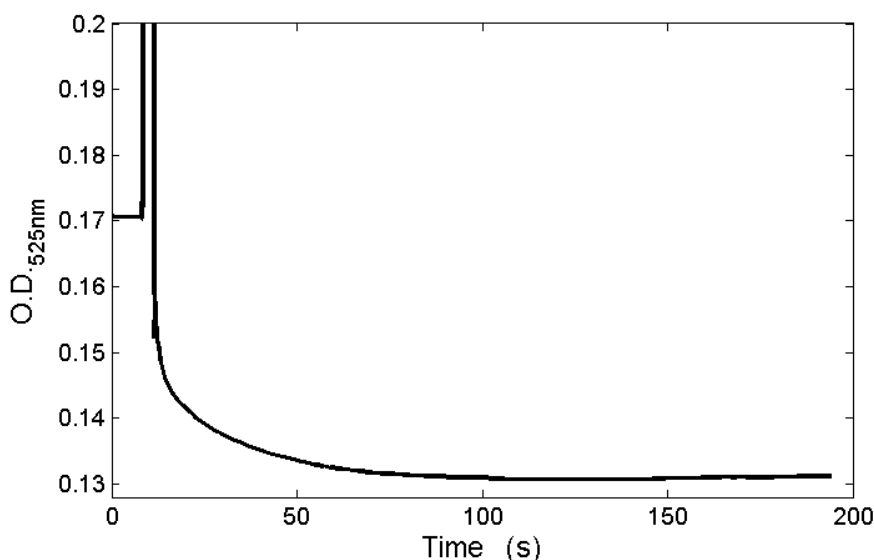
Figure 4-7 An example of the subtle increase of the signal towards the end of the decay of the OD$_{525nm}$ that could be associated with the reversion of the cob(III)alamin on different ligand coordination. The sample includes EAL (1 mg/ml), AdoCbl (12 μM), phosphate buffer (10 mM) in a total volume of 490 μl. The cleavage is initiated with the addition of 60 μL EG is added to 50 mM at 15 °C.
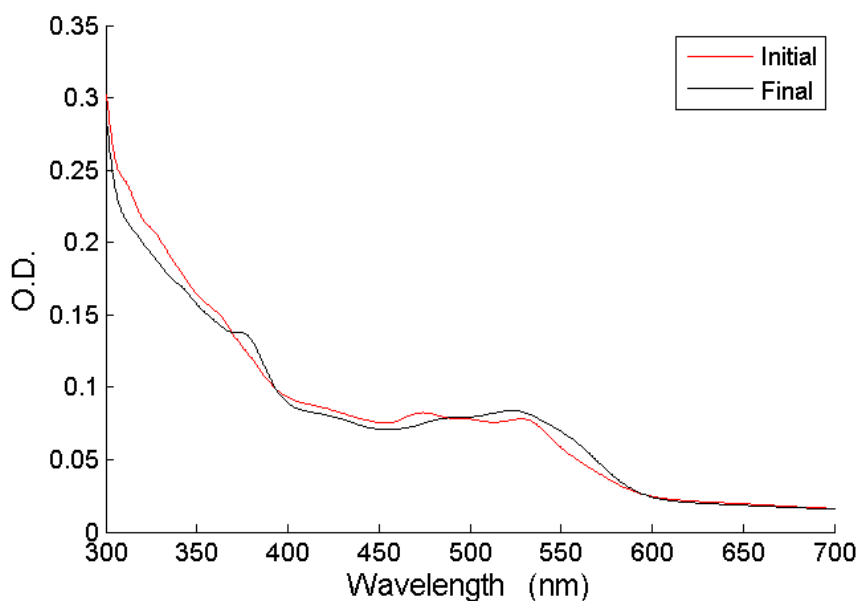
Figure 4-8 An example for the initial and final spectra of the cob(III)alamin to cob(II)alamin conversion in EAL with EG as the substrate. The initial spectrum refers to the spectrum that is collected prior the EG injection, and the final spectrum refers to the spectrum that is collected in a very long time after the time scale of the kinetics measurements. New features emerged around 492 nm and 530 nm, which are not associated with the cob(III)alamin to cob(II)alamin conversion. The sample includes EAL (1 mg/ml), AdoCbl (12 μM), phosphate buffer (10 mM) in a total volume of 490 μl. The cleavage is initiated with the addition of 60 μL EG is added to 50 mM at 15 ℃.

The study that is done by Scrutton et al. investigated the changes in the protein structure by IR methods during the EAL-catalyzed reaction, in addition reports a stop-flow UV-vis spectroscopic measurement of the EG-catalyzed Co-C bond cleavage. In their time-coursed kinetic measurement of the decay of the AdoCbl, they observe an increase in the OD_{525} value at after ~8 s of the start of the reaction at ambient temperatures, however, in this study this increase starts after ~150 s of the start of the reaction at 23 ℃. This difference may be due to the excess substrate (800 mM of EG with 30 μM of EAL) that the Scrutton et al. used, i.e. more EG can destruct the

active site side chain to form X-B$_{12}$. In this study, the substrate is also excess (50 mM of EG with 12 µM of EAL active site) but not in the order of the Scrutton et al. study, so the increase of the OD$_{525}$ value is subtler and occurs at longer times.

The yield in this study is given as 19.9% in Figure 4-2, and is found 13.72% (±2.48) by averaging all the collected data. Neither of the previous studies have not reported a stoichiometric yield for their UV-vis measurements, but from the visual inspection of the OD$_{525}$ values in the given time-coursed decay plot, the yield is approximately 5-6 % for Scrutton et al. and 20% for Babior's measurement. Therefore, all three studies remained at low-efficiency which can either mean that the enzyme is not forming a reaction complex at its full active site capacity, or the Cob(II)alamin that is formed after the cleavage follows the EG destructive path to form a new Cob(III)alamin, X-B$_{12}$. Since the spectral evidence and the time-coursed measurements also support an interfering increase in the α-band region, the latter could be likely occurring.

The Scrutton et al. study has not present the cleavage rate values that are found by the time-coursed decay data of the OD$_{525}$ value. However, from the visual inspection of their decay plot, the order of magnitudes of the cleavage rates are matching with the 23 ℃ rates in this study.

4.4.2 The Co-C bond cleavage kinetics using the deuterated substrate

The EG-d4 measurements were performed in order to inspect whether the observed reaction corresponds to the native HT1 step (Figure 1-5), or to the radical rearrangement step. Previously, the hydrogen isotope effect was studied by using stopped-flow spectrophotometric measurements for the Co-C bond homolysis reaction in the EAL in the presence of the deuterated aminoethanol and (S)-2-aminopropanol as the substrate and calculated as >10 and 3, respectively [121]. The hydrogen isotope effect is explained by: (i) having the Co-C bond cleavage step

concerted with the HT1 step, however seem unlikely because it is not feasible for the 5′-deoxyadenosyl radical has to take the distance of 8-11 Å between the Co and the substrate radical, (ii) effect of the substrate on the equilibrium between the intact and the homolyzed coenzyme, that is as the substrate reacts with the 5′-deoxyadenosyl radical, because of the high free energy of that state, the reaction would be driven to the formation of the intact coenzyme. In order to further investigate the origin of this kinetic isotope effect on the Co-C bond homolysis, Wang&Warncke studied the kinetics of the (*S*)-2-aminopropanol-generated Co(II)-substrate radical formation in EAL in DMSO/water cryosolvent system at 234 – 248 K, and found a kinetic isotope effect that is close to the unity [67, 76]. They interpreted this absence of the kinetic isotope effect as the Co-C bond cleavage and the HT1 steps not being kinetically coupled at low temperatures, and Co-C bond cleavage is the rate-determining step upon the Co(II)-substrate radical pair formation.

In this study, the presence of the isotope effect at a value of 2.1 ± 0.4 supports the previous studies that are based on the visible absorption readings with the stopped-flow method at ambient temperatures [121]. This result may suggest that, at these temperature and solvent conditions that are closer to the physiological values, the intact and the cleaved state of the coenzyme forms an equilibrium, to be perturbed to recombine the intact coenzyme upon the substrate addition. Also, in the case of this study, the isotope effect can be explained by the role of the substrate in the abstraction of a hydrogen from a side chain that yields the formation of the X-B$_{12}$.

4.4.3   Arrhenius relations of the EG and EG-d4

In order to obtain the Arrhenius parameters, the logarithm of the rates in Table 4.1 are plotted with respect to the inverse temperature in Figure 4-9 with the fit parameters listed in Table 4.2. The linear Arrhenius shows that the rate limiting step remains the same through the given

temperature rate. Also, the Arrhenius parameters in Table 4.2 shows no significant kinetic isotope effect, which indicates that the absence of a large primary kinetic isotope effect. According to the findings so far, the observed reaction seemed to be the mainly Co-C bond cleavage reaction only as the effect of the radical rearrangement step cannot be traced from the data that is presented so far. The effect of the HT1 step should have made a larger isotope effect, however this low kinetic isotope effect values are indicating a secondary kinetic isotope effect.
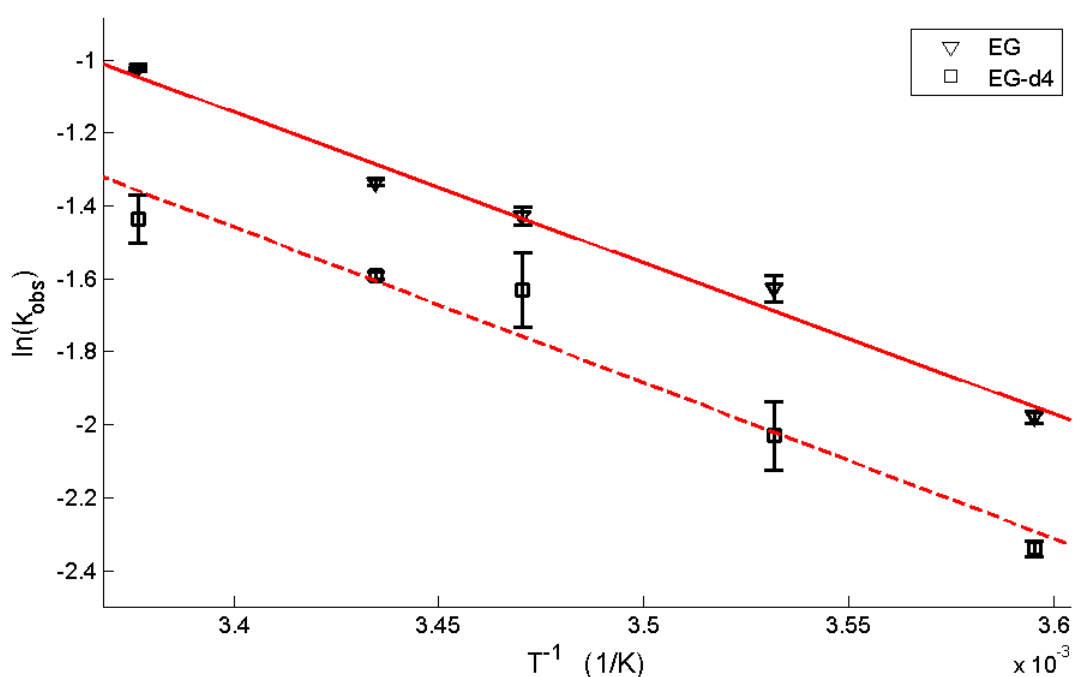
Figure 4-9 The Arrhenius plots that is obtained by the observed rates of the EG (open triangles) and deuterium bound EG (EG-d4) (open squares). The linear fits to both data sets are shown overlaid to the data in solid and dashed red lines, respectively. The associated fit parameters are listed in Table 4.2. The sample includes EAL (1 mg/ml), AdoCbl (12 μM), phosphate buffer (10 mM) in a total volume of 490 μl. The cleavage is initiated with the addition of 60 μL EG is added to 50 mM.

Table 4.2 Fitting parameters for Arrhenius reaction rate expressions for the EG and EG-d4.

	$\mathbf{Log}[A\ (s^{-1})]$	E_a (kcal mol^{-1})	R^{2a}
EG	12.47 ($\pm$0.78)	7.95 ($\pm$0.82)	0.9875
EG − d4	11.91 ($\pm$0.95)	7.80 ($\pm$2.59)	0.8843

[a]R is the Pearson's correlation coefficient

Warncke et al continued their investigation of Co-C bond homolysis step in a subsequent study, where they combined their EPR measurement data on the (*S*)-2-aminopropanol-generated Co(II)-substrate radical formation with the equilibration perturbation experiments and wrap their findings and interpretations for a complete energetic picture of the Co-C bond cleavage step [123]. They found that the Co-C cleavage at their low T measurements is the rate-limiting step, and by extrapolating their stopped-flow visible spectroscopic data to the ambient temperatures, they predicted that the rate limiting step at higher temperatures would be the radical rearrangement step. This cannot be observed in this study because of using EG, which evidently destructs the catalytic cycle and do not proceed with the radical rearrangement step. As the Warncke et al.'s later study accepted that their system is in equilibrium, they made Eyring analyses of their rates to find the activation energy parameters. They found that the activation entropy and enthalpy values Co-C bond cleavage at low temperatures in the presence of (*S*)-2-aminopropanol as the substrate as $\Delta S^{\ddagger} = 61 \pm 6$ cal/(mol·K) and $\Delta H^{\ddagger} = 32 \pm 1$ kcal/(mol·K). The Gibbs free energy at 248 K is then calculated as $\Delta G^{\ddagger} = 17 \pm 2$ cal/(mol·K). They've found that the Co-C bond cleavage is large

122

entropy-based by comparing the energetic values of the cleavage reaction in the solution and

protein [123, 124].

By assuming that the Co-C bond cleavage is also rate-limiting step in this experiment, the

Eyring plot for the observed rates is made in Figure 4-10 and the activation energy parameters that

are calculated from the Eyring plot linear fit parameters are shown in Table 4.3.
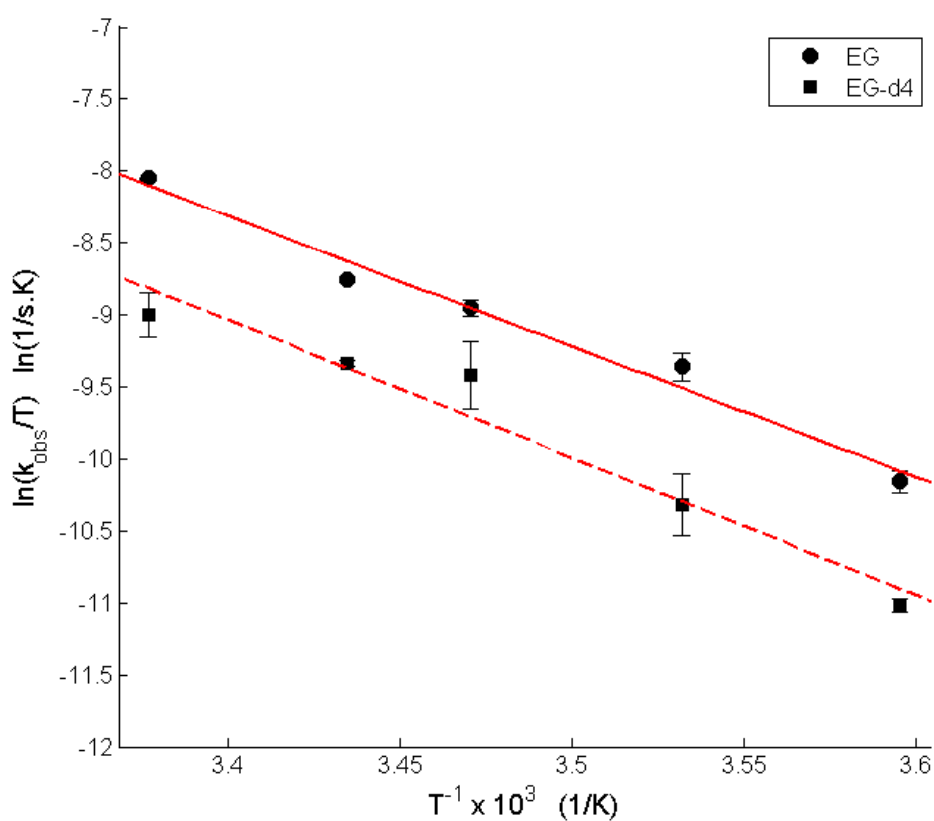
Figure 4-10 Eyring plot for the observed rate constants of the Co-C bond cleavage in the presence of EG at 5-23 °C: EG and EG-d4 cleavage rates are shown in full circles and full squares, respectively. The best-fit linear lines are overlaid and the activation energy parameters that are found by the fit parameters are shown in Table 4.3.

Table 4.3 Fitting parameters for Eyring plot for the EG and EG-d4.

	$\Delta H^{\ddagger}$ kcal/(mol·K)	$\Delta S^{\ddagger}$ cal/(mol·K)	$\Delta G^{\ddagger}$ cal/(mol·K)	R^{2a}
EG	18.03 ($\pm$1.04)	-2.41 ($\pm$0.6)	17.32 ($\pm$0.86)	0.9811
EG − d4	18.97 ($\pm$0.35)	-0.60 ($\pm$0.12)	18.79 ($\pm$0.31)	0.9513

[a]R is the Pearson's correlation coefficient

This result seems to be contradicting with the aforementioned study of Warncke et al. as the entropy contribution is small in the total activation enthalpy change, as it is reported to be the case in the cleavage of Co-C bond in both aqueous solution. Moreover, the $\Delta H^{\ddagger}$ and $\Delta S^{\ddagger}$ values are less than, but in the same order of magnitude with the other high temperature enzymatic cleavage studies [124-127].

4.5 Conclusions

We showed that the UV-vis absorption spectroscopic monitoring of the Co-C bond homolysis in the EAL in the presence of the EG at close to the physiological temperature and solvent conditions give a reliable set of observed kinetics data. The parallel kinetics of the observed decay of the AdoCbl and the formation of the Cob(II)alamin UV-vis spectroscopic features is found to be promising for the further investigations for understanding which reaction steps in the EG catalyzed EAL kinetics that this observed kinetics correspond. The substrate concentration independence of the observed rate, substitution of the EG with the EG-d4, and the energetic analyses of the observed kinetics data, together with the aid of the previous reports gave a basis for further speculations. According to these speculations, the cleaved coenzyme Co center either remains in the cob(II)alamin state, or coordinates with the active site side chain residue which is

reduced by the excess substrate. That is, the Co-C cleavage step itself is observed, together with the formation of a non-native corrinoid. The activation energy parameters gave the similar results with the other enzymatic Co-C bond cleavage studies that is performed with the other substrates at ambient temperatures. Therefore, if the equilibrium assumption with the Co-C bond cleavage being the rate-limiting step holds, the EAL in the presence of EG drives the catalytic reaction with the activation enthalpy, and this single-step reaction with the EG corresponds to the same step in the enzyme catalysis that is driven by the other substrates.

As a future direction, this experiment could be repeated by using the UV-vis absorption values β- or γ-band as a measure for the time-coursed kinetics experiments, as the α-band reportedly features the X-B_{12} peaks too, which interfere with the observed reaction. In addition, since the excess EG is suspect for the formation of the X-B_{12}, a new set of data at a lower EG concentration could be planned. Also, as the future analyses of the current data, the full-wavelength spectral measurements can be deconvoluted to differentiate the spectra to its AdoCbl derivative components, so that the pure decay of the AdoCbl can be extracted from the observed data.

Chapter 5

Conclusions

This chapter includes the overall assessment of the studies that are presented in this dissertation, and connects the findings of these different studies. Although the reactions, techniques, experimental set-ups and objectives are vastly different for these three projects, one purpose is common: being able to understand the EAL kinetics and dynamical contributions to the EAL enzyme kinetics.

Among the three projects, the Co(II)-substrate radical pair decay (Chapter 2) that is observed by using time-resolved, full-spectrum CW-EPR (and also by using time-resolved UV-vis spectroscopy) provides the central conclusions in this dissertation. One striking finding was the presence of a non-native reaction path which is prevalent at low temperatures. This reaction path not only complemented and enhanced our understanding of native reaction kinetics by presenting a new set of data to be analyzed and used to speculate the structure and dynamics of the enzyme catalysis, the identification and characterization of this reaction path is essentially significant in itself and can render many future studies possible, such as investigating the effect of the protein fluctuations on the native reaction; i.e. comparing their impact on the native and non-native reaction would make the determination of the functionally important structural and conformational changes in the enzyme possible. This two different reactions can be reckoned as two different probes to understand the kinetics and dynamics of the enzyme catalysis.

Again in Chapter 2, along with the project-specific results, we found an abrupt transition in the observed kinetics of the Co(II)-substrate radical pair decay, which suggests a protein or solvent dynamic transition effect on the enzyme kinetics at 240 K. It is evident from the study in the Chapter 3 that the solvent dynamics goes through a transition region where the TEMPOL features two populations with different tumbling speeds at 230 – 245 K. Hence the transition that is seen in Chapter 2 in the Arrhenius relation of the substrate configuration rates at >240 K could

be as a result of the same solvent dynamical transition that is present in the TEMPOL studies. The solvent dynamics could be affecting the reaction chemistry via the changes in the protein active site geometry as a result of the solvent-dependent configurational relaxations. Also the substrate/product exchange experiments show a dynamical transition that occurs in the mesodomain where the holoenzyme resides, which is interpreted as mesodomain "melting" because when this transition occurs at 250 K, the excess substrate in the solvent gains diffusional ability similar to the aqueous solvent conditions.

As our kinetical investigation of the Co(II)-substrate radical decay pair suggests solvent-dependent dynamical transitions at 240 and 250 K, we targeted to study the solvent dynamical transitions in our samples by using mobility of spin probes as a measure of the state of the solvent (Chapter 3). Since the samples would be the identical to that of the Chapter 2 (frozen aqueous samples with EAL and AmPrOH), any phase transition that is observed in this chapter would be applicable to the interpretations of the Chapter 2. The spin probe mobility becomes detectable with X-band EPR at 220 K according to our results, which is also the initial temperature point of the kinetic decay study in Chapter 2. Two critical temperature ranges appeared as a result of the spin probe investigation of the mesodomain, 230 – 245 K, and above 250 K region. At 230 – 245 K, the solvent undergoes a transition to yield two different TEMPOL tumbling rate components; with the fast component gaining more weight as the temperature increases. This could be the origin of the transition that is present in the observed decay of the Co(II)-substrate radical pair at Chapter 2. In this study, starting around 240 K, the fast phase of the observed decay becomes dominant over the slow phase, and this dominant phase is the one that is associated with the radical rearrangement step. If the information from both studies are combined, we can say that the mesodomain undergoes a transition at 240 K that allows the larger-scale molecular motions to occur, and this

larger-scale molecular motions in the kinetic decay study would refer to the protein active site configurational changes that ease the isomerization of the amino group in the substrate during the radical rearrangement step, and hence increases the reaction rate.

The spin probe mobility studies show that above 255 K temperatures, the solvent seems to be going through a transition that allows the melting of the ice-water crystalline boundaries, which can be associated with the mesodomain "melting" that is also observed at the aforementioned substrate/product exchange experiment in Chapter 2. This proposal is also supported by the minimal kinetic model that suggests a decrease in the potential energy surface of the native protein configurations that occurs at around the same temperature (250 K). The melting in the mesodomain that starts around 245- 250 K causes the potential energy barrier of the native active site configuration decrease in the FEC representation in the kinetic model in Chapter 2. In summary, we had three different results from three different experiments that indicate a transition that starts occurring at 245-250 K and becomes predominant at above 255 K temperatures. These experiments and the transitions that they refer to are (in chronological order):

a.   **Substrate/product exchange experiment in Chapter 2**

The substrate enzyme interface undergoes a transition at 255 K to allow the diffusion of the excess free substrate to the protein active site.

b.   **The minimal kinetic modeling studies in Chapter 2**

A transition occurs at 240-245 K the active site geometry that makes the native substrate configuration more stable compared to the lower temperatures.

c.   **Spin probe mobility studies in Chapter 3**

(i) At 250 K, the TEMPOL exhibits uniform tumbling which means that the mesodomain becomes more homogeneous and viscous compared to that of the

lower temperatures. (ii) At 255 K, the EAL in the ice-crystal boundaries starts diffusing in the mesodomain. This cause an increase in the EAL concentration, and hence a higher viscosity in the mesodomain. Therefore the TEMPOL tumbling rate decreases at >250 K.

In conclusion, the dynamical transition starts in the protein and its mesodomain at 245 K (from (b) and (c,i) experiments), allowing the native substrate configuration to become more stable. Then at 255 K (from (a) and (c,ii) experiments), the transition at protein-crystal boundaries occur that changes the mesodoamin features by allowing the EAL that is locked in the crystal water to diffuse in the mesodomain.

In Chapter 4 a different reaction step in the EAL minimal reaction mechanism is studied using a different experimental setup. However, this chapter also contributes to the understanding of the kinetics of the EAL minimal reaction mechanism in a single-step resolution. A previous study from our lab also focused on the same reaction step, i.e. the Co-C bond cleavage, but in this study the reaction was induced by 2-aminopropanol in DMSO solvent and at low temperatures, because the reaction occurs spontaneously at room temperatures [67, 116]. In Chapter 4, we aimed to use a slower substrate, EG, which has reportedly a slower catalytic rate to be able to time-resolve the Co-C homolysis step at room temperatures and in water-based solvent would become possible. Therefore, this chapter is significant as it is exploring a temperature range that is very close to the physiological temperatures, as well as the liquid solvent conditions, which is pure, buffered water (i.e. no DMSO used as in the previous study [67]) and yet still approaching the EAL minimal reaction cycle with the same single reaction-step resolution with the EPR studies which are done under cryogenic temperatures with frozen samples.

We elucidated specific details of the B12-mediated catalysis in the EAL enzyme, and through the pioneering use of low temperature systems and correlations of results from multiple EPR techniques applied to protein and solvent, revealed features of dynamical contributions to enzyme reactions that are of general relevance.

References

1.   Ott, W.H., E.L. Rickes, and T.R. Wood, *Activity of crystalline vitamin B12 for chick growth.* Journal of Biological Chemistry, 1948. **174**(3): p. 1047-1048.

2.   Rickes, E.L., et al., *Crystalline vitamin B12.* Science, 1948. **107**(2781): p. 396-397.

3.   Smith, E.L., *Presence of cobalt in the anti-pernicious anaemia factor.* Nature, 1948. **162**(4108): p. 144.

4.   Hodgkin, D., M. Porter, and R. Spiller, *Crystalline Anti-Pernicious Anaemia Factor from Liver: Appendix: Crystallographic Measurements on the Anti-Pernicious Anaemia Factor.* Proceedings of the Royal Society of London. Series B, Biological Sciences, 1950: p. 609-613.

5.   Bonnett, R., et al., *The structure of vitamin B12 and its hexacarboxylic acid degradation product.* Nature, 1955. **176**(4477): p. 328-330.

6.   Brink, C., et al., *X-ray crystallographic evidence on the structure of vitamin B12.* Nature, 1954. **174**(4443): p. 1169-1171.

7.   Barker, H., H. Weissbach, and R. Smyth, *A coenzyme containing pseudovitamin B12.* Proceedings of the National Academy of Sciences of the United States of America, 1958. **44**(11): p. 1093.

8.   Reddy, K.H., *Bioinorganic chemistry*. 2007: New Age International.

9.   MURAKAMI, Y., *Vitamin B12 Models with Macrocyclic Ligands*. 1979.

10.   Brown, K.L., *Chemistry and enzymology of vitamin B12.* Chemical reviews, 2005. **105**(6): p. 2075-2150.

11.   Stich, T.A., et al., *Spectroscopic and computational studies of Co3+-corrinoids: Spectral and electronic properties of the B12 cofactors and biologically relevant precursors.* Journal of the American Chemical Society, 2003. **125**(19): p. 5897-5914.

12.   Buckel, W. and B.T. Golding, *Glutamate and 2-methyleneglutarate mutase: from microbial curiosities to paradigms for coenzyme B12-dependent enzymes.* Chem. Soc. Rev., 1996. **25**(5): p. 329-337.

13.   Banerjee, R., *Chemistry and Biochemistry of B12*. 1999: John Wiley & Sons.

14.   Toraya, T., *Radical catalysis in coenzyme B12-dependent isomerization (eliminating) reactions.* Chemical reviews, 2003. **103**(6): p. 2095-2128.

15.   Matthews, R.G., *Cobalamin-and corrinoid-dependent enzymes.* Metal ions in life sciences, 2009. **6**: p. 53.

16.   Barker, H., et al., *The Glutamate Mutase System ASSAYS AND PROPERTIES.* Journal of Biological Chemistry, 1964. **239**(10): p. 3260-3266.

17.   Pierik, A.J., et al., *Rotation of the exo-methylene group of (R)-3-methylitaconate catalyzed by coenzyme B12-dependent 2-methyleneglutarate mutase from Eubacterium barkeri.* Journal of the American Chemical Society, 2002. **124**(47): p. 14039-14048.

18.   Moore, B.S., et al., *On the stereospecificity of the coenzyme B12-dependent isobutyryl-CoA mutase reaction.* Journal of the American Chemical Society, 1995. **117**(45): p. 11285-11291.

19.   Marsh, E.N.G., *A radical approach to enzyme catalysis.* BioEssays, 1995. **17**(5): p. 431-441.

20.   Chirpich, T., et al., *Lysine 2, 3-Aminomutase PURIFICATION AND PROPERTIES OF A PYRIDOXAL PHOSPHATE AND S-ADENOSYLMETHIONINE-ACTIVATED ENZYME.* Journal of Biological Chemistry, 1970. **245**(7): p. 1778-1789.

21.   Wolthers, K.R., S.E. Rigby, and N.S. Scrutton, *Mechanism of radical-based catalysis in the reaction catalyzed by adenosylcobalamin-dependent ornithine 4, 5-aminomutase.* Journal of Biological Chemistry, 2008. **283**(50): p. 34615-34625.

22.   Shibata, N., et al., *A new mode of B$_{12}$ binding and the direct participation of a potassium ion in enzyme catalysis: X-ray structure of diol dehydratase.* Structure, 1999. **7**(8): p. 997-1008.

23.   Masuda, J., et al., *How a protein generates a catalytic radical from coenzyme B$_{12}$: X-ray structure of a diol-dehydratase–adeninylpentylcobalamin complex.* Structure, 2000. **8**(7): p. 775-788.

24.   Yamanishi, M., et al., *The crystal structure of coenzyme B12-dependent glycerol dehydratase in complex with cobalamin and propane-1, 2-diol.* European journal of biochemistry, 2002. **269**(18): p. 4484-4494.

25.   Liao, D.-I., et al., *Crystal structure of substrate free form of glycerol dehydratase.* Journal of inorganic biochemistry, 2003. **93**(1): p. 84-91.

26.   Stubbe, J. and W.A. van der Donk, *Protein radicals in enzyme catalysis.* Chemical reviews, 1998. **98**(2): p. 705-762.

27.   Babior, B.M. and T.K. Li, *Binding of cobamides to ethanolamine deaminase.* Biochemistry, 1969. **8**(1): p. 154-160.

28.   Babior, B.M., et al., *The Mechanism of Action of Ethanolamine Ammonia-Lyase, a B12-dependent Enzyme THE PARTICIPATION OF PARAMAGNETIC SPECIES IN THE CATALYTIC DEAMINATION OF 2-AMINOPROPANOL.* Journal of Biological Chemistry, 1974. **249**(14): p. 4537-4544.

29.   Bandarian, V. and G.H. Reed, *Analysis of the electron paramagnetic resonance spectrum of a radical intermediate in the coenzyme B12-dependent ethanolamine ammonia-lyase catalyzed reaction of S-2-aminopropanol.* Biochemistry, 2002. **41**(27): p. 8580-8588.

30.   Canfield, J.M. and K. Warncke, *Geometry of reactant centers in the COII-substrate radical pair state of coenzyme B12-dependent ethanolamine deaminase determined by using orientation-selection-ESEEM spectroscopy.* The Journal of Physical Chemistry B, 2002. **106**(34): p. 8831-8841.

31.   Licht, S.S., C.C. Lawrence, and J. Stubbe, *Class II ribonucleotide reductases catalyze carbon-cobalt bond reformation on every turnover.* Journal of the American Chemical Society, 1999. **121**(33): p. 7463-7468.

32.   Babior, B.M., J.S. Krouwer, and H. Hogenkamp, *The Mechanism of Adenosylcobalamin-Dependent Reaction.* Critical Reviews in Biochemistry and Molecular Biology, 1979. **6**(1): p. 35-102.

33.   Hay, B.P. and R.G. Finke, *Thermolysis of the cobalt-carbon bond in adenosylcorrins. 3. Quantification of the axial base effect in adenosylcobalamin by the synthesis and thermolysis of axial base-free adenosylcobinamide. Insights into the energetics of enzyme-assisted cobalt-carbon bond homolysis.* Journal of the American Chemical Society, 1987. **109**(26): p. 8012-8018.

34.   Finke, R.G. and B.P. Hay, *Thermolysis of adenosylcobalamin: a product, kinetic, and cobalt-carbon (C5') bond dissociation energy study.* Inorganic Chemistry, 1984. **23**(20): p. 3041-3043.

35.   Kratky, C., et al., *Accurate structural data demystify B12: high-resolution solid-state structure of aquocobalamin perchlorate and structure analysis of the aquocobalamin ion in solution.* Journal of the American Chemical Society, 1995. **117**(16): p. 4654-4670.

36.   Hay, B.P. and R.G. Finke, *Thermolysis of the Co・C bond in adenosylcobalamin (coenzyme B< sub> 12</sub>)—IV. Products, kinetics and Co・C bond dissociation energy studies in ethylene glycol.* Polyhedron, 1988. **7**(16): p. 1469-1481.

37.   Canfield, J.M. and K. Warncke, *Active Site Reactant Center Geometry in the CoII-Product Radical Pair State of Coenzyme B12-Dependent Ethanolamine Deaminase Determined by Using Orientation-Selection Electron Spin-Echo Envelope Modulation Spectroscopy.* The Journal of Physical Chemistry B, 2005. **109**(7): p. 3053-3064.

38.   Warncke, K. and A.S. Utada, *Interaction of the Substrate Radical and the 5'-Deoxyadenosine-5'-Methyl Group in Vitamin B12 Coenzyme-Dependent Ethanolamine Deaminase.* Journal of the American Chemical Society, 2001. **123**(35): p. 8564-8572.

39.   Buckel, W., C. Kratky, and B.T. Golding, *Stabilisation of methylene radicals by cob (II) alamin in coenzyme B12 dependent mutases.* Chemistry-A European Journal, 2006. **12**(2): p. 352-362.

40.   Kozlowski, P.M., et al., *Does Cob (II) alamin act as a conductor in coenzyme B12 dependent mutases?* Angewandte Chemie International Edition, 2007. **46**(6): p. 980-983.

41.   Faust, L., et al., *Cloning, sequencing, and expression of the genes encoding the adenosylcobalamin-dependent ethanolamine ammonia-lyase of Salmonella typhimurium.* Journal of Biological Chemistry, 1990. **265**(21): p. 12462-12466.

42.   Sun, L. and K. Warncke, *Comparative model of EutB from coenzyme B12-dependent ethanolamine ammonia-lyase reveals a β8α8, TIM-barrel fold and radical catalytic site structural features.* Proteins: Structure, Function, and Bioinformatics, 2006. **64**(2): p. 308-319.

43.   Shibata, N., et al., *Crystal structures of ethanolamine ammonia-lyase complexed with coenzyme B12 analogs and substrates.* Journal of Biological Chemistry, 2010. **285**(34): p. 26484-26493.

44.   Shibata, N., Y. Higuchi, and T. Toraya, *How coenzyme B12-dependent ethanolamine ammonia-lyase deals with both enantiomers of 2-amino-1-propanol as substrates: structure-based rationalization.* Biochemistry, 2010. **50**(4): p. 591-598.

45.   Gerards, L.E., et al., *A study of the cage mechanism for the homolytic cleavage of the cobalt-carbon bond in coenzyme B< sub> 12</sub> by varying the solvent viscosity.* Inorganica Chimica Acta, 1991. **190**(1): p. 47-53.

46.   Bradbeer, C., *The clostridial fermentations of choline and ethanolamine I. Preparation and properties of cell-free extracts.* Journal of Biological Chemistry, 1965. **240**(12): p. 4669-4674.

47.   Law, P. and J. Wood, *Studies on the mechanism of ethanolamine ammonia lyase using 2-ethoxyethylamine as a substrate.* Biochimica et Biophysica Acta (BBA)-Enzymology, 1973. **321**(1): p. 382-396.

48.   Abeles, R.H. and D. Dolphin, *The vitamin B12 coenzyme.* Accounts of Chemical Research, 1976. **9**(3): p. 114-120.

49.   Babior, B.M., *The Mechanism of Action of Ethanolamine Deaminase VI. ETHYLENE GLYCOL, A QUASI-SUBSTRATE FOR ETHANOLAMINE DEAMINASE.* Journal of Biological Chemistry, 1970. **245**(7): p. 1755-1766.

50.   Frey, P.A., M.K. Essenberg, and R.H. Abeles, *Studies on the mechanism of hydrogen transfer in the cobamide coenzyme-dependent dioldehydrase reaction.* Journal of Biological Chemistry, 1967. **242**(22): p. 5369-5377.

51.   Sun, L., et al., *Critical Role of Arginine 160 of the EutB Protein Subunit for Active Site Structure and Radical Catalysis in Coenzyme B12-Dependent Ethanolamine Ammonia-lyase†.* Biochemistry, 2008. **47**(20): p. 5523-5535.

52.   Poyner, R.R., et al., *Probing nitrogen-sensitive steps in the free-radical-mediated deamination of amino alcohols by ethanolamine ammonia-lyase.* Journal of the American Chemical Society, 2006. **128**(22): p. 7120-7121.

53.   Carty, T.J., B.M. Babior, and R.H. Abeles, *The Mechanism of Action of Ethanolamine Ammonia-Lyase, a B12-dependent Enzyme IX. INTERACTION OF THE ENZYME-COENZYME COMPLEX WITH REACTION PRODUCTS.* Journal of Biological Chemistry, 1971. **246**(20): p. 6313-6317.

54.   Atherton, N.M., *Principles of Electron Spin Resonance*. 1993: Ellis Horwood Limited: New York.

55.   Gilbert, B.C., *Electron paramagnetic resonance*. Vol. 21. 2008: Royal Society of Chemistry.

56.   Berliner, L.J., *Spin labeling: theory and applications*. 2013: Academic Press.

57.   Senesi, N., et al., *Electron spin (or paramagnetic) resonance spectroscopy.* Methods of soil analysis. Part 3-chemical methods., 1996: p. 323-356.

58. Redfield, A.G., *On the theory of relaxation processes.* IBM Journal of Research and Development, 1957. **1**(1): p. 19-31.

59. Bartucci, R. and L. Sportelli, *ESR investigation on the phase transitions of DPPC vesicles in presence of high concentrations of Li+, Na+, K+ and Cs+.* Colloid and Polymer Science, 1993. **271**(3): p. 262-267.

60. Reed, G.H., *Radical mechanisms in adenosylcobalamin-dependent enzymes.* Current opinion in chemical biology, 2004. **8**(5): p. 477-483.

61. Wetmore, S.D., et al., *Understanding the mechanism of action of B12-dependent ethanolamine ammonia-lyase: synergistic interactions at play.* Journal of the American Chemical Society, 2002. **124**(47): p. 14054-14065.

62. Frey, P., *Cobalamin coenzymes in enzymology*. 2010, Elsevier: Oxford, UK. p. 501-546.

63. Toraya, T., *Cobalamin-dependent dehydratases and a deaminase: Radical catalysis and reactivating chaperones.* Archives of biochemistry and biophysics, 2014. **544**: p. 40-57.

64. Ngai, K. and S. Capaccioli, *Unified explanation of the anomalous dynamic properties of highly asymmetric polymer blends.* The Journal of chemical physics, 2013. **138**(5): p. 054903.

65. Panagopoulou, A., et al., *Protein and Water Dynamics in Bovine Serum Albumin–Water Mixtures over Wide Ranges of Composition.* The Journal of Physical Chemistry B, 2012. **116**(15): p. 4593-4602.

66. Gallat, F.-X., et al., *Dynamical coupling of intrinsically disordered proteins and their hydration water: comparison with folded soluble and membrane proteins.* Biophysical journal, 2012. **103**(1): p. 129-136.

67. Wang, M. and K. Warncke, *Kinetic and thermodynamic characterization of COII-substrate radical pair formation in coenzyme B12-dependent ethanolamine ammonia-lyase in a cryosolvent system by using time-resolved, full-spectrum continuous-wave electron paramagnetic resonance spectroscopy.* Journal of the American Chemical Society, 2008. **130**(14): p. 4846-4858.

68. Zhu, C. and K. Warncke, *Kinetic Isolation and Characterization of the Radical Rearrangement Step in Coenzyme B12-Dependent Ethanolamine Ammonia-lyase.* Journal of the American Chemical Society, 2010. **132**(28): p. 9610-9615.

69. Zhu, C. and K. Warncke, *Reaction of the Co II-Substrate Radical Pair Catalytic Intermediate in Coenzyme B 12-Dependent Ethanolamine Ammonia-Lyase in Frozen Aqueous Solution from 190 to 217K.* Biophysical journal, 2008. **95**(12): p. 5890-5900.

70. Padmakumar, R., R. Padmakumar, and R. Banerjee, *Evidence that cobalt-carbon bond homolysis is coupled to hydrogen atom abstraction from substrate in methylmalonyl-CoA mutase.* Biochemistry, 1997. **36**(12): p. 3713-3718.

71.   Graves, S.W., J.A. Fox, and B.M. Babior, *Deamination of 2-aminopropanol by ethanolamine ammonia-lyase, an AdoCbl-requiring enzyme. Kinetics and isotope effects for the R and S enantiomers of the substrate.* Biochemistry, 1980. **19**(15): p. 3630-3633.

72.   WALLIS, O.C., et al., *The Extents of Formation of Cobalt (II)-Radical Intermediates in the Reactions with Different Substrates Catalysed by the Adenosylcobalamin-Dependent Enzyme Ethanolamine Ammonia-Lyase.* European Journal of Biochemistry, 1982. **125**(2): p. 299-303.

73.   Bender, G.n., R.R. Poyner, and G.H. Reed, *Identification of the Substrate Radical Intermediate Derived from Ethanolamine during Catalysis by Ethanolamine Ammonia-Lyase†.* Biochemistry, 2008. **47**(43): p. 11360-11366.

74.   Woodward, J., et al., *Time-resolved studies of radical pairs.* Biochemical Society Transactions, 2009. **37**(2): p. 358.

75.   C. Zhu, M.K., & K. Warncke, unpublished.

76.   Wang, M., et al., *Chapter Four-Resolution and Characterization of Chemical Steps in Enzyme Catalytic Sequences by Using Low-Temperature and Time-Resolved, Full-Spectrum EPR Spectroscopy in Fluid Cryosolvent and Frozen Solution Systems.* Methods in enzymology, 2015. **563**: p. 59-94.

77.   Chen, H., L. Sun, and K. Warncke, *Heterogeneous Ordered–Disordered Structure of the Mesodomain in Frozen Sucrose–Water Solutions Revealed by Multiple Electron Paramagnetic Resonance Spectroscopies.* Langmuir, 2013. **29**(13): p. 4357-4365.

78.   Faust, L.P. and B.M. Babior, *Overexpression, purification, and some properties of the AdoCbl-dependent ethanolamine ammonia-lyase from Salmonella typhimurium.* Archives of biochemistry and biophysics, 1992. **294**(1): p. 50-54.

79.   Abend, A., et al., *Ethanolamine Ammonia-Lyase Has a "Base-On" Binding Mode for Coenzyme B₁₂.* Archives of biochemistry and biophysics, 1999. **370**(1): p. 138-141.

80.   B. Nforneh, K.W., unpublished.

81.   Zagalak, B., et al., *The stereochemistry of the conversion of D and L 1, 2-propanediols to propionaldehyde.* Journal of Biological Chemistry, 1966. **241**(13): p. 3028-3035.

82.   Rétey, J., et al., *The Stereochemistry of the Reaction Catalyzed by Ethanolamine AmmoniaLyase, an Adenosylcobalamindependent Enzyme AN EXAMPLE OF RACEMIZATION ACCOMPANYING SUBSTITUTION.* Journal of Biological Chemistry, 1974. **249**(19): p. 6359-6360.

83.   Austin, R.H., et al., *Dynamics of ligand binding to myoglobin.* Biochemistry, 1975. **14**(24): p. 5355-5373.

84.   Gregory, R., *Protein-solvent interactions.* 1995: CRC Press.

85.   Kuntz Jr, I. and W. Kauzmann, *Hydration of proteins and polypeptides.* Advances in protein chemistry, 1974. **28**: p. 239.

86.   Fenimore, P.W., et al., *Bulk-solvent and hydration-shell fluctuations, similar to α-and β-fluctuations in glasses, control protein motions and functions.* Proceedings of the National Academy of Sciences of the United States of America, 2004. **101**(40): p. 14408-14413.

87.   Ringe, D. and G.A. Petsko, *[19] Study of protein dynamics by X-ray diffraction.* Methods in enzymology, 1986. **131**: p. 389-433.

88.   Kohn, J.E., et al., *Evidence of functional protein dynamics from X-ray crystallographic ensembles.* PLoS Comput Biol, 2010. **6**(8): p. 1-5.

89.   Parak, F., E. Knapp, and D. Kucheida, *Protein dynamics: Mössbauer spectroscopy on deoxymyoglobin crystals.* Journal of molecular biology, 1982. **161**(1): p. 177-194.

90.   Frauenfelder, H., F. Parak, and R.D. Young, *Conformational substates in proteins.* Annual review of biophysics and biophysical chemistry, 1988. **17**(1): p. 451-479.

91.   Doster, W., S. Cusack, and W. Petry, *Dynamical transition of myoglobin revealed by inelastic neutron scattering.* 1989.

92.   Ngai, K., S. Capaccioli, and A. Paciaroni, *Change of caged dynamics at Tg in hydrated proteins: Trend of mean squared displacements after correcting for the methyl-group rotation contribution.* The Journal of chemical physics, 2013. **138**(23): p. 235102.

93.   Wolf, M., et al., *Relaxation dynamics of a protein solution investigated by dielectric spectroscopy.* Biochimica et Biophysica Acta (BBA)-Proteins and Proteomics, 2012. **1824**(5): p. 723-730.

94.   Cametti, C., et al., *Dielectric relaxation spectroscopy of lysozyme aqueous solutions: Analysis of the δ-dispersion and the contribution of the hydration water.* The Journal of Physical Chemistry B, 2011. **115**(21): p. 7144-7153.

95.   Angell, C.A., *Formation of glasses from liquids and biopolymers.* Science, 1995. **267**(5206): p. 1924.

96.   Iben, I., et al., *Glassy behavior of a protein.* Physical review letters, 1989. **62**(16): p. 1916.

97.   Frauenfelder, H., et al., *A unified model of protein dynamics.* Proceedings of the National Academy of Sciences, 2009. **106**(13): p. 5129-5134.

98.   Guzzi, R., R. Bartucci, and D. Marsh, *Heterogeneity of Protein Substates Visualized by Spin-label EPR.* Biophysical journal, 2014. **106**(3): p. 716-722.

99.   Steinhoff, H.-J., K. Lieutenant, and J. Schhtter, *Residual motion of hemoglobin-bound spin labels as a probe for protein dynamics.* Zeitschrift für Naturforschung C, 1989. **44**(3-4): p. 280-288.

100.   Stoll, S. and A. Schweiger, *EasySpin, a comprehensive software package for spectral simulation and analysis in EPR.* Journal of Magnetic Resonance, 2006. **178**(1): p. 42-55.

101.   Jensen, K.P. and U. Ryde, *How the Co-C bond is cleaved in coenzyme B12 enzymes: a theoretical study.* Journal of the American Chemical Society, 2005. **127**(25): p. 9117-9128.

102. Firth, R., et al., *The chemistry of vitamin B 12. Part XI. Some further formation constants.* Journal of the Chemical Society A: Inorganic, Physical, Theoretical, 1969: p. 381-386.

103. Grate, J. and G. Schrauzer, *Sterically induced, spontaneous dealkylation of secondary alkylcobalamins due to axial base coordination and conformational changes of the corrin ligand.* J. Am. Chem. Soc., 1979. **101**: p. 4601-4611.

104. Halpern, J., *Mechanisms of coenzyme B12-dependent rearrangements.* Science, 1985. **227**(4689): p. 869-875.

105. De Ridder, D.J., E. Zangrando, and H.-B. Bürgi, *Structural behaviour of cobaloximes: planarity, an anomalous trans-influence and possible implications on Co-C bond cleavage in coenzyme-B 12-dependent enzymes.* Journal of Molecular Structure: THEOCHEM, 1996. **374**(1): p. 63-83.

106. Bresciani-Pahor, N., et al., *Organocobalt B 12 models: axial ligand effects on the structural and coordination chemistry of cobaloximes.* Coordination chemistry reviews, 1985. **63**: p. 1-125.

107. Vlasie, M.D. and R. Banerjee, *Tyrosine 89 accelerates Co-carbon bond homolysis in methylmalonyl-CoA mutase.* Journal of the American Chemical Society, 2003. **125**(18): p. 5431-5435.

108. Toraya, T. and A. Ishida, *Acceleration of cleavage of the carbon-cobalt bond of sterically hindered alkylcobalamins by binding to apoprotein of diol dehydrase.* Biochemistry, 1988. **27**(20): p. 7677-7681.

109. Zhu, L. and N.M. Kostic, *Molecular orbital study of coenzyme B12. Activation of the cobalt-carbon bond by angular distortions.* Inorganic Chemistry, 1987. **26**(25): p. 4194-4197.

110. Mancia, F. and P.R. Evans, *Conformational changes on substrate binding to methylmalonyl CoA mutase and new insights into the free radical mechanism.* Structure, 1998. **6**(6): p. 711-720.

111. Banerjee, R., *The Yin-Yang of cobalamin biochemistry.* Chemistry & biology, 1997. **4**(3): p. 175-186.

112. Puckett, J.M., et al., *Near-IR FT-Raman spectroscopy of methyl-B12 and other cobalamins and of imidazole and imidazolate methylcobinamide derivatives in aqueous solution.* Inorganic Chemistry, 1996. **35**(16): p. 4656-4662.

113. Dong, S., et al., *Resonance Raman Co-C stretching frequencies reflect bond strength changes in alkyl cobalamins, but are unaffected by trans ligand substitution.* Journal of the American Chemical Society, 1996. **118**(38): p. 9182-9183.

114. Dong, S., et al., *Co-C Bond Activation in B12-Dependent Enzymes: Cryogenic Resonance Raman Studies of Methylmalonyl-Coenzyme A Mutase.* Journal of the American Chemical Society, 1999. **121**(30): p. 7063-7070.

115. Brunold, T., et al. *Spectroscopic and computational insights into the biosynthesis and reactivity of adenosylcobalamin.* in *ABSTRACTS OF PAPERS OF THE AMERICAN CHEMICAL SOCIETY.* 2003. AMER CHEMICAL SOC 1155 16TH ST, NW, WASHINGTON, DC 20036 USA.

116.   Wang, M.a.W., Kurt, unpublished, 2009.

117.   Russell, H.J., et al., *Protein Motions Are Coupled to the Reaction Chemistry in Coenzyme B12-Dependent Ethanolamine Ammonia Lyase.* Angewandte Chemie International Edition, 2012. **51**(37): p. 9306-9310.

118.   Kräutler, B., *Vitamin B12: chemistry and biochemistry.* Biochemical Society Transactions, 2005. **33**(4): p. 806-810.

119.   Morrison, J.F., *Michaelis–Menten Kinetics.* Encyclopedia of Molecular Biology.

120.   Salama, S. and T.G. Spiro, *Visible and near-ultraviolet resonance Raman spectra of photolabile vitamin B12 derivatives with a rapid-flow technique.* Journal of Raman Spectroscopy, 1977. **6**(2): p. 57-60.

121.   Bandarian, V. and G.H. Reed, *Isotope effects in the transient phases of the reaction catalyzed by ethanolamine ammonia-lyase: Determination of the number of exchangeable hydrogens in the enzyme-cofactor complex.* Biochemistry, 2000. **39**(39): p. 12069-12075.

122.   Walker, L.A., et al., *Time-resolved spectroscopic studies of B12 coenzymes: the identification of a metastable cob (III) alamin photoproduct in the photolysis of methylcobalamin.* Journal of the American Chemical Society, 1998. **120**(15): p. 3597-3603.

123.   Wang, M. and K. Warncke, *Entropic Origin of Cobalt–Carbon Bond Cleavage Catalysis in Adenosylcobalamin-Dependent Ethanolamine Ammonia-Lyase.* Journal of the American Chemical Society, 2013. **135**(40): p. 15077-15084.

124.   Hay, B.P. and R.G. Finke, *Thermolysis of the cobalt-carbon bond of adenosylcobalamin. 2. Products, kinetics, and cobalt-carbon bond dissociation energy in aqueous solution.* Journal of the American Chemical Society, 1986. **108**(16): p. 4820-4829.

125.   Sharma, P.K., et al., *A new paradigm for electrostatic catalysis of radical reactions in vitamin B12 enzymes.* Proceedings of the National Academy of Sciences, 2007. **104**(23): p. 9661-9666.

126.   Garr, C.D., J.M. Sirovatka, and R.G. Finke, *Adenosylcobinamide, the Base-Free Analog of Coenzyme B12 (Adenosylcobalamin). 1.1 Probing the Role of the Axial 5, 6-Dimethylbenzimidazole Base in Coenzyme B12 via Exogenous Axial Base K association, Δ H, and Δ S Measurements plus a Critical Review of the Relevant Biochemical Literature.* Inorganic Chemistry, 1996. **35**(20): p. 5912-5922.

127.   Bucher, D., et al., *The elusive 5'-deoxyadenosyl radical in coenzyme-B12-mediated reactions.* Journal of the American Chemical Society, 2012. **134**(3): p. 1591-1599.